Cell Reports

Article

ZBTB7A is a modulator of KDM5-driven transcriptional networks in basal breast cancer

Graphical abstract

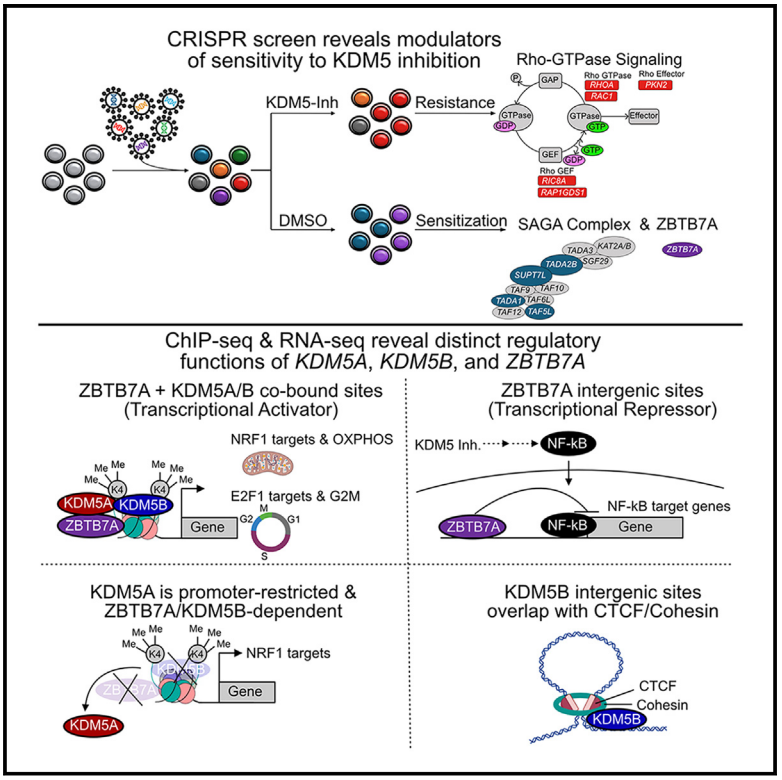

Highlights

- Deletion of *ZBTB7A* transcription factor and core SAGA complex synergizes with KDM5 inhibitors
- KDM5A chromatin binding is altered by ZBTB7A deletion
- Loss of ZBTB7A potentiates KDM5 inhibition-induced signaling changes by modulating NF-κB
- High ZBTB7A in triple-negative breast cancer with no response to neoadjuvant chemotherapy

Authors

Benedetto DiCiaccio, Marco Seehawer, Zheqi Li, ..., Jason S. Carroll, Henry W. Long, Kornelia Polyak

Correspondence

kornelia_polyak@dfci.harvard.edu

In brief

DiCiaccio et al. conducted a CRISPR viability screen to characterize mechanisms of response and resistance to KDM5 inhibition in basal breast cancer and identified the ZBTB7A transcription factor as a key mediator of KDM5A chromatin binding. Deletion of ZBTB7A alters NF-κB and mitochondrial signaling following KDM5 inhibition.

DiCiaccio et al., 2024, Cell Reports *43*, 114991
December 24, 2024
https://doi.org/10.1016/j.celrep.2024.114991

CellPress

Cell Reports

CellPress
OPEN ACCESS

Article

ZBTB7A is a modulator of KDM5-driven transcriptional networks in basal breast cancer

Benedetto DiCiaccio,[1,2,3] Marco Seehawer,[1,2,3] Zheqi Li,[1,2,3] Andriana Patmanidis,[1] Triet Bui,[1,2,3] Pierre Foidart,[1,2,3] Jun Nishida,[1,2,3] Clive S. D'Santos,[4] Evangelia K. Papachristou,[4] Malvina Papanastasiou,[5] Andrew H. Reiter,[5] Xintao Qiu,[6] Rong Li,[6] Yijia Jiang,[6] Xiao-Yun Huang,[1] Anton Simeonov,[7] Stephen C. Kales,[7] Ganesha Rai,[7] Madhu Lal-Nag,[7] Ajit Jadhav,[7] Myles Brown,[1,2,3] Jason S. Carroll,[4] Henry W. Long,[6] and Kornelia Polyak[1,2,3,5,6,8,9,*]

[1]Department of Medical Oncology, Dana-Farber Cancer Institute, Boston, MA 02215, USA
[2]Department of Medicine, Brigham and Women's Hospital, Boston, MA 02115, USA
[3]Department of Medicine, Harvard Medical School, Boston, MA 02115, USA
[4]Cambridge Research Institute, University of Cambridge, Cambridge, UK
[5]The Eli and Edythe L. Broad Institute, Cambridge, MA 02142, USA
[6]Center for Functional Cancer Epigenetics, Dana-Farber Cancer Institute, Boston, MA 02215, USA
[7]National Center for Advancing Translational Sciences, National Institutes of Health, Bethesda, MD 20892, USA
[8]The Ludwig Center at Harvard, Boston, MA 02115, USA
[9]Lead contact
*Correspondence: kornelia_polyak@dfci.harvard.edu
https://doi.org/10.1016/j.celrep.2024.114991

SUMMARY

We previously described that the *KDM5B* histone H3 lysine 4 demethylase is an oncogene in estrogen-receptor-positive breast cancer. Here, we report that *KDM5A* is amplified and overexpressed in basal breast tumors, and KDM5 inhibition (KDM5i) suppresses the growth of *KDM5*-amplified breast cancer cell lines. Using CRISPR knockout screens in a basal breast cancer cell line with or without KDM5i, we found that deletion of the *ZBTB7A* transcription factor and core SAGA complex sensitizes cells to KDM5i, whereas deletion of RHO-GTPases leads to resistance. Chromatin immunoprecipitation sequencing (ChIP-seq) and RNA sequencing (RNA-seq) revealed co-localization of ZBTB7A and KDM5A/B at promoters with high histone H3K4me3 and dependence of KDM5A chromatin binding on ZBTB7A. *ZBTB7A* knockout altered the transcriptional response to KDM5i at NF-κB targets and mitochondrion-related pathways. High expression of *ZBTB7A* in triple-negative breast cancer is significantly associated with poor response to neoadjuvant chemotherapy. Our work furthers the understanding of KDM5-mediated gene regulation and identifies mediators of sensitivity to KDM5i.

INTRODUCTION

Histone modifications regulate chromatin structure and transcription, and abnormalities in this process are involved in cancer.[1,2] Genes encoding histones and chromatin modifiers are frequently mutated in human cancers,[1,3] yet the role of these in tumorigenesis remains poorly defined. Epigenetic regulators define cell states, and cellular phenotypic heterogeneity is a driver of tumor progression and therapeutic resistance.[4,5]

The KDM5 family of histone 3 lysine 4 (H3K4) demethylases has been implicated as oncogenes in breast cancer. Breast cancer is a heterogeneous disease clinically classified based on the presence of estrogen receptors (ERs) and progesterone receptors (PRs) and HER2 into ER^+, $HER2^+$, and triple-negative ($ER^-/PR^-/HER2^-$; TNBC) subtypes, while gene expression profiling has demonstrated luminal, basal, and mesenchymal molecular subtypes.[6] We previously identified *KDM5B* as a luminal lineage-driving oncogene frequently amplified in ER^+ tumors and associated with endocrine resistance.[7] In line with this, deletion of *Kdm5b* in mice delays mammary gland development by perturbing luminal epithelial cell differentiation.[8] Subsequently, both *KDM5A* and *KDM5B* paralogs were found to contribute to endocrine therapy resistance, indicating redundancy as oncogenes in ER^+ breast cancer.[9,10] In addition, inhibition of KDM5 catalytic activity decreased cellular transcriptomic heterogeneity, overcoming endocrine resistance.[10]

The role of KDM5 demethylases in TNBC is less clear, with *KDM5A* and *KDM5B* demonstrating divergent results. *KDM5A* is significantly associated with metastatic relapse in ER^- breast cancer patients, and *KDM5A* knockdown significantly reduced lung metastasis *in vivo*.[11] However, studies of *KDM5B* in TNBC models implicate *KDM5B* as a tumor suppressor.[12,13] KDM5B inhibits the expression of CCL14 through interaction with the LSD1/NuRD complex, thus suppressing angiogenesis.[13] In addition, *KDM5B* overexpression reduced *in vitro* migration and invasion of TNBC cell lines, depending on the interaction between KDM5B's PHD1 domain and unmethylated H3K4.[12] Therefore,

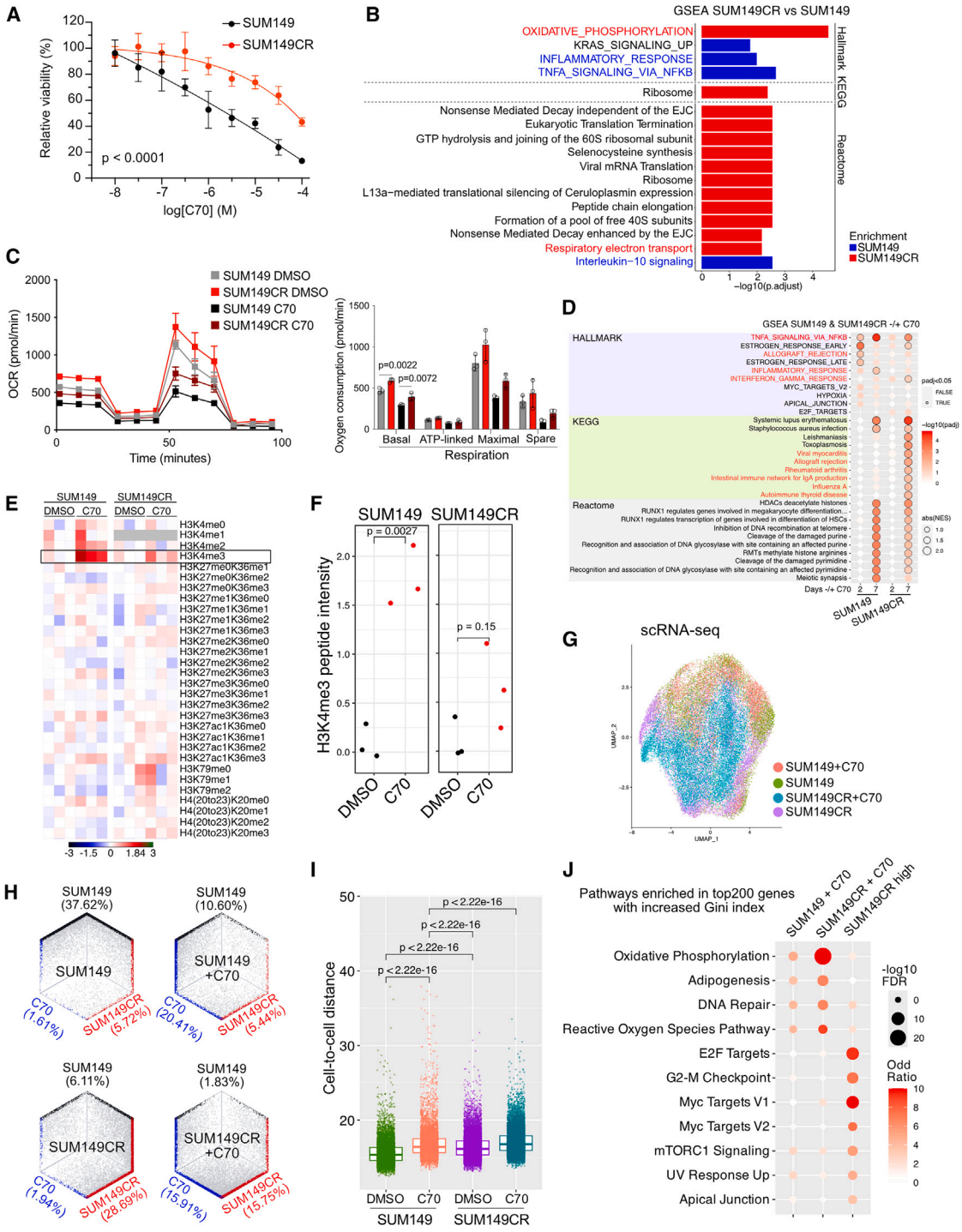

Figure 1. Characterization of the SUM149CR cell line

(A) Viability of SUM149 and SUM149CR cells after 7 days of treatment across C70 concentrations. *p* = t test comparing area under the curve. Data are the mean ± standard deviation (*n* = 6).

(B) Gene Set Enrichment Analysis (GSEA) comparing RNA-seq profiles of SUM149CR and SUM149 cells.

(C) Oxygen consumption rate (OCR) in SUM149 and SUM149CR cells ± pre-treatment with 10 μM C70 for 6 days; plot (left) and bar graph depicting quantification of differences (right). Values are the mean ± standard deviation. *n* = 3 for all conditions. One-way ANOVA with multiple comparison within either DMSO- or C70-treated groups for each respiration phase test was used.

(D) GSEA comparing RNA-seq profiles of SUM149 ± 10 μM C70 and SU149CR ± 10 μM C70. Top 10 most significant gene sets from each database are shown.

(legend continued on next page)

the function of KDM5 demethylases and their therapeutic potential in TNBC are still unclear.

To investigate the functional relevance of KDM5 in TNBC and basal breast cancer, we analyzed genetic alterations in the KDM5 family and found the *KDM5A* paralog to be specifically amplified and overexpressed in basal breast cancer. We next analyzed KDM5 inhibition (KDM5i) sensitivity in breast cancer cell lines and identified the SUM149 *KDM5A*-amplified basal TNBC line with high sensitivity to KDM5i. Using this line and its KDM5i-resistant derivative, we performed genome-wide CRISPR screens to identify modulators of KDM5 inhibitor sensitivity. We followed up top hits and integrated these data with RNA sequencing (RNA-seq) and chromatin immunoprecipitation sequencing (ChIP-seq) to understand the signaling pathways associated with KDM5 activity in basal breast cancer.

RESULTS

KDM5A is commonly amplified and overexpressed in basal breast cancer

Both *KDM5A* and *KDM5B* were reported to be amplified and overexpressed in breast cancer.[7,14] However, paralog-specific differences between luminal and basal breast cancer have not been analyzed. Thus, we assessed the mutational landscape of KDM5 paralogs in luminal A (LumA) and basal breast tumors in the TCGA cohort. We previously reported that *KDM5B* is specifically amplified in LumA breast cancer (Figure S1A).[7,10] However, *KDM5A* was specifically amplified in basal breast cancer to a similar degree (Figures S1A and S1B), and *KDM5A* expression was also the highest in the basal subtype (Figure S1C).[15] Although *KDM5A* had been reported in the 12p13.3 amplicon detected in ~15% of breast cancers,[14,15] we demonstrate that this amplification is basal subtype specific, with *KDM5A* being amplified in over 50% of basal breast cancers (Figure S1B). Given that basal breast cancers tend to be ER^-, this could explain why *KDM5A* expression correlates with metastatic progression only in ER^- tumors.[11]

To address if *KDM5A* and *KDM5B* are co-amplified passenger genes and not drivers of their amplicons, we assessed all regions of chromosomes 1 (*KDM5B* amplicon) and 12 (*KDM5A* amplicon), respectively, to identify the most frequent amplifications (Figures S1D and S1E). Amplification of chromosome 1q (*KDM5B* locus) is frequent in LumA breast cancer (Figure S1D), while chromosome 12p13.33 (*KDM5A* locus) gain is frequent in basal tumors (Figure S1E). In addition, among all genes on chromosome 12, *KDM5A* is the second most frequently amplified gene next to *ETV6*. However, the oncoPrint plot shows that *KDM5A* amplification commonly occurs in the absence of *ETV6* amplification (Figure S1F), indicating it is not a passenger associated with *ETV6*.

The effect of the C70 KDM5 inhibitor on breast cancer cell lines

To determine subtype-specific difference in response to KDM5i, we tested the sensitivity of breast cancer cell lines to the pan-KDM5 inhibitor C70.[16] $HER2^+$ and some TNBC cell lines (MDA-MB-436 mesenchymal and SUM149 basal) were the most sensitive (Figures S2A and S2B). Sensitivity to C70 did not significantly correlate with the expression levels of KDM5 family members (Figure S2C), potentially due to small sample size. While high sensitivity of $HER2^+$ breast cancer has been shown before,[17] similar sensitivity in a subset of TNBC lines has not been described. Thus, we chose the SUM149 basal *KDM5A*-amplified TNBC cell line for further studies.

To study mechanisms of acquired resistance to KDM5i, we generated C70-resistant derivatives of SUM149 cells, SUM149CR, by prolonged culture with 10 μM C70 (Figure 1A). We then performed RNA-seq and gene set enrichment analysis (GSEA) on untreated SUM149 and SUM149CR cells. GSEA of differentially expressed genes (DEGs) revealed oxidative phosphorylation as the top enriched pathway in SUM149CR, while inflammatory response and interleukin-10 (IL-10) and nuclear factor κB (NF-κB) signaling were enriched in SUM149 (Figure 1B; Table S1). To test potential differences in mitochondrial function between SUM149 and SUM149CR cells, we performed the Mito Stress Test ± 10 μM C70. SUM149CR showed significantly higher basal respiration compared to SUM149, validating the RNA-seq data, while C70 treatment decreased respiration in both cell lines (Figure 1C).

To identify C70 resistance-associated gene expression changes, we performed RNA-seq on SUM149 and SUM149CR cells ± 10 μM C70 for 2 or 7 days. SUM149CR had a delayed transcriptional response to C70, indicated by a smaller shift in RNA-seq principal-component analysis (PCA) coordinates at 2 days, but this difference diminished by 7 days of treatment (Figure S2E). Quantification using Euclidian distances confirmed this observation (Figure S2F). In line with this, SUM149CR cells had attenuated enrichment of signaling pathways after C70 treatment (Figure 1D). In SUM149 cells, we found enrichment for tumor necrosis factor α (TNF-α) signaling via NF-κB and inflammatory response upon C70 treatment (Figure 1D). However, in SUM149CR, these pathways were either delayed (TNF-α signaling via NF-κB) or absent (inflammatory response). Quantitative histone mass spectrometry demonstrated muted response of SUM149CR cells to C70 after 2 days of treatment compared to SUM149 based on changes in H3K4me3 (Figures 1E and 1F; Table S2).

(E) Heatmap of normalized peptide intensities from mass spectrometry analysis of histone modifications in SUM149 and SUM149CR ± 10 μM C70 treatment for 48 h. Lysine residues that can be methylated are shown. Peptide intensities were normalized to the DMSO control within each cell line, in which there were three processing replicates.
(F) Boxplot depicting quantification of H3K4me3 peptide intensities. The *p* values are based on the t test.
(G) Uniform Manifold Approximation and Projection (UMAP) of scRNA-seq in SUM149 and SUM149CR ± 10 μM C70 for 7 days.
(H) Hexagonal plots showing classification of single cells as parental (black), parental C70-treated (C70; teal), or C70-resistant (SUM149CR; red) populations.
(I) Boxplot showing transcriptomic cell-to-cell Euclidean distance from PCA dimension reduction in the indicated groups. Mann Whitney U test was used.
(J) Dot plot illustrating the enrichment of hallmark pathways in the top 200 genes with increased Gini index in the indicated groups. Pathways with false discovery rate (FDR) < 0.05 in at least one groups are selected.

To explore resistance and response to C70 at the single-cell level, we performed single-cell RNA-seq (scRNA-seq) on SUM149 and SUM149CR cell lines ± C70 for 7 days. Both SUM149 and SUM149CR cells tended to occupy different regions of Uniform Manifold Approximation and Projection (UMAP) space (Figure 1G). To determine if these cell states are acquired or pre-existing, we next generated cell state signatures from DEGs between SUM149, SUM149CR, and C70-treated SUM149 + C70 from bulk RNA-seq and classified each individual cell into these states. The resistant state was present in a subset of SUM49 cells prior to treatment, while the C70 state was quite distinct, and very few cells occupied this state (Figure 1H). The transition to this C70 state after 7 days of treatment was similar between SUM149 and SUM149CR, indicating that SUM149CR maintains a similar, yet delayed, transcriptional response to C70 treatment.

Previously, we found that C70 treatment reduced cellular transcriptomic heterogeneity of luminal ER$^+$ cell lines but had the opposite effect in the SUM159 TNBC cell line.[10] To explore C70 effects in SUM149 and SUM149CR lines, we calculated cell-to-cell transcriptomic distances ± C70 treatment. We found that C70 treatment increased cell-to-cell transcriptomic distances in both SUM149 and SUM149CR cells and that SUM149CR cells had higher baseline heterogeneity compared to SUM149 (Figure 1I). To investigate transcriptomic heterogeneity changes, we performed GSEA on genes with increasing Gini index after C70 treatment or resistance (i.e., more heterogeneously expressed genes). Pathways related to oxidative phosphorylation and reactive oxygen species (ROS) were top enriched in both cell lines after C70 treatment, while proliferation-related pathways were enriched in SUM149CR compared to SUM149 (Figure 1J).

These results imply that C70 has the largest impact on genes related to mitochondrial function and proliferation.

CRISPR viability screen to identify modulators of KDM5 inhibitor sensitivity

To identify synthetic lethal targets and mechanisms of resistance to C70 in basal breast cancer, we performed a genome-wide CRISPR-Cas9 knockout (KO) viability screen ± C70 in SUM149 and SUM149CR. In SUM149 we identified 69 and 138 genes that when deleted made cells more sensitive or resistant to C70, respectively ($p < 0.001$) (Figure 2A; Table S3). Although *KDM5A* was a resistance hit (Figure 2A), it had a low robust rank aggregation (RRA) score, and *KDM5A* and *KDM5B* KO cell lines did not reveal significant differences in C70 response in cell growth or histone H3K4me3 levels (Figures S2G–S2I). SUM149CR produced fewer hits (24 resistance and 39 sensitizers; $p < 0.001$) and displayed limited overlap with SUM149 cells (Figures 2A and 2B; Table S3). Only three targets increased sensitivity to C70 in both the SUM149 and the SUM149CR cells: *XPR1* (retrovirus receptor), *TADA2B* (transcriptional adaptor), and *MTCH2* (mitochondrial carrier homolog) (Figure 2B; Table S2). We also integrated our RNA-seq data with the CRISPR hits. *SOX7*, *IL7*, *KIAA1257*, *MUC6*, and *DLG5* were differentially enriched in the SUM149 CRISPR screen ($p < 0.001$) and differentially expressed (padj < 0.05 and abs(log2(FC)) > 1) between SUM149CR and SUM149, while *ROS1* and *FUT3* were CRISPR hits and differentially expressed between C70- and DMSO-treated SUM149 cells (Table S3).

Among the most significantly depleted hits in C70-treated SUM149 was the transcription factor *ZBTB7A* (Figure 2A; Table S3).[18] *ZBTB7A* is thought to act as a transcriptional repressor and associates with DNA-repressive complexes (e.g., NuRD, Sin3a, and NCoR).[19,20] Among the most significantly enriched hits in C70-treated SUM149 were members of the RHOA/RAC1 GTPase cycle (Figures 2A, S2J, and S2K; Table S3). Four of the top six resistance hits included the *RHOA* and *RAC1* GTPases in addition to the RHOA-effector proteins *PKN2* and *ILK* (integrin-linked kinase). Because ILK and RHO/RAC regulate extracellular matrix attachment and cell shape,[21] their identification as top C70 resistance hits implies that cell shape might influence response to KDM5i.

We then performed GSEA for Hallmark, KEGG, and Reactome gene sets and CORUM protein complexes within the differentially enriched CRISPR screen hits. Within SUM149, loss of MYC targets was associated with increased resistance (Figure 2C), consistent with prior reports identifying *KDM5A* required for MYC-driven transcription in multiple myeloma.[22] In addition, the RAC1-RHOA-VANGL2 and the SAGA complex were significantly enriched among gRNA targets associated with resistance (Figure 2D). The SAGA complex is a transcriptional co-activator with both histone acetyltransferase (H3K9ac and H3K14ac) and deubiquitinase (H2BK120ub) enzymatic activity.[23] Four of the eight SAGA subunits were hits in the SUM149 screen (*TADA1*, *SUPT7L*, *SPT20H*, and *TAF5L*), and one member of the SAGA histone acetyltransferase (*TADA2B*) was a hit in both SUM149 and SUM149CR screens (Figures 2A and 2B). This implies that a decrease in SAGA complex activity may increase sensitivity to KDM5i.

To validate the role of *ZBTB7A*, *RHOA*, and *PKN2* deletion in KDM5i sensitivity, we generated SUM149 cell lines expressing constitutive Cas9 and individual gRNAs (Figure S2L). *ZBTB7A* deletion reduced growth in the presence of C70, but not DMSO, compared to control guides targeting the *ROSA26* locus as well as a non-targeting control guide, confirming the screen results (Figures 2E and 2F). For *RHOA* and *PKN2*, only one guide per gene induced a sufficient decrease in protein levels (*RHOA*-g1 and *PKN2*-g1, Figure S2L). Consequently, only these effective guides led to increased growth in the presence of C70 compared to controls (Figures 2E and 2F). In addition, *RHOA*/*PKN2* KO had a larger effect on growth in C70 than in DMSO, in agreement with our CRISPR screen.

To investigate how RHO-GTPase signaling could alter sensitivity to KDM5i, we assessed if cell density affects C70-mediated growth arrest and performed RHOA/RAC1-GTP pull-down assays. We found that cells plated at higher densities had diminished sensitivity to C70 (Figure S2M). Pull-downs for GTP-bound RHOA and RAC1 ± C70 showed that under sparse conditions, KDM5i led to a reduction in GTP-bound RHOA (Figure S2N). Therefore, RHO-GTPase signaling might modify KDM5i and vice versa, but delineating these interactions requires further studies.

Because our eventual goal is to evaluate the therapeutic potential of KDM5 inhibitors in breast cancer, we focused on sensitizing hits. We selected *ZBTB7A* for further studies as it was a top

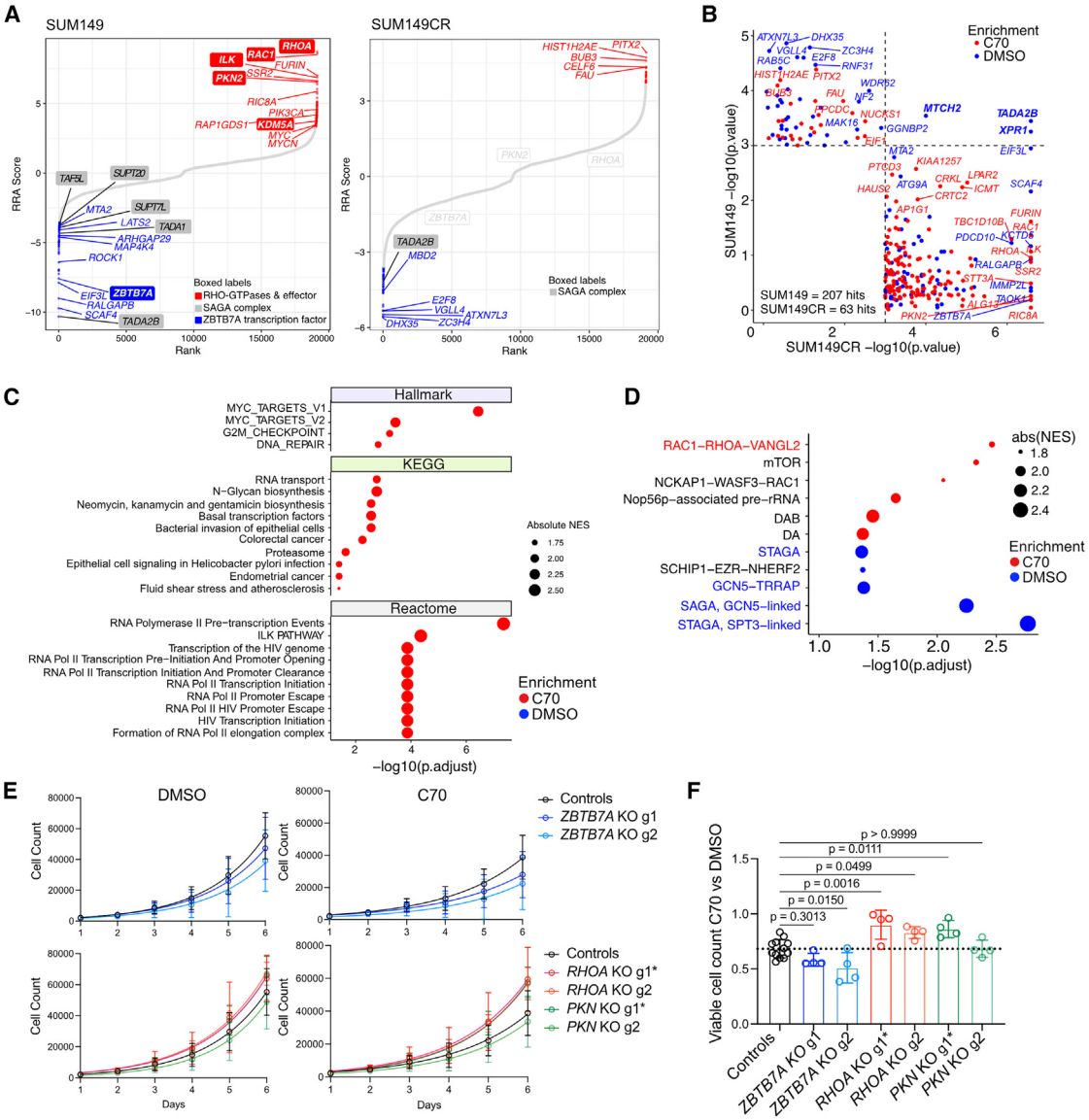

Figure 2. CRISPR screen results and validation

(A) Rank plots of CRISPR KO viability screens in SUM149 and SUM149CR cells after 10 doublings ± 10 μM C70. Genes are ranked based on the computed RRA score from MaGECK RRA, which indicates the essentiality of each gene. Positive RRA scores indicate enriched in C70. Negative RRA scores indicate enriched in DMSO. Differentially enriched hits ($p < 0.001$) are marked in blue and red for DMSO-enriched and C70-enriched hits, respectively.

(B) Comparison of CRISPR hits with $p < 0.001$ in either the SUM149 or the SUM149CR CRISPR screens ± C70.

(C and D) GSEA on RRA-ranked CRISPR screen results in SUM149. Top 10 most significant gene sets with padj < 0.05 from the indicated databases (C) and CORUM protein complexes (D) are shown.

(E) Cell growth assays of SUM149 cells expressing constitutive Cas9 and guide RNAs (gRNAs) targeting *ZBTB7A*, *RHOA*, *PKN2*, or non-targeting controls. gRNAs with more efficient KO efficiency are marked with an asterisk (see also Figure S2L). Data are the mean ± standard deviation ($n = 4$, controls are merged ROSA26 and NonTargeting cells with $n = 4$ each).

(F) Bar plot depicting quantification of ratios in viable cell numbers upon DMSO vs. C70 treatment at day 6. Data are the mean ± standard deviation, one-way ANOVA followed by Dunnett's multiple comparisons test comparing to control group only ($n = 4$, controls are merged ROSA26 and cells expressing non-targeting gRNAs with $n = 4$ each).

See also Figure S2.

hit sensitizing cells to C70 and the ZBTB7A DNA binding motif was the second most enriched motif in our prior KDM5B ChIP-seq data,[7] implying that ZBTB7A and KDM5 family members may interact at common loci.

ZBTB7A, KDM5A/B, repressive chromatin complexes, and response to KDM5i

ZBTB7A and KDM5s are considered repressive factors that associate with multiple histone deacetylase (HDAC)-containing

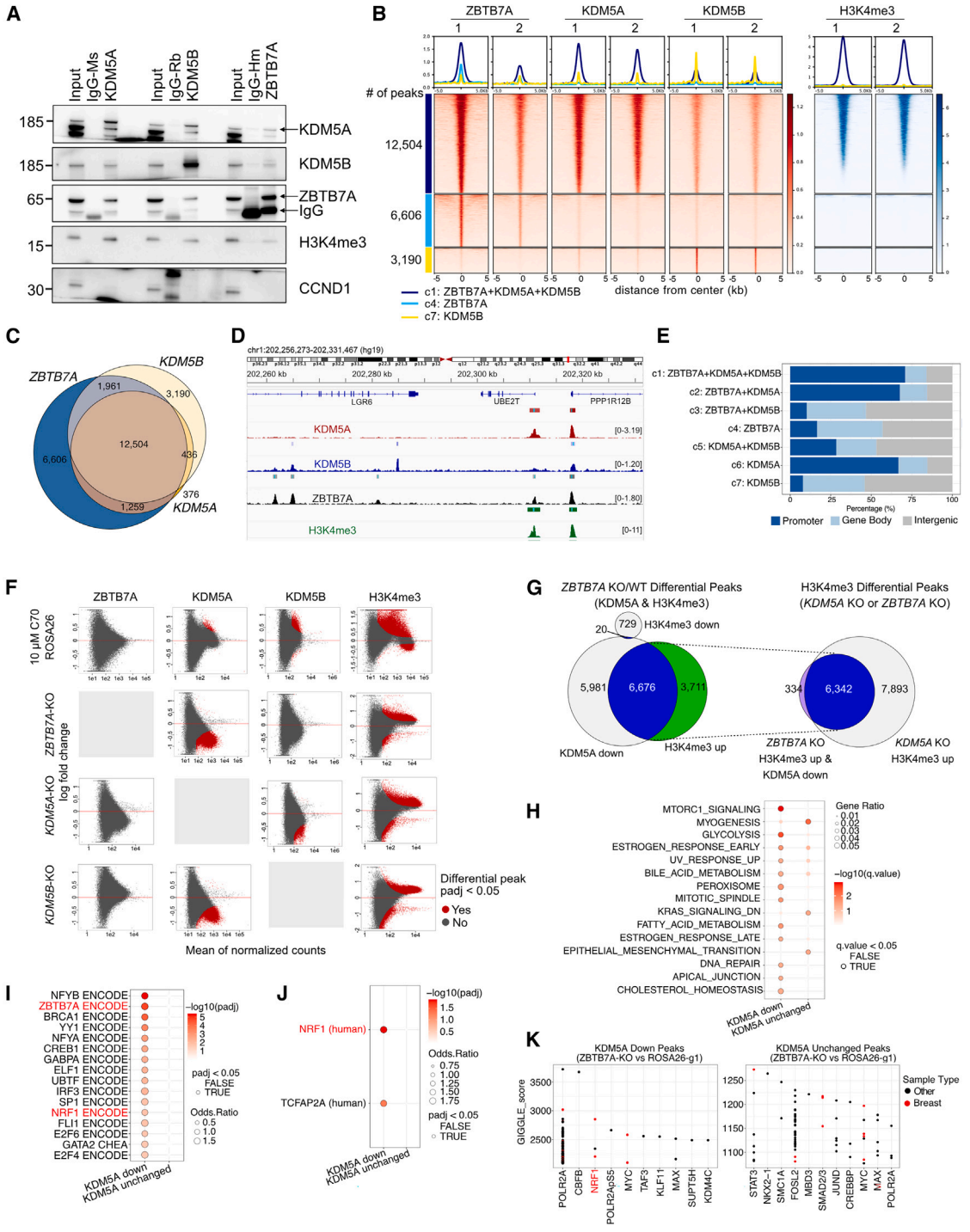

Figure 3. ZBTB7A and KDM5A/B interact and co-localize on DNA with high H3K4me3 levels

(A) Immunoblot analysis of ZBTB7A, KDM5A, and KDM5B in total cell lysates (input), control IgG, and the indicated immunoprecipitants in SUM149 cells.

(B) Heatmap of ChIP-seq for ZBTB7A, KDM5A, KDM5B, and H3K4me3. Peaks are clustered based on the intersection of peak calls among the three proteins.

(C) Venn diagram illustrating overlap of ChIP-seq peaks.

(D) Example ChIP-seq bigwig tracks with the hg19 genome as a reference.

(E) Genomic feature distribution of peaks within clusters.

(F) MA plots showing differential peak enrichment for the indicated proteins (columns) after the indicated perturbations (rows). Each perturbation is compared to SUM149-ROSA26-g1 in DMSO. Differential peaks are indicated in red (*padj* < 0.05; default output from CoBRA (Containerized Bioinformatics Workflow for Reproducible ChIP/ATAC-seq Analysis) using the Wald test from DEseq2). The y axis shows log fold change; x axis shows mean of normalized counts.

(legend continued on next page)

complexes.[24,25] Cross-referencing the BioGrid database, we found that ZBTB7A shared 15 interactors with KDM5A and/or KDM5B, 7 within the SWI/SNF, NuRD, and core HDAC chromatin complexes (Figure S3A).[26,27] The STRING database of protein-protein interaction networks also predicted functional interactions with chromatin-repressive complexes, in which KDM5A associates with SIN3B and ZBTB7A with NuRD and nuclear co-repressor NCOR1 (Figure S3B).[28] Guides targeting the *MTA2* and *MBD2* subunits of NuRD were significantly depleted upon C70 treatment in SUM149 and SUM149CR CRISPR screens, respectively (Figures 2A and 2B). Therefore, perturbation of the NuRD complex may also sensitize SUM149 cells to KDM5i.[13,29,30]

To delineate these protein interaction complexes we performed qPLEX-RIME (quantitative multiplexed rapid immunoprecipitation mass spectrometry)[31] for KDM5B in luminal ER$^+$ (MCF-7 and T47D) and TNBC (SUM149 and SUM159) cell lines (Table S4). Components of the NuRD, SWI/SNF, and other chromatin complexes were detected in both the luminal and the basal cell lines (Figure S3C). Immunoprecipitation of KDM5B revealed association with many of the core NuRD subunits, MTA1, MTA2, MBD2, MBD3, CHD3, and CHD4, while ZBTB7A pull-downs showed only weak bands for CHD4 and MTA1 (Figure S3D). These data imply that ZBTB7A may sensitize to C70 treatment by modulating the interaction of KDM5A and KDM5B with repressive chromatin complexes.

The STRING database also predicted functional interactions between KDM5A/KDM5B and members of the mitochondrial ATP synthase complex V based on co-expression (Figure S3E) corresponding to C70-resistant cells having higher expression of genes related to oxidative phosphorylation, many of which are subunits of the mitochondrial respiratory chain complexes I–IV or enzymes within the tricarboxylic acid cycle (TCA) cycle (Figures 1B and S3E) and imply that KDM5A/B may regulate mitochondrial activity.

ZBTB7A and KDM5A/B interact and co-localize on chromatin with high H3K4me3 levels

In our previous KDM5B ChIP-seq data ZBTB7A was among the most enriched DNA binding motifs.[7] To test if ZBTB7A and KDM5A/B are in the same protein complexes, we performed immunoprecipitation followed by immunoblot using H3K4me3 and CCND1 as positive and negative controls, respectively. We detected ZBTB7A in both KDM5A and KDM5B immunoprecipitants, and both KDM5 family members were present in ZBTB7A pull-downs (Figure 3A). Furthermore, both KDM5A and KDM5B were detected in ZBTB7A immunoprecipitants in both SUM149 and SUM149CR cells regardless of C70 treatment (Figure S3F), indicating that C70 does not disrupt these protein complexes.

To assess if ZBTB7A and KDM5A/B co-localize at the same chromatin regions, we performed ChIP-seq for each protein. We found a significant overlap between ZBTB7A, KDM5A, and KDM5B peaks, especially at sites with high levels of H3K4me3 (Figures 3B–3D and S3G; Table S4). We clustered the peaks based on overlap and found that 47% of all high-confidence peaks (i.e., peaks called across replicates) are co-occupied by ZBTB7A, KDM5A, and KDM5B and coincide with high levels of H3K4me3 (12,504 of 26,332) (Figures 3B, 3C, and S3G). Interestingly, KDM5A primarily bound promoter regions with high H3K4me3 signal, while ZBTB7A and KDM5B were found at both promoter and non-promoter regions (Figures 3E and S3H). This suggests that KDM5A and KDM5B may have distinct preference for genomic loci and thus functions, although differences due to antibodies used for ChIP cannot be excluded.

To determine correlations of each peak cluster with other chromatin binding factors, we explored overlap with public ChIP-seq data using Cistrome DB's toolkit[33] and compared the top 10 factors identified for each cluster based on the maximum GIGGLE score ($-$log10(*p*adj) * odds ratio from Fisher's exact test)[34] (Figure S3I). ZBTB7A binding in non-promoter regions (clusters 3 and 4) had specific overlap for SWI/SNF (SMARCC1 and SMARCA4) and NuRD (MBD3) chromatin complexes. It was also enriched for STAT3, which regulates the NF-κB signaling pathway.[35] The KDM5B-specific cluster 7 overlapped with factors related to the cohesin/CTCF complex (STAG1, SMC3, SMC1A, RAD21, ESCO2, and CTCF), in line with our prior data demonstrating that KDM5B physically interacts and co-localizes with CTCF.[7] Factors enriched across KDM5A-containing clusters were mostly associated with active promoters (e.g., H3K4me3, H3K9ac, and POLR2A), in agreement with KDM5A being mainly restricted to promoter regions. Enrichment analysis of the ZBTB7A consensus sequence (GACCC)[36] showed significant enrichment only in overall ZBTB7A peaks and in clusters where ZBTB7A and KDM5A peaks overlapped (Figure S3J), strengthening the importance of the ZBTB7A/KDM5A interactions.

To gain functional insights into each cluster, we assessed overlap of their predicted target genes with Hallmark gene signatures (Figure S3K) using the top 500 predicted target genes based on regulatory potential scores (Table S5).[32] Cluster 1 (co-bound by KDM5A, KDM5B, and ZBTB7A) was significantly enriched for Hedgehog signaling, G2M checkpoint, glycolysis, and hypoxia. Clusters 3 and 4 (mostly intergenic regions bound by ZBTB7A) showed enrichment for apical junction and coagulation. Finally, cluster 7 (mostly intergenic KDM5B peaks) was

(G) Venn diagrams showing overlap between KDM5A down and H3K4me3 up peaks in *ZBTB7A* KO cells. The intersect of these peaks is then compared with H3K4me3 up peaks in *KDM5A* KO cells.
(H–J) Overlap of the top 500 predicted target genes of KDM5A down/unchanged peaks in the *ZBTB7A* KO with the described gene sets. (H) Hallmark pathways, (I) consensus target genes for transcription factors present in ENCODE and ChEA, (J) position weight matrices from TRANSFAC and JASPAR at the gene promoters. The top 500 target genes were identified via the regulatory potential score from BETA.[32]
(K) Overlap of the entire set of KDM5A down/unchanged peaks in the *ZBTB7A* KO with public ChIP-seq tracks available on CISTROME.[33] The top 10–11 enriched transcription factors are shown ranked by GIGGLE score ($-$log10(*p*) * odds ratio).[34]
See also Figure S3.

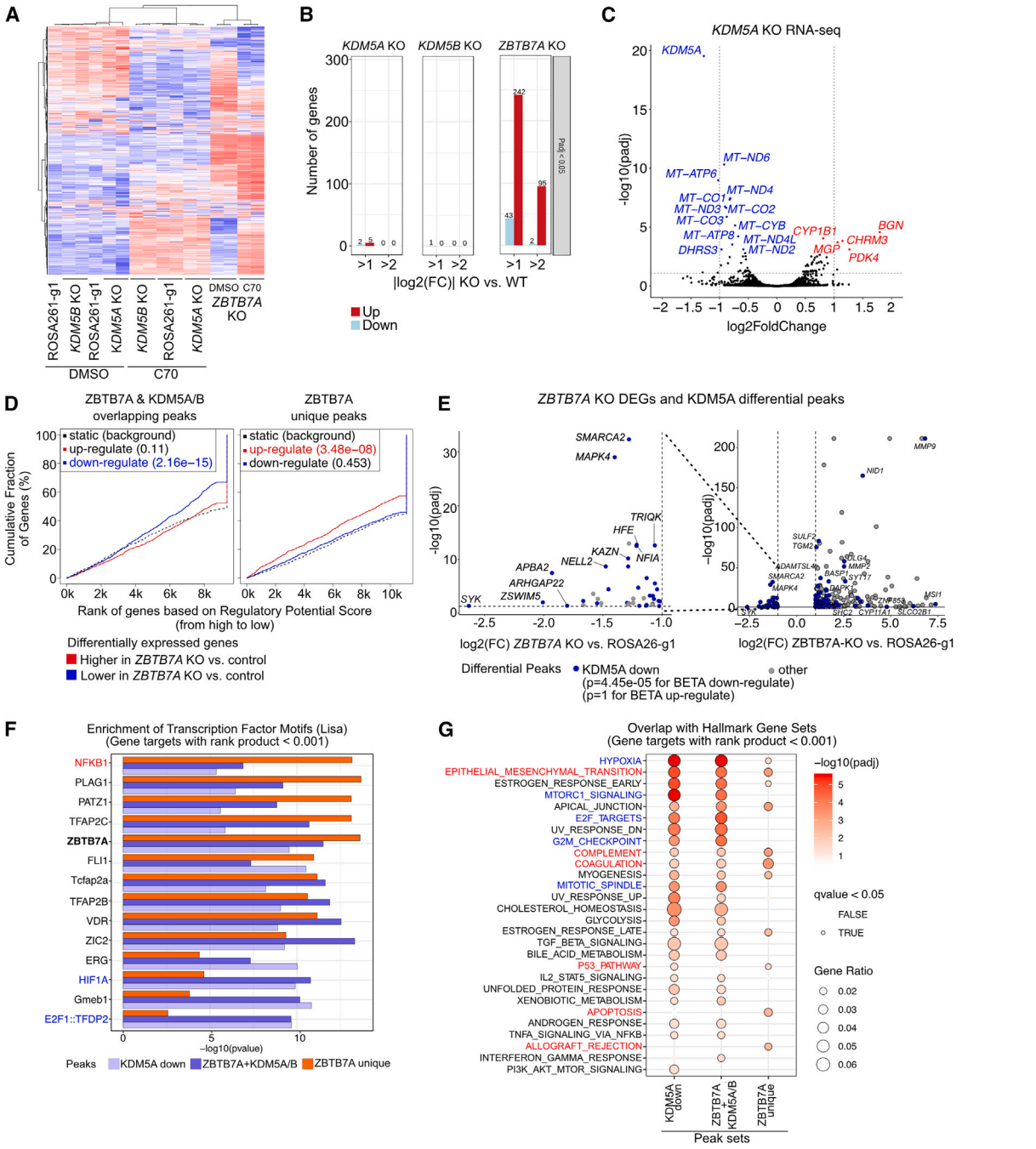

Figure 4. Gene expression changes induced by ZBTB7A-KO and its associations with ZBTB7A and KDM5A/B peak sets

(A) Heatmap of RNA-seq in SUM149 cells expressing the indicated gRNAs treated with DMSO or 10 μM C70 for 7 days. Rows and columns are ordered based on hierarchical clustering. Values are row-normalized *Z* scores.

(B) Number of DEGs for KOs in SUM149 cells compared to the ROSA26-g1 control.

(C) Volcano plot of RNA-seq in the SUM149 *KDM5A* KO compared to the ROSA26-g1 control. Dashed gray lines indicate adjusted *p* value (padj) and fold change (FC) cutoff used for (B).

(D) Output from BETA testing for association between the indicated peak sets and the up-/downregulated genes upon *ZBTB7A* KO.[32] For promoter-enriched peaks, the distance from the transcription start site (TSS) for within which peaks were considered to contribute to the gene regulatory potential score was set to 3 kb. For non-promoter-enriched peak sets, the default parameter of 100 kb was used.

(legend continued on next page)

significantly enriched for downregulated genes in response to UV. There is little overlap between the top 500 target genes of each cluster (Figure S3L), implying both shared and unique functions for each of the three proteins.

ZBTB7A KO reduces chromatin-bound KDM5A

To test if the co-localization of ZBTB7A, KDM5A, and KDM5B is due to direct recruitment mechanisms, we performed ChIP-seq in SUM149 ROSA26g control and in each of the three individual KO cells. ZBTB7A binding was not affected by deletion of KDM5A and KDM5B or by C70 treatment (Figure 3F). However, deletion of *ZBTB7A* led to decreased KDM5A signal in 43% of KDM5A peaks with no effect on KDM5B binding (Figure 3F). Since total KDM5A protein levels were not reduced in the *ZBTB7A* KO (Figure S2L), ZBTB7A may help recruit and/or stabilize KDM5A but not KDM5B at specific loci. KDM5A peaks were also decreased in the *KDM5B* KO, and conversely, we observed diminished KDM5B peak intensities in the *KDM5A* KO, implying mutual stabilization of KDM5A and KDM5B at a subset of binding sites (Figures 3F and S4A). However, potential cross-reactivity of the KDM5A and KDM5B antibodies used for ChIP cannot be excluded.

Next, we assessed whether KDM5A peaks that were decreased in *ZBTB7A* KO cells were associated with changes in H3K4me3. We found that 53% of these peaks were associated with an increase in H3K4me3 (Figures 3G and S4B). To determine whether the increase in H3K4me3 signal at these loci is a consequence of diminished KDM5A binding, we analyzed H3K4me3 at these loci in *KDM5A* KO cells and found that 95% of these peaks also had increased H3K4me3 upon KDM5A KO (Figures 3G and S4B). Therefore, loss of ZBTB7A likely leads to a decrease in KDM5A chromatin binding and a subsequent increase in H3K4me3.

To identify differences between changed and unchanged KDM5A peaks in *ZBTB7A* KO cells, we first identified the top 500 predicted gene targets based on regulatory potential scores (Table S5) and quantified overlap with Hallmark gene sets. Genes associated with diminished KDM5A peaks had stronger enrichment for mTORC1 signaling and glycolysis, whereas those associated with unchanged KDM5A peaks had stronger enrichment with myogenesis (Figure 3H). Second, overlap with consensus transcription factor targets from ENCODE/ChEA and promoter motifs from TRANSFAC/JASPAR identified nuclear respiratory factor 1 (*NRF1*) transcription factor as consistently enriched among KDM5A down-target genes (Figures 3I and 3J). *NRF1* is a regulator of nuclear genes encoding mitochondrial respiratory complex subunits and the transcription and replication of mitochondrial DNA.[37] We also saw enrichment for ZBTB7A among the KDM5A down-target genes (Figure 3I), supporting that these are ZBTB7A-specific peaks. Finally, we assessed the entire KDM5A decreased and unchanged peak sets for overlap with public ChIP-seq data in CISTROME.[38] Again, NRF1 was significantly enriched among the KDM5A peaks diminished in the *ZBTB7A* KO cells, implicating its importance as a putative downstream target of ZBTB7A and KDM5A in basal breast cancer (Figure 3K). To test if the enrichment in NRF1 binding sites in KDM5A peaks lost in *ZBTB7A* KO cells is due to differences in NRF1 expression or nuclear localization, we performed immunoblot analysis for NRF1 in fractionated cell lysates from wild-type (WT) and *KDM5A* or *ZBTB7A* KO cell lines but found no differences (Figure S4C). Thus, the enrichment for NRF1 targets might indicate overlap between the downstream targets of NRF1 and the KDM5A-ZBTB7A complex rather than its direct activation.

ZBTB7A activation/repressive regulatory function depends on the chromatin context

We next investigated gene expression changes induced by *KDM5A*, *KDM5B*, or *ZBTB7A* KO. Overall, *KDM5A* and *KDM5B* KOs had minimal impact on gene expression compared to the ZBTB7A KO at the high stringency we used as cut off ($p$adj < 0.05 and |log2(FC)| > 1) (Figures 4A and 4B; Table S1). A possible explanation is the redundancy of KDM5A and KDM5B, and the deletion of only one is not sufficient to cause major transcriptomic changes. Supporting this idea is the observation that C70 treatment that inhibits all KDM5s led to significant changes in gene expression in both WT and KO cells (Figure 4A; Table S1). It is also possible that the acute deletion of the gene has an effect, but this is diminished by the time the cells are expanded due to compensatory mechanisms. However, we do see significant changes in the expression of mitochondria-encoded genes in the KDM5A KO cells; 11 of the 13 most downregulated genes ($p$adj < 0.001) in the *KDM5A* KO were mitochondrial encoded (Figure 4C; Table S1), which was not observed in *KDM5B* KO cells (Figure S4D). This result is consistent with our findings of ZBTB7A-dependent KDM5A peaks being enriched in targets of the mitochondrial biogenesis transcription factor *NRF1*.

We next integrated RNA-seq from the *ZBTB7A* KO with our ChIP-seq data to determine if ZBTB7A binding was significantly associated with changes in gene expression. Based on binding and expression target analysis (BETA),[32] we found that ZBTB7A peaks overlapping with KDM5A/B, which are enriched at promoters, were associated with decreased gene expression in the *ZBTB7A* KO (p = 2.16e−15 for BETA downregulated) (Figure 4D). Conversely, ZBTB7A-unique sites, which are enriched in intronic/intergenic regions, were associated with increased gene expression in the *ZBTB7A* KO cells (p = 3.48e−08 for BETA upregulated) (Figure 4D). Therefore, non-promoter ZBTB7A may be acting as a canonical repressor, whereas promoter-bound ZBTB7A may be acting as a transcriptional activator.

We next investigated if changes in chromatin were associated with differential gene expression. As expected, increased

(E) Volcano plot comparing DEGs and decreased KDM5A peak enrichment in the *ZBTB7A* KO cells. Only significant DEGs are shown ($p$adj < 0.05 and | log2(FC)| > 1). The p values are based on BETA, indicating if the differential peak set is significantly associated with up- or downregulated genes. Nearest genes to each peak are annotated.

(F and G) Overlap of the predicted target genes for each peak set with (F) CISTROME LISA transcription factor motifs (top 5 motifs per cluster are shown) and (G) Hallmark gene sets. Genes with a rank product score <0.001 from the BETA output were used as predicted target genes for each peak set.

See also Figure S4.

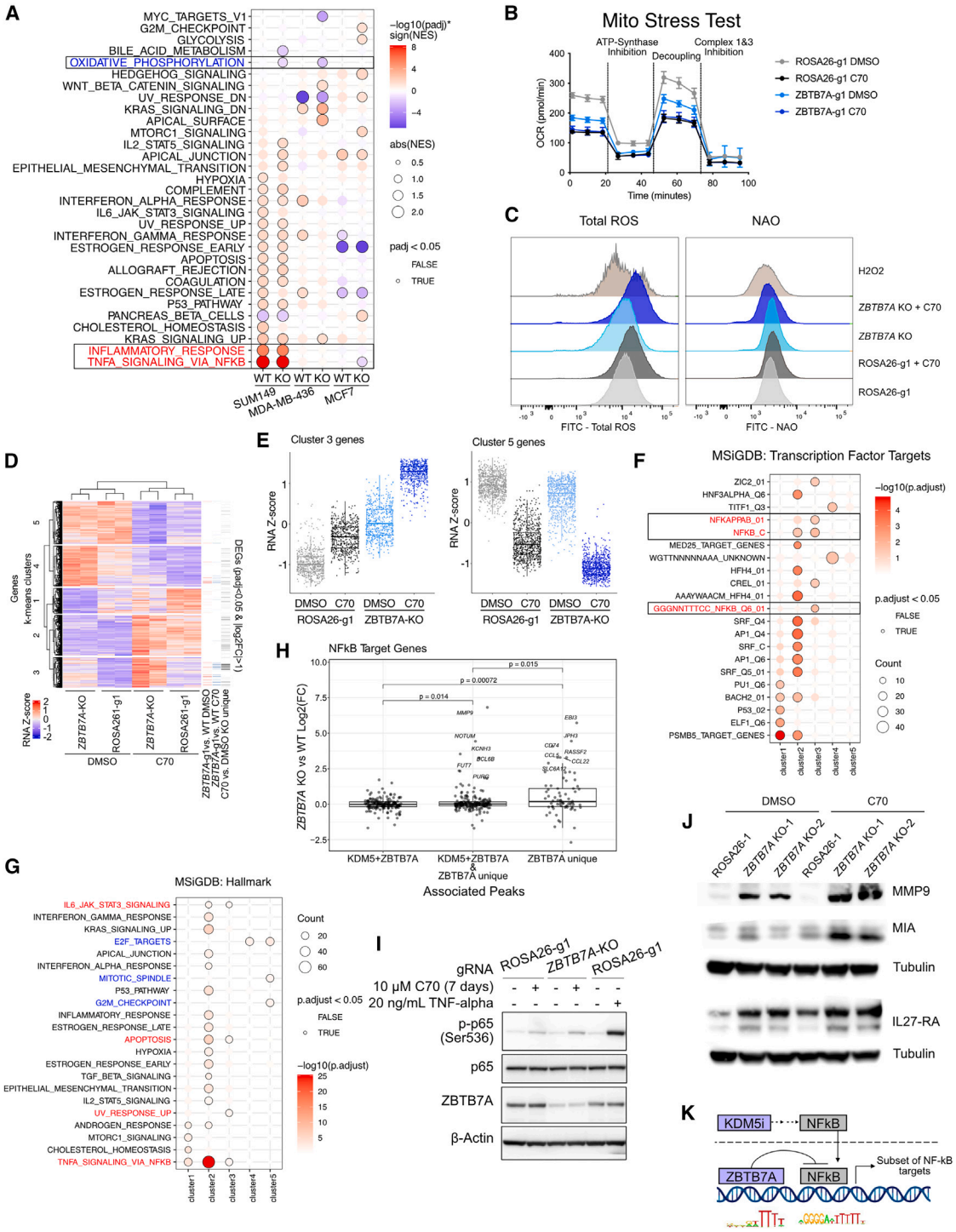

Figure 5. Effects of *ZBTB7A* KO on transcriptional response to KDM5 inhibition

(A) GSEA on genes ranked by log2(FC) for ±10 μM C70 for 7 days. The analysis was performed in all three cell lines with wild-type (i.e., ROSA26-g1) or *ZBTB7A* KO.

(B) Oxygen consumption rate (OCR) in ROSA26-g1 and *ZBTB7A* KO SUM149 cells ± pre-treatment with 10 μM C70 for 6 days. Values are the mean ± standard deviation. $N = 5$ for all conditions except ZBTB7A KO + C70, which had one outlier well removed ($N = 4$).

(C) Ridge plot depicting flow cytometry for total ROS detection with the Total Reactive Oxygen Species (ROS) Assay Kit and for mitochondrial cardiolipins with nonyl acridine orange (NAO). SUM149 cells were treated with or without 10 μM C70 for 5 days. One millimolar H_2O_2 (7 h for ROS and 2 h for NAO) was used as a positive control.

(legend continued on next page)

H3K4me3 signal was associated with increased gene expression (p = 3.48e−07 for BETA upregulated) (Figure S4E). Surprisingly, sites with increased H3K4me3 that coincide with decreased KDM5A binding had no correlation with gene expression (Figure S4E). In fact, diminished KDM5A signal intensity was significantly associated with a decrease in gene expression (Figures 4C and 4E, p = 4.45e−05 for BETA downregulated), implying that the KDM5A-ZBTB7A complex is a positive regulator of gene expression.

We next analyzed the predicted targets of the ZBTB7A and KDM5A/B overlapping, ZBTB7A unique, and KDM5A down peaks for enrichment of specific transcription factors or pathways. We defined direct targets as genes with a rank product <0.001 from the BETA output in Figures 4D and 4E.[32] The ZBTB7A transcription factor motif was evenly enriched between ZBTB7A unique and ZBTB7A and KDM5A/B overlapping peaks (Figure 4F). However, several transcription factors showed a bias toward one peak set. For example, NFKB1 was more significantly enriched among the ZBTB7A unique peak target genes, whereas HIF1A and E2F1::TFDP2 were more significantly enriched among the ZBTB7A and KDM5A/B overlapping target genes (Figure 4F). These observations support our analysis of the Hallmark gene set pathways (Figure 4G), in which HIF1A (e.g., hypoxia) and E2F-driven (e.g., E2F targets, G2M checkpoint, and mitotic spindle) pathways were specifically enriched among the ZBTB7A and KDM5A/B overlapping and KDM5A down gene targets, whereas immune pathways (e.g., allograft rejection, coagulation, and complement) were specifically enriched in the ZBTB7A unique peaks.

We also created *ZBTB7A* KOs in additional breast cancer cell lines (Figure S4F). MDA-MB-436 is another *BRCA1*-mutant TNBC cell line, like SUM149, with similar sensitivity to C70 (Figures S2A and S2B), and MCF7 is an ER$^+$, luminal breast cancer cell line. Similar to SUM149, deletion of *ZBTB7A* predominantly increased transcription in both MDA-MB-436 and MCF7 cells (Figure S4G). DEGs between parental and *ZBTB7A* KO cells in the SUM149 line showed similar trends in both MDA-MB-436 and MCF7 cell lines (Figures S4H and S4I). Upregulated DEGs from the SUM149 *ZBTB7A* KO cells were significantly enriched in both MDA-MB-436 ($p$adj = 2.7e−19, GSEA) and MCF7 ($p$adj = 7.8e−13, GSEA) ZBTB7A KOs (Figure S4J). However, downregulated DEGs from SUM149 cells were enriched only in the MDA-MB-436 *ZBTB7A* KO cells ($p$adj = 5.3e−3, GSEA) (Figure S4J).

To determine if *ZBTB7A* KO alters TNBC subtype-specific transcriptional states, we performed GSEA on the TNBC subtypes we previously described.[39] Mesenchymal and basal-specific genes were upregulated in the luminal MCF7 line, while the MDA-MB-436 mesenchymal-TNBC line showed upregulation of genes repressed in mesenchymal cells and downregulation of mesenchymal genes (Figure S4K). Finally, the basal-TNBC line SUM149 reactivated genes repressed in the basal state and turned on genes specific to mesenchymal and luminal-like TNBC (Figure S4K). Therefore, *ZBTB7A* may be an important regulator of cell state fidelity in breast cancer. Last, the most significantly upregulated pathways by C70 in the TNBC lines were related to immunity (e.g., allograft rejection, complement, inflammatory response), myogenesis, epithelial-to-mesenchymal transition, and IL-6/JAK/STAT3 in SUM149 cells and interferon-α response in the MDA-MB-436 cell line (Figure S4L).

These data show that ZBTB7A is an important regulator of epithelial cell differentiation-related processes and that some of its function is via modulation of KDM5A chromatin binding.

ZBTB7A and KDM5i co-regulate oxidative phosphorylation and NF-κB targets

To explore how loss of ZBTB7A alters the transcriptional response to KDM5i, we performed RNA-seq in WT and *ZBTB7A* KO cells ± 10 μM C70 for 7 days. We first observed that C70 treatment upregulates more DEGs ($p$adj < 0.05, |log2(FC)| > 1) in the *ZBTB7A* KO cells compared to WT controls across all three cell lines (SUM149, MDA-MB-436, and MCF7) (Figure S5A; Table S1). In addition, *ZBTB7A* KO did not change the gene targets of C70, since there was pronounced overlap in the DEGs induced in both WT and KO cells, at least in the two TNBC lines with a more limited overlap in MCF7 ER$^+$ luminal cells (Figure S5A). Therefore, loss of ZBTB7A may amplify response to C70 without completely rewiring its target genes in TNBC.

We next examined if C70 treatment modulated different pathways in the *ZBTB7A* KO cells (Figure 5A). GSEA in both SUM149 and MDA-MB-436 cells upon C70 treatment identified a reduction in oxidative phosphorylation specifically in the *ZBTB7A* KO and not in the WT cells (Figure 5A). Analysis of mitochondrial respiration in SUM149 WT and *ZBTB7A* KO cells ± 10 μM C70 showed that *ZBTB7A* KO and C70 diminished basal and maximum respiratory potential, and this decrease was saturated with C70 treatment and not further augmented by *ZBTB7A* KO (Figure 5B). Since dysfunctional mitochondria can be a source of ROS, we assessed total ROS levels and mitochondrial

(D) Heatmap of DEGs upon C70 treatment in either SUM149 ROSA26-g1 or *ZBTB7A*-g1 ($p$adj < 0.05). Genes are ordered based on k-means clustering (k = 5) and samples are ordered based on hierarchical clustering.
(E) RNA *Z* scores of cluster 3 and 5 genes from (D). Box plots represent mean, first and third quantile, and min and max values.
(F and G) Overrepresentation analysis for (F) MSigDB transcription factor targets and (G) MSigDB Hallmark pathways within each gene cluster specified by (D).
(H) Plot of NF-κB target genes associated with KDM5 + ZBTB7A peaks, ZBTB7A unique peaks, or both (KDM5 + ZBTB7A and ZBTB7A unique). Target genes were defined by the union of MSigDB transcription factor target gene sets (GGGNNTTTCC_NFKB_Q6_01, NFKAPPAB_01, NFKAPPAB65_01, NFKB_C, NFKB_Q6_01, and NFKB_Q6). The p value was determined by the t test. Box plots represent mean, first and third quantile, and min and max values.
(I) Immunoblot for phospho-NF-κB p65 (Ser536) in SUM149 ROSA26-g1 and *ZBTB7A* KO cells ± 10 μM C70 for 7 days. Cells treated with 20 ng/mL TNF-α for 5 min were used as positive control. Image is the left side part of a larger blot with additional lanes.
(J) Immunoblot for NF-κB targets MMP9, MIA, and IL-27-RA in SUM149 ROSA26-g1 or *ZBTB7A* KO cell lines ± 10 μM C70 for 6 days. Tubulin was used as loading control.
(K) Diagram of proposed interaction between ZBTB7A and KDM5 inhibition on NF-κB signaling.
See also Figures S4 and S5.

cardiolipins. We found higher ROS levels in both WT and *ZBTB7A* KO C70-treated cells compared to vehicle controls. However, ROS levels were higher within the *ZBTB7A* KO cells treated with C70 compared to WT (Figure 5C). In addition, nonyl acridine orange (NAO) staining to measure the abundance and redox status of mitochondrial cardiolipins showed no effect of C70 treatment in the WT cells but a decrease signal in the *ZBTB7A* KO cells, implying an increase in oxidized cardiolipins (Figure 5C).

To more globally analyze how *ZBTB7A* KO alters transcriptional response to C70, we re-clustered all DEGs upon C70 treatment in WT or *ZBTB7A* KO cells ($p$adj < 0.05) (Figure 5D). We then categorized the genes into five clusters, each with unique responses to ZBTB7A and/or C70 (Figures 5D, 5E, and S5B). Cluster 1 genes had a muted upregulation following C70 treatment in *ZBTB7A* KO cells compared to WT (Figure 5D), and they showed enrichment in mitochondrion-encoded genes (Figures S5C and S5D). We also assessed if upregulated genes are clustered to particular genomic regions potentially reflecting co-regulation due to shared enhancer activity. Only one cluster, cluster 2, displayed cytogenetic enrichment to a specific genomic region, 1q32 (Figure S5C). Among all clusters detected, cluster 3 was particularly prominent because it was enriched in genes differentially expressed due to either C70 treatment or *ZBTB7A* deletion (Figure 5D). These genes increased upon loss of ZBTB7A and had a further increase with C70 treatment (Figure 5E). When we analyzed each cluster for overlap with MSigDB transcription factor targets, cluster 3 was significantly enriched for NF-κB target genes (Figure 5F), which was also the transcription factor motif enriched among the predicted targets of ZBTB7A unique peaks (Figure 4F). To explore this in more detail, we analyzed changes in the expression of NF-κB targets in *ZBTB7A* KO cells compared to WT and found significantly higher expression of NF-κB targets associated with ZBTB7A unique compared to ZBTB7A and KDM5 overlapping peaks (Figure 5G).

When comparing each cluster to Hallmark gene sets, we found significant enrichment of TNF-α signaling via NF-κB, apoptosis, and IL-6/JAK/STAT3 signaling in both clusters 2 and 3, both of which show highest gene expression levels in the C70-treated *ZBTB7A* KO cells (Figures 5E, 5H, and S5B). Cluster 2 showed the most significant enrichment for TNF-α signaling via NF-κB even though the NF-κB transcription factor targets were specifically enriched in cluster 3 (Figures 5F and 5H).

To examine NF-κB activation after KDM5i and *ZBTB7A* KO, we assessed phospho(S536)-p65 and nuclear p65 levels and the activity of an NF-κB-driven GFP reporter. C70 increased phospho(S536)-p65 as well as marginally increasing nuclear p65 levels, with *ZBTB7A* KO having no observable effect (Figures 5I and S5E). Similarly, C70 induced GFP expression driven by a minimal NF-κB promoter, with no additive effect observed for the *ZBTB7A* KO (Figure S5F). However, immunoblot analysis of NF-κB targets selected from the overlapping topmost enriched genes in cluster 3 (Figure 5E) and NF-κB targets (Figure 5F) revealed that the expression of several proteins, including MMP9, MIA, and IL-27-RA, was significantly higher in ZBTB7A KO cells and upregulated by C70 (Figure 5J). Taken together, our data imply that KDM5i acts upstream and leads to the activation and nuclear localization of NF-κB. ZBTB7A, however, acts at the DNA level, in which ZBTB7A unique peaks repress a subset of NF-κB direct-target genes (Figure 5K).

In contrast to cluster 3 genes that were the most upregulated by C70 in ZBTB7A KO, cluster 5 genes had the largest decrease in expression in C70-treated *ZBTB7A* KO cells (Figures 5D and 5E). This cluster was specifically enriched for proliferative pathways, such as E2F targets, mitotic spindle, and G2M checkpoint (Figure 5G), which were the same pathways specifically enriched among KDM5A sites with diminished binding in the *ZBTB7A* KO (Figure 4G). Since these peaks were associated with activator function (Figure 4E), we hypothesize that ZBTB7A and KDM5A co-bound sites function as transcriptional activators of pro-proliferation pathways and that combined *ZBTB7A* KO and KDM5i leads to a stronger downregulation of these target genes.

Last, we reanalyzed our RNA-seq data for differential expression of endogenous retroelements with ERVmap because KDM5B was previously reported to derepress retroelements.[40] We found that KDM5i led to increased expression of endogenous retroelements (mostly LINEs [long interspersed nuclear elements] and SINEs [short interspersed nuclear elements]) in both the ROSA26-g1 control cells and all three KO derivates (Figure S5G; Table S6).[41] However, while 4,732 endogenous retroelements were significantly differentially expressed between DMSO- and C70-treated parental SUM149 cells (mostly upregulated), this number was much higher (12,097) in *ZBTB7A* KO and lower in *KDM5A* and *KDM5B* KO lines (4,072 and 2,474, respectively). In addition, we also noted that, in contrast to the limited changes seen in the expression of protein-coding genes in *KDM5A* KO cells, the expression of 2,143 endogenous retroelements was significantly different between KO and WT cells, whereas this was not seen in *KDM5B* KO (Table S6). Thus, some of the phenotypic consequences of C70 treatment and deletion of *KDM5* genes might be via their regulation of endogenous retroelement expression.

ZBTB7A expression alters KDM5-associated phenotypes in patient samples

We next tested if *ZBTB7A* expression altered KDM5-associated phenotypes in patient samples using the TCGA and METABRIC cohorts. Corroborating our findings in cell-line models, KDM5A/B expression was significantly positively correlated with proliferation (E2F targets, G2M checkpoint, and mitotic spindle) and negatively correlated with NF-κB and other inflammation-related pathways (Figure 6A). In addition, these correlations were stronger among samples with low *ZBTB7A* expression. Analysis of TNBC samples from the METABRIC cohort also demonstrated that KDM5A/B expression is more strongly associated with many of the select pathways in *ZBTB7A*-low samples, but the differences were less prominent (Figure 6B).

Due to the significant inverse association between KDM5A/B expression and inflammation-related pathways, we also assessed the correlation between *KDM5A*, *KDM5B*, or *ZBTB7A* expression with estimated immune infiltration scores among basal breast cancer samples in the TCGA cohort. We found that *ZBTB7A* was significantly positively correlated with immune infiltration, *KDM5B* was negatively correlated, and *KDM5A* had no association (Figure 6C).

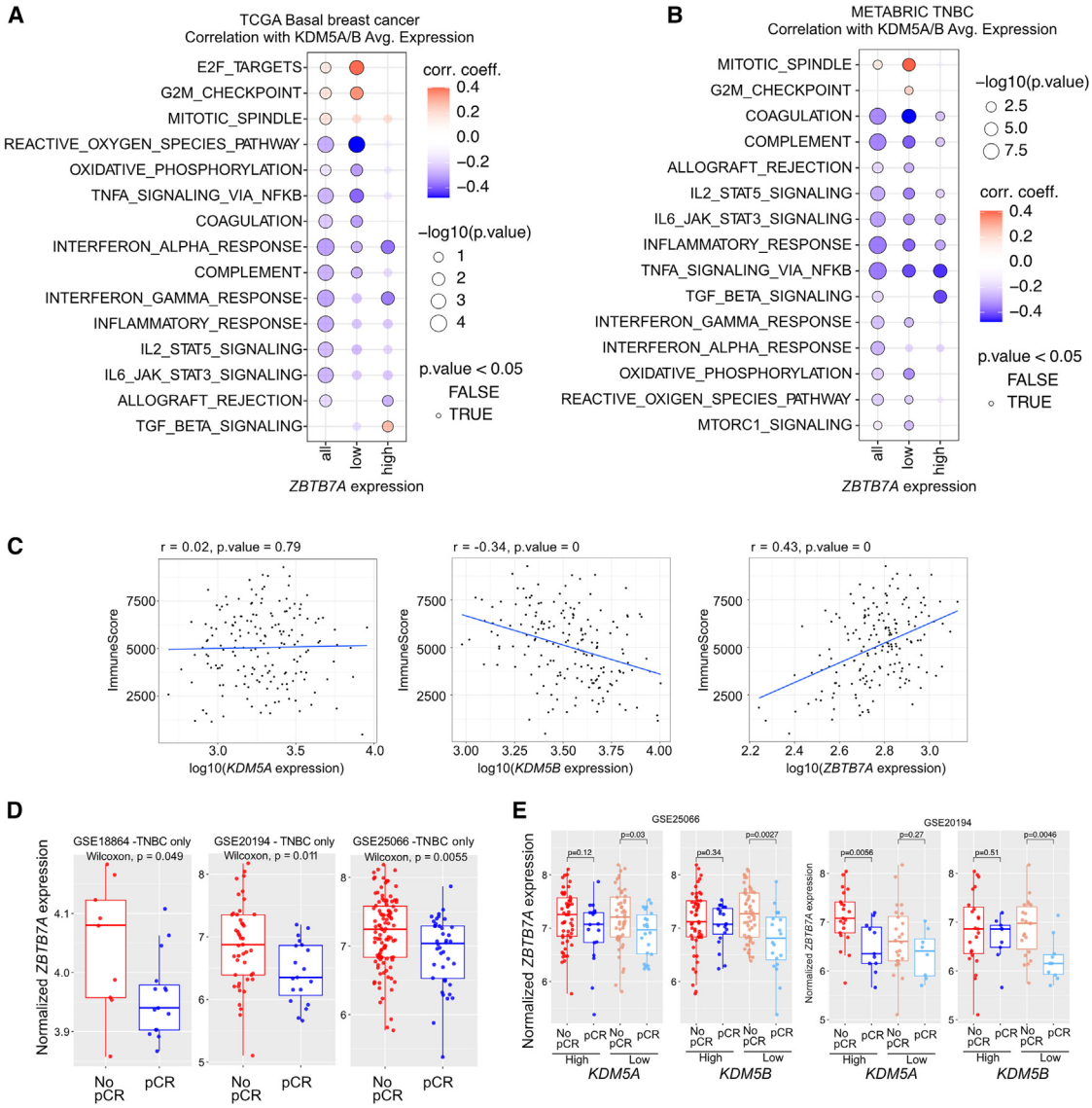

Figure 6. Associations between *ZBTB7A* and KDM5 expression and tumor features in patient samples

(A and B) Correlation between *KDM5A/B* expression and select pathways across basal tumors from TCGA (A) and TNBC samples from METABRIC (B). Correlation coefficients and −log10(*p*) are plotted. The samples were subset into high and low *ZBTB7A* expression based on upper and lower tertiles.

(C) Correlation between KDM5A, KDM5B, and ZBTB7A expression with estimated immune infiltration scores from bulk RNA-seq data. Data are from basal tumors in TCGA. Immune scores were calculated from bulk RNA-seq via "Estimation of Stromal and Immune cells in Malignant Tumors Using Expression Data" (ESTIMATE).

(D) Boxplots depicting the expression of *ZBTB7A* in TNBC from patients with pCR or no pCR from the indicated cohorts. Box plots represent mean, first and third quantile, and min and max values. Mann-Whitney U test was used.

(E) Boxplots depicting the expression of *ZBTB7A* in breast tumors from patients with pCR or no pCR from the indicated cohorts and divided based on the expression levels of *KDM5A* or *KDM5B*. Box plots represent mean, first and third quantile, and min and max values. Mann-Whitney U test was used.

Finally, we wanted to determine if *ZBTB7A* expression modified response to neoadjuvant chemotherapy by itself or associated with KDM5 expression. We found that the expression of *ZBTB7A* in TNBC was significantly higher in tumors from patients who did not achieve pathologic complete response (pCR) in three independent cohorts (Figure 6D).[42–44] The association of higher ZBTB7A expression with lack of pCR was significant only in tumors with lower expression of *KDM5B*, whereas for *KDM5A* this was less consistent (Figure 6E).

These analyses of clinical samples validate our findings in the cell-line models and confirm the role for ZBTB7A as a transcriptional modulator of NF-κB and inflammation-related pathways.

DISCUSSION

Through CRISPR KO viability screens ± C70 KDM5 inhibitor, we identified several factors that modulate sensitivity to KDM5i in basal breast cancer, including ZBTB7A. We demonstrated that

ZBTB7A interacts and co-localizes with KDM5A/B at genomic regions with high H3K4me3 levels and that a subset of KDM5A binding might be ZBTB7A dependent.

Functional differences between the KDM5 paralogs have been described previously, but the underlying mechanism remains unresolved.[45] For example, KDM5A and not KDM5B was found to promote MYC-driven transcription in multiple myeloma by altering RNA polymerase II (RNAPII) promoter-proximal pausing,[22] while KDM5B was specifically found to suppress endogenous retroelement expression in melanoma by recruiting the H3K9 methyltransferase SETDB1.[40] Our work provides some mechanistic insight into these distinctions, in which we found significant differences in genomic binding between KDM5A and KDM5B. Specifically, KDM5A was primarily restricted to promoters, whereas KDM5B exhibited extensive binding across both promoter and non-promoter regions. This indicates that KDM5A could be a promoter-specific regulator of transcription in agreement with prior findings that KDM5A is a key modulator of RNAPII pausing at MYC-driven promoters.[22] In addition, the intergenic binding of KDM5B could explain why this paralog was found to regulate endogenous retroelement expression in melanoma,[40] supporting our data in SUM149 cells. Further investigation into the intergenic KDM5B peaks in our study unveiled an association with the cohesin/CTCF complex, indicating a potential role of KDM5B in the regulation of chromatin topology. This finding is particularly intriguing in the context of previous research from our lab, which demonstrated that KDM5B physically associates with CTCF.[7] Overall, our results indicate that distinct genomic binding patterns may contribute, at least in part, to paralog-specific KDM5 activity, but further work is needed to elucidate the underlying mechanisms.

ZBTB7A has previously been described as a key regulator of metabolism in leukemias, where loss of ZBTB7A increased glycolysis and sensitized to glycolytic inhibition.[46–48] Here, we identified ZBTB7A as a regulator of oxidative phosphorylation in TNBC and propose that this may contribute to increased KDM5 inhibitor sensitivity upon loss of ZBTB7A. Initially, we found that peaks with decreased KDM5A binding in the *ZBTB7A* KO were significantly enriched for downstream targets of the NRF1 transcription factor, a regulator of nuclear genes essential for both respiration and mitochondrial DNA transcription.[37] Several observations support the hypothesis that reduced mitochondrial respiration can sensitize cells to KDM5i. First, our C70-resistant derivative cell line significantly upregulated oxidative phosphorylation genes, especially members of the electron transport chain. Second, prior studies found that melanoma cells with high *KDM5B* expression had an increased reliance on mitochondrial respiration.[49] Inhibition of ATP synthase decreased the emergence of cells with high *KDM5B* expression after treatment with a panel of anti-cancer drugs, and *KDM5B* overexpression led to increased oxygen consumption and mitochondrial ATP production.[49] This potential link between mitochondrial activity and KDM5 inhibitor sensitivity is interesting given that α-ketoglutarate, a key product of the TCA cycle, is a required co-factor for KDM5 demethylase activity. In addition, since the KDM5 inhibitor C70 is an α-ketoglutarate competitor,[16] altering α-ketoglutarate levels could alter the effective concentration of C70.

Mitochondrial dysfunction can also contribute to ROS and oxidative stress. We found that C70 treatment induced ROS production in both WT and *ZBTB7A* KO cells. However, ROS levels were higher within the *ZBTB7A* KO treated with C70. This is in line with previous observations in which ZBTB7A was found to protect against oxidative stress to promote cell survival during viral infection.[50] It also agrees with previous work where KDM5A was found to mitigate the accumulation of ROS and protect against defects in mitochondrial membrane potential in response to cisplatin treatment.[51] Interestingly, regulation of mitochondrial activity via KDM5s may be evolutionarily conserved, in that *Drosophila* KDM5/Lid was identified as a direct activator of genes required for mitochondrial structure/function, and mutant KDM5/Lid led to elevated ROS production.[52] Taken together, these results indicate that both ZBTB7A and KDM5 activity may protect against oxidative damage and that loss of both could have a compounding effect on cell viability.

Last, we found that both KDM5i and loss of ZBTB7A led to an induction of NF-κB target genes and that the NF-κB pathway was depleted in the C70-resistant SUM149CR cell line. We hypothesize that KDM5 activity and ZBTB7A may influence NF-κB signaling through distinct mechanisms. First, KDM5i may act upstream, since C70 increased phosphorylated p65 (Ser536), led to slightly elevated levels of p65 in the nucleus, and induced GFP expression driven by a minimal NF-κB binding motif. It is unclear how inhibition of KDM5 activity activates NF-κB, but previous research implicates the DNA-sensing cGAS-STING pathway, an upstream activator of NF-κB signaling.[40,53] *KDM5B*, but not *KDM5A* KO, was found to derepress STING expression and induce interferon signaling in breast cancer cell lines with high cytosolic DNA levels.[53] Similarly, *KDM5B* KO was found to increase tumor immunogenicity through the derepression of retroelements and subsequent activation of cGAS-STING.[40] Aligned with these findings, our RNA-seq data revealed a significant increase in retroelement expression after C70 treatment. In contrast, we hypothesize that ZBTB7A regulates NF-κB at the DNA level, whereby ZBTB7A binding represses nearby NF-κB target genes. Supporting this hypothesis, we found that the targets of ZBTB7A unique binding sites were significantly enriched for the *NFKB1* transcription factor motif.

Given that NF-κB is generally a pro-survival pathway that activates anti-apoptotic factors and cell-cycle-promoting genes, it was unexpected to see this pathway diminished and less responsive to C70 in the SUM149CR C70-resistant cell line. However, there are several reports indicating that NF-κB could both inhibit and promote cell death depending on the context and type of stressor placed on the cell.[54,55] Most relevantly, NF-κB signaling enhanced oxidative-stress-induced killing with H_2O_2.[54] Therefore, increased NF-κB activity could render the cells more sensitive to increased ROS observed with *ZBTB7A* KO and C70 treatment. Cells adapt to long-term ROS by upregulating antioxidant defense mechanisms.[56] Thus, the upregulation of MMP9, an NF-κB target that has been shown to protect from ROS in some cellular contexts,[57] in *ZBTB7A* KO cells could reflect such a coping mechanism.

Limitations of the study

Our study was performed in human breast cancer cell lines with validation of findings in clinical samples. However, we do not

know to what degree cell lines and cell culture reflect the physiological conditions in human breast cancer, which is especially a concern for changes in metabolic pathways. A limitation of the experiments using KO cell lines is that the consequences of short-term and long-term deletion of a gene can be different, as we have seen previously for *KDM5B*.[10] Thus, while *KDM5A* deletion in the CRISPR screen (relatively short-term assay and assessing more acute loss of *KMD5A*) may have decreased response to C70, this effect is lost in the stable *KDM5A* KO cell line used for validation.

The KDM5 inhibitor we used blocks the activity of all KDM5 family members. Further studies would be required to assess the effects of the specific inhibition of KDM5A or KDM5B in human breast tumors.

RESOURCE AVAILABILITY

Lead contact

Requests for further information and resources and reagents should be directed to and will be fulfilled by the lead contact, Kornelia Polyak, Dana-Farber Cancer Institute, 450 Brookline Avenue, SM1070B, Boston, MA 02215, USA (kornelia_polyak@dfci.harvard.edu).

Materials availability

Breast cancer cell line derivatives will be made available upon request and following the execution of an MTA.

Data and code availability

All data needed to evaluate the conclusions in the paper are present in the paper and/or the supplemental information. All raw genomic data were deposited with GEO under accession no. GSE259252. This study did not generate custom code. The raw mass spectrometry data have been deposited in the public proteomics repository MassIVE (http://massive.ucsd.edu) using the identifier MSV000094452. The data should be accessible at ftp://massive.ucsd.edu/v07/MSV000094452. Any additional information required to reanalyze the data reported in this work paper is available from the lead contact upon request.

ACKNOWLEDGMENTS

We thank members of our laboratories for their critical reading of the manuscript and useful discussions. We thank the Dana-Farber Cancer Institute Molecular Biology Core Facility for their outstanding sequencing service. This research was supported by National Cancer Institute R35 CA197623 (K.P.) and P01 CA250959 (K.P., H.W.L., and M.B.), by the Ludwig Center at Harvard (K.P.), and in part by the Intramural Research Program of the National Center for Advancing Translational Sciences (NCATS), National Institutes of Health (A.S., S.C.K., G.R., M.L.-N., and A.J). The content is solely the responsibility of the authors and does not necessarily represent the official views of the National Institutes of Health.

AUTHOR CONTRIBUTIONS

Conceptualization, B.D. and K.P.; methodology, B.D., C.S.D'S., A.H.R., E.K.P., and M.P.; analyses, B.D., E.K.P., M.P., Z.L., X.Q., R.L., and Y.J.; investigation, B.D., M.S., A.P., T.B., P.F., J.N., and X.-Y.H.; resources, J.S.C., A.S., S.C.K., G.R., M.L.-N., A.J., M.B., and H.W.L.; writing—original draft, B.D. and K.P.; writing—review & editing, all authors; funding acquisition, K.P.; supervision, J.S.C., H.W.L., and K.P.

DECLARATION OF INTERESTS

K.P. serves on the scientific advisory boards of Ideaya Biosciences and Scorpion Therapeutics, holds equity options in Scorpion Therapeutics and Ideaya Biosciences, and receives sponsored research funding from Novartis, where she also consults. H.W.L. receives research funding from Novartis.

STAR★METHODS

Detailed methods are provided in the online version of this paper and include the following:

- KEY RESOURCES TABLE
- EXPERIMENTAL MODEL AND STUDY PARTICIPANT DETAILS
  - Breast cancer cohort data
  - Breast cancer cell lines and derivation of the C70-resistant model
  - CRISPR libraries
- METHOD DETAILS
  - Cellular viability and growth assays
  - CRISPR screen and data analyses
  - Generation of single CRISPR/Cas9 knock-out cells
  - Generation of NFkB reporter cells
  - ChIP-seq
  - RNA-seq
  - qPLEX-RIME
  - Antibodies and inhibitors
  - Immunoblotting and immunoprecipitation experiments
  - Mass spectrometry analysis of histone modifications
  - scRNA-seq library prep
  - Flow cytometry experiments
  - Mito-Stress Test
- QUANTIFICATION AND STATISTICAL ANALYSIS
  - Software used in this study
  - ChIP-seq data analysis
  - RNA-seq data analysis
  - Endogenous retroelement expression analysis
  - CRISPR screen data analysis
  - scRNA-seq data analysis
  - qPLEX RIME data analysis

SUPPLEMENTAL INFORMATION

Supplemental information can be found online at https://doi.org/10.1016/j.celrep.2024.114991.

Received: April 11, 2024
Revised: August 7, 2024
Accepted: November 1, 2024
Published: November 20, 2024

REFERENCES

1. Feinberg, A.P., Koldobskiy, M.A., and Göndör, A. (2016). Epigenetic modulators, modifiers and mediators in cancer aetiology and progression. Nat. Rev. Genet. *17*, 284–299. https://doi.org/10.1038/nrg.2016.13.
2. Flavahan, W.A., Gaskell, E., and Bernstein, B.E. (2017). Epigenetic plasticity and the hallmarks of cancer. Science *357*, eaal2380. https://doi.org/10.1126/science.aal2380.
3. Shen, C., and Vakoc, C.R. (2015). Gain-of-function mutation of chromatin regulators as a tumorigenic mechanism and an opportunity for therapeutic intervention. Curr. Opin. Oncol. *27*, 57–63. https://doi.org/10.1097/CCO.0000000000000151.
4. Hinohara, K., and Polyak, K. (2019). Intratumoral Heterogeneity: More Than Just Mutations. Trends Cell Biol. *29*, 569–579. https://doi.org/10.1016/j.tcb.2019.03.003.
5. Yuan, S., Norgard, R.J., and Stanger, B.Z. (2019). Cellular Plasticity in Cancer. Cancer Discov. *9*, 837–851. https://doi.org/10.1158/2159-8290.CD-19-0015.
6. Perou, C.M., Sørlie, T., Eisen, M.B., van de Rijn, M., Jeffrey, S.S., Rees, C.A., Pollack, J.R., Ross, D.T., Johnsen, H., Akslen, L.A., et al. (2000).

Molecular portraits of human breast tumours. Nature *406*, 747–752. https://doi.org/10.1038/35021093.

7. Yamamoto, S., Wu, Z., Russnes, H.G., Takagi, S., Peluffo, G., Vaske, C., Zhao, X., Moen Vollan, H.K., Maruyama, R., Ekram, M.B., et al. (2014). JARID1B is a luminal lineage-driving oncogene in breast cancer. Cancer Cell *25*, 762–777. https://doi.org/10.1016/j.ccr.2014.04.024.

8. Zou, M.R., Cao, J., Liu, Z., Huh, S.J., Polyak, K., and Yan, Q. (2014). Histone demethylase jumonji AT-rich interactive domain 1B (JARID1B) controls mammary gland development by regulating key developmental and lineage specification genes. J. Biol. Chem. *289*, 17620–17633. https://doi.org/10.1074/jbc.M114.570853.

9. Choi, H.J., Joo, H.S., Won, H.Y., Min, K.W., Kim, H.Y., Son, T., Oh, Y.H., Lee, J.Y., and Kong, G. (2018). Role of RBP2-Induced ER and IGF1R-ErbB Signaling in Tamoxifen Resistance in Breast Cancer. J. Natl. Cancer Inst. *110*, 400. https://doi.org/10.1093/jnci/djx207.

10. Hinohara, K., Wu, H.J., Vigneau, S., McDonald, T.O., Igarashi, K.J., Yamamoto, K.N., Madsen, T., Fassl, A., Egri, S.B., Papanastasiou, M., et al. (2018). KDM5 Histone Demethylase Activity Links Cellular Transcriptomic Heterogeneity to Therapeutic Resistance. Cancer Cell *34*, 939–953.e9. https://doi.org/10.1016/j.ccell.2018.10.014.

11. Cao, J., Liu, Z., Cheung, W.K.C., Zhao, M., Chen, S.Y., Chan, S.W., Booth, C.J., Nguyen, D.X., and Yan, Q. (2014). Histone demethylase RBP2 is critical for breast cancer progression and metastasis. Cell Rep. *6*, 868–877. https://doi.org/10.1016/j.celrep.2014.02.004.

12. Klein, B.J., Piao, L., Xi, Y., Rincon-Arano, H., Rothbart, S.B., Peng, D., Wen, H., Larson, C., Zhang, X., Zheng, X., et al. (2014). The histone-H3K4-specific demethylase KDM5B binds to its substrate and product through distinct PHD fingers. Cell Rep. *6*, 325–335. https://doi.org/10.1016/j.celrep.2013.12.021.

13. Li, Q., Shi, L., Gui, B., Yu, W., Wang, J., Zhang, D., Han, X., Yao, Z., and Shang, Y. (2011). Binding of the JmjC demethylase JARID1B to LSD1/NuRD suppresses angiogenesis and metastasis in breast cancer cells by repressing chemokine CCL14. Cancer Res. *71*, 6899–6908. https://doi.org/10.1158/0008-5472.CAN-11-1523.

14. Hou, J., Wu, J., Dombkowski, A., Zhang, K., Holowatyj, A., Boerner, J.L., and Yang, Z.Q. (2012). Genomic amplification and a role in drug-resistance for the KDM5A histone demethylase in breast cancer. Am. J. Transl. Res. *4*, 247–256.

15. Liu, H., Liu, L., Holowatyj, A., Jiang, Y., and Yang, Z.Q. (2016). Integrated genomic and functional analyses of histone demethylases identify oncogenic KDM2A isoform in breast cancer. Mol. Carcinog. *55*, 977–990. https://doi.org/10.1002/mc.22341.

16. Johansson, C., Velupillai, S., Tumber, A., Szykowska, A., Hookway, E.S., Nowak, R.P., Strain-Damerell, C., Gileadi, C., Philpott, M., Burgess-Brown, N., et al. (2016). Structural analysis of human KDM5B guides histone demethylase inhibitor development. Nat. Chem. Biol. *12*, 539–545. https://doi.org/10.1038/nchembio.2087.

17. Paroni, G., Bolis, M., Zanetti, A., Ubezio, P., Helin, K., Staller, P., Gerlach, L.O., Fratelli, M., Neve, R.M., Terao, M., and Garattini, E. (2019). HER2-positive breast-cancer cell lines are sensitive to KDM5 inhibition: definition of a gene-expression model for the selection of sensitive cases. Oncogene *38*, 2675–2689. https://doi.org/10.1038/s41388-018-0620-6.

18. Maeda, T., Hobbs, R.M., and Pandolfi, P.P. (2005). The transcription factor Pokemon: a new key player in cancer pathogenesis. Cancer Res. *65*, 8575–8578. https://doi.org/10.1158/0008-5472.CAN-05-1055.

19. Lunardi, A., Guarnerio, J., Wang, G., Maeda, T., and Pandolfi, P.P. (2013). Role of LRF/Pokemon in lineage fate decisions. Blood *121*, 2845–2853. https://doi.org/10.1182/blood-2012-11-292037.

20. Constantinou, C., Spella, M., Chondrou, V., Patrinos, G.P., Papachatzopoulou, A., and Sgourou, A. (2019). The multi-faceted functioning portrait of LRF/ZBTB7A. Hum. Genomics *13*, 66. https://doi.org/10.1186/s40246-019-0252-0.

21. Blumbach, K., Zweers, M.C., Brunner, G., Peters, A.S., Schmitz, M., Schulz, J.N., Schild, A., Denton, C.P., Sakai, T., Fässler, R., et al. (2010). Defective granulation tissue formation in mice with specific ablation of integrin-linked kinase in fibroblasts - role of TGFbeta1 levels and RhoA activity. J. Cell Sci. *123*, 3872–3883. https://doi.org/10.1242/jcs.063024.

22. Ohguchi, H., Park, P.M.C., Wang, T., Gryder, B.E., Ogiya, D., Kurata, K., Zhang, X., Li, D., Pei, C., Masuda, T., et al. (2021). Lysine Demethylase 5A is Required for MYC Driven Transcription in Multiple Myeloma. Blood Cancer Discov. *2*, 370–387. https://doi.org/10.1158/2643-3230.BCD-20-0108.

23. Helmlinger, D., and Tora, L. (2017). Sharing the SAGA. Trends Biochem. Sci. *42*, 850–861. https://doi.org/10.1016/j.tibs.2017.09.001.

24. Liu, C.J., Prazak, L., Fajardo, M., Yu, S., Tyagi, N., and Di Cesare, P.E. (2004). Leukemia/lymphoma-related factor, a POZ domain-containing transcriptional repressor, interacts with histone deacetylase-1 and inhibits cartilage oligomeric matrix protein gene expression and chondrogenesis. J. Biol. Chem. *279*, 47081–47091. https://doi.org/10.1074/jbc.M405288200.

25. Pavlenko, E., Ruengeler, T., Engel, P., and Poepsel, S. (2022). Functions and Interactions of Mammalian KDM5 Demethylases. Front. Genet. *13*, 906662. https://doi.org/10.3389/fgene.2022.906662.

26. Stark, C., Breitkreutz, B.J., Reguly, T., Boucher, L., Breitkreutz, A., and Tyers, M. (2006). BioGRID: a general repository for interaction datasets. Nucleic Acids Res. *34*, D535–D539. https://doi.org/10.1093/nar/gkj109.

27. Oughtred, R., Rust, J., Chang, C., Breitkreutz, B.J., Stark, C., Willems, A., Boucher, L., Leung, G., Kolas, N., Zhang, F., et al. (2021). The BioGRID database: A comprehensive biomedical resource of curated protein, genetic, and chemical interactions. Protein Sci. *30*, 187–200. https://doi.org/10.1002/pro.3978.

28. Szklarczyk, D., Morris, J.H., Cook, H., Kuhn, M., Wyder, S., Simonovic, M., Santos, A., Doncheva, N.T., Roth, A., Bork, P., et al. (2017). The STRING database in 2017: quality-controlled protein-protein association networks, made broadly accessible. Nucleic Acids Res. *45*, D362–D368. https://doi.org/10.1093/nar/gkw937.

29. Nishibuchi, G., Shibata, Y., Hayakawa, T., Hayakawa, N., Ohtani, Y., Sinmyozu, K., Tagami, H., and Nakayama, J.-I. (2014). Physical and Functional Interactions between the Histone H3K4 Demethylase KDM5A and the Nucleosome Remodeling and Deacetylase (NuRD) Complex. J. Biol. Chem. *289*, 28956–28970. https://doi.org/10.1074/jbc.m114.573725.

30. Choi, W.I., Jeon, B.N., Yoon, J.H., Koh, D.I., Kim, M.H., Yu, M.Y., Lee, K.M., Kim, Y., Kim, K., Hur, S.S., et al. (2013). The proto-oncoprotein FBI-1 interacts with MBD3 to recruit the Mi-2/NuRD-HDAC complex and BCoR and to silence p21WAF/CDKN1A by DNA methylation. Nucleic Acids Res. *41*, 6403–6420. https://doi.org/10.1093/nar/gkt359.

31. Papachristou, E.K., Kishore, K., Holding, A.N., Harvey, K., Roumeliotis, T.I., Chilamakuri, C.S.R., Omarjee, S., Chia, K.M., Swarbrick, A., Lim, E., et al. (2018). A quantitative mass spectrometry-based approach to monitor the dynamics of endogenous chromatin-associated protein complexes. Nat. Commun. *9*, 2311. https://doi.org/10.1038/s41467-018-04619-5.

32. Wang, S., Sun, H., Ma, J., Zang, C., Wang, C., Wang, J., Tang, Q., Meyer, C.A., Zhang, Y., and Liu, X.S. (2013). Target analysis by integration of transcriptome and ChIP-seq data with BETA. Nat. Protoc. *8*, 2502–2515. https://doi.org/10.1038/nprot.2013.150.

33. Liu, T., Ortiz, J.A., Taing, L., Meyer, C.A., Lee, B., Zhang, Y., Shin, H., Wong, S.S., Ma, J., Lei, Y., et al. (2011). Cistrome: an integrative platform for transcriptional regulation studies. Genome Biol. *12*, R83. https://doi.org/10.1186/gb-2011-12-8-r83.

34. Layer, R.M., Pedersen, B.S., DiSera, T., Marth, G.T., Gertz, J., and Quinlan, A.R. (2018). GIGGLE: a search engine for large-scale integrated genome analysis. Nat. Methods *15*, 123–126. https://doi.org/10.1038/nmeth.4556.

35. Yu, H., Pardoll, D., and Jove, R. (2009). STATs in cancer inflammation and immunity: a leading role for STAT3. Nat. Rev. Cancer *9*, 798–809. https://doi.org/10.1038/nrc2734.

36. Ren, R., Horton, J.R., Chen, Q., Yang, J., Liu, B., Huang, Y., Blumenthal, R.M., Zhang, X., and Cheng, X. (2023). Structural basis for transcription factor ZBTB7A recognition of DNA and effects of ZBTB7A somatic mutations that occur in human acute myeloid leukemia. J. Biol. Chem. *299*, 102885. https://doi.org/10.1016/j.jbc.2023.102885.

37. Scarpulla, R.C. (2008). Transcriptional paradigms in mammalian mitochondrial biogenesis and function. Physiol. Rev. *88*, 611–638. https://doi.org/10.1152/physrev.00025.2007.

38. Zheng, R., Wan, C., Mei, S., Qin, Q., Wu, Q., Sun, H., Chen, C.H., Brown, M., Zhang, X., Meyer, C.A., and Liu, X.S. (2019). Cistrome Data Browser: expanded datasets and new tools for gene regulatory analysis. Nucleic Acids Res. *47*, D729–D735. https://doi.org/10.1093/nar/gky1094.

39. Jovanovic, B., Temko, D., Stevens, L.E., Seehawer, M., Fassl, A., Murphy, K., Anand, J., Garza, K., Gulvady, A., Qiu, X., et al. (2023). Heterogeneity and transcriptional drivers of triple-negative breast cancer. Cell Rep. *42*, 113564. https://doi.org/10.1016/j.celrep.2023.113564.

40. Zhang, S.M., Cai, W.L., Liu, X., Thakral, D., Luo, J., Chan, L.H., McGeary, M.K., Song, E., Blenman, K.R.M., Micevic, G., et al. (2021). KDM5B promotes immune evasion by recruiting SETDB1 to silence retroelements. Nature *598*, 682–687. https://doi.org/10.1038/s41586-021-03994-2.

41. Tokuyama, M., Kong, Y., Song, E., Jayewickreme, T., Kang, I., and Iwasaki, A. (2018). ERVmap analysis reveals genome-wide transcription of human endogenous retroviruses. Proc. Natl. Acad. Sci. USA *115*, 12565–12572. https://doi.org/10.1073/pnas.1814589115.

42. Hatzis, C., Pusztai, L., Valero, V., Booser, D.J., Esserman, L., Lluch, A., Vidaurre, T., Holmes, F., Souchon, E., Wang, H., et al. (2011). A genomic predictor of response and survival following taxane-anthracycline chemotherapy for invasive breast cancer. JAMA *305*, 1873–1881. https://doi.org/10.1001/jama.2011.593.

43. Popovici, V., Chen, W., Gallas, B.G., Hatzis, C., Shi, W., Samuelson, F.W., Nikolsky, Y., Tsyganova, M., Ishkin, A., Nikolskaya, T., et al. (2010). Effect of training-sample size and classification difficulty on the accuracy of genomic predictors. Breast Cancer Res. *12*, R5. https://doi.org/10.1186/bcr2468.

44. Silver, D.P., Richardson, A.L., Eklund, A.C., Wang, Z.C., Szallasi, Z., Li, Q., Juul, N., Leong, C.O., Calogrias, D., Buraimoh, A., et al. (2010). Efficacy of neoadjuvant Cisplatin in triple-negative breast cancer. J. Clin. Oncol. *28*, 1145–1153. https://doi.org/10.1200/JCO.2009.22.4725.

45. Yoo, J., Kim, G.W., Jeon, Y.H., Kim, J.Y., Lee, S.W., and Kwon, S.H. (2022). Drawing a line between histone demethylase KDM5A and KDM5B: their roles in development and tumorigenesis. Exp. Mol. Med. *54*, 2107–2117. https://doi.org/10.1038/s12276-022-00902-0.

46. Redondo Monte, E., Kerbs, P., and Greif, P.A. (2020). ZBTB7A links tumor metabolism to myeloid differentiation. Exp. Hematol. *87*, 20–24.e1. https://doi.org/10.1016/j.exphem.2020.05.010.

47. Redondo Monte, E., Wilding, A., Leubolt, G., Kerbs, P., Bagnoli, J., Hiddemann, W., Enard, W., Theurich, S., and Greif, P.A. (2019). Loss of ZBTB7A Enhances Glycolysis and Beta Oxidation in Myeloid Leukemia. Blood *134*, 1453. https://doi.org/10.1182/blood-2019-128378.

48. Redondo Monte, E., Wilding, A., Leubolt, G., Kerbs, P., Bagnoli, J.W., Hartmann, L., Hiddemann, W., Chen-Wichmann, L., Krebs, S., Blum, H., et al. (2020). ZBTB7A prevents RUNX1-RUNX1T1-dependent clonal expansion of human hematopoietic stem and progenitor cells. Oncogene *39*, 3195–3205. https://doi.org/10.1038/s41388-020-1209-4.

49. Roesch, A., Vultur, A., Bogeski, I., Wang, H., Zimmermann, K.M., Speicher, D., Körbel, C., Laschke, M.W., Gimotty, P.A., Philipp, S.E., et al. (2013). Overcoming Intrinsic Multidrug Resistance in Melanoma by Blocking the Mitochondrial Respiratory Chain of Slow-Cycling JARID1B-high Cells. Cancer Cell *23*, 811–825. https://doi.org/10.1016/j.ccr.2013.05.003.

50. Zhu, X., Trimarco, J.D., Williams, C.A., Barrera, A., Reddy, T.E., and Heaton, N.S. (2022). ZBTB7A promotes virus-host homeostasis during human coronavirus 229E infection. Cell Rep. *41*, 111540. https://doi.org/10.1016/j.celrep.2022.111540.

51. Liu, C., Zheng, Z., Li, W., Tang, D., Zhao, L., He, Y., and Li, H. (2022). Inhibition of KDM5A attenuates cisplatin-induced hearing loss via regulation of the MAPK/AKT pathway. Cell. Mol. Life Sci. *79*, 596. https://doi.org/10.1007/s00018-022-04565-y.

52. Liu, X., and Secombe, J. (2015). The Histone Demethylase KDM5 Activates Gene Expression by Recognizing Chromatin Context through Its PHD Reader Motif. Cell Rep. *13*, 2219–2231. https://doi.org/10.1016/j.celrep.2015.11.007.

53. Wu, L., Cao, J., Cai, W.L., Lang, S.M., Horton, J.R., Jansen, D.J., Liu, Z.Z., Chen, J.F., Zhang, M., Mott, B.T., et al. (2018). KDM5 histone demethylases repress immune response via suppression of STING. PLoS Biol. *16*, e2006134. https://doi.org/10.1371/journal.pbio.2006134.

54. Kaltschmidt, B., Kaltschmidt, C., Hofmann, T.G., Hehner, S.P., Dröge, W., and Schmitz, M.L. (2000). The pro- or anti-apoptotic function of NF-κB is determined by the nature of the apoptotic stimulus. Eur. J. Biochem. *267*, 3828–3835. https://doi.org/10.1046/j.1432-1327.2000.01421.x.

55. Baichwal, V.R., and Baeuerle, P.A. (1997). Apoptosis: Activate NF-κB or die? Curr. Biol. *7*, R94–R96. https://doi.org/10.1016/s0960-9822(06)00046-7.

56. Pickering, A.M., Vojtovich, L., Tower, J., and A Davies, K.J. (2013). Oxidative stress adaptation with acute, chronic, and repeated stress. Free Radic. Biol. Med. *55*, 109–118. https://doi.org/10.1016/j.freeradbiomed.2012.11.001.

57. Walter, L., Canup, B., Pujada, A., Bui, T.A., Arbasi, B., Laroui, H., Merlin, D., and Garg, P. (2020). Matrix metalloproteinase 9 (MMP9) limits reactive oxygen species (ROS) accumulation and DNA damage in colitis-associated cancer. Cell Death Dis. *11*, 767. https://doi.org/10.1038/s41419-020-02959-z.

58. Tumber, A., Nuzzi, A., Hookway, E.S., Hatch, S.B., Velupillai, S., Johansson, C., Kawamura, A., Savitsky, P., Yapp, C., Szykowska, A., et al. (2017). Potent and Selective KDM5 Inhibitor Stops Cellular Demethylation of H3K4me3 at Transcription Start Sites and Proliferation of MM1S Myeloma Cells. Cell Chem. Biol. *24*, 371–380. https://doi.org/10.1016/j.chembiol.2017.02.006.

59. Cornwell, M., Vangala, M., Taing, L., Herbert, Z., Köster, J., Li, B., Sun, H., Li, T., Zhang, J., Qiu, X., et al. (2018). VIPER: Visualization Pipeline for RNA-seq, a Snakemake workflow for efficient and complete RNA-seq analysis. BMC Bioinform. *19*, 135. https://doi.org/10.1186/s12859-018-2139-9.

60. Qiu, X., Feit, A.S., Feiglin, A., Xie, Y., Kesten, N., Taing, L., Perkins, J., Gu, S., Li, Y., Cejas, P., et al. (2021). CoBRA: Containerized Bioinformatics Workflow for Reproducible ChIP/ATAC-seq Analysis. Genom. Proteom. Bioinform. *19*, 652–661. https://doi.org/10.1016/j.gpb.2020.11.007.

61. Li, W., Xu, H., Xiao, T., Cong, L., Love, M.I., Zhang, F., Irizarry, R.A., Liu, J.S., Brown, M., and Liu, X.S. (2014). MAGeCK enables robust identification of essential genes from genome-scale CRISPR/Cas9 knockout screens. Genome Biol. *15*, 554. https://doi.org/10.1186/s13059-014-0554-4.

62. Wang, B., Wang, M., Zhang, W., Xiao, T., Chen, C.H., Wu, A., Wu, F., Traugh, N., Wang, X., Li, Z., et al. (2019). Integrative analysis of pooled CRISPR genetic screens using MAGeCKFlute. Nat. Protoc. *14*, 756–780. https://doi.org/10.1038/s41596-018-0113-7.

63. Wu, T., Hu, E., Xu, S., Chen, M., Guo, P., Dai, Z., Feng, T., Zhou, L., Tang, W., Zhan, L., et al. (2021). clusterProfiler 4.0: A universal enrichment tool for interpreting omics data. Innovation *2*, 100141. https://doi.org/10.1016/j.xinn.2021.100141.

64. Yu, G., Wang, L.G., Han, Y., and He, Q.Y. (2012). clusterProfiler: an R package for comparing biological themes among gene clusters. OMICS *16*, 284–287. https://doi.org/10.1089/omi.2011.0118.

65. Chen, E.Y., Tan, C.M., Kou, Y., Duan, Q., Wang, Z., Meirelles, G.V., Clark, N.R., and Ma'ayan, A. (2013). Enrichr: interactive and collaborative HTML5 gene list enrichment analysis tool. BMC Bioinf. *14*, 128. https://doi.org/10.1186/1471-2105-14-128.

66. Kuleshov, M.V., Jones, M.R., Rouillard, A.D., Fernandez, N.F., Duan, Q., Wang, Z., Koplev, S., Jenkins, S.L., Jagodnik, K.M., Lachmann, A., et al. (2016). Enrichr: a comprehensive gene set enrichment analysis web server 2016 update. Nucleic Acids Res. *44*, W90–W97. https://doi.org/10.1093/nar/gkw377.

67. Xie, Z., Bailey, A., Kuleshov, M.V., Clarke, D.J.B., Evangelista, J.E., Jenkins, S.L., Lachmann, A., Wojciechowicz, M.L., Kropiwnicki, E., Jagodnik, K.M., et al. (2021). Gene Set Knowledge Discovery with Enrichr. Curr. Protoc. *1*, e90. https://doi.org/10.1002/cpz1.90.

68. Liberzon, A., Birger, C., Thorvaldsdóttir, H., Ghandi, M., Mesirov, J.P., and Tamayo, P. (2015). The Molecular Signatures Database (MSigDB) hallmark gene set collection. Cell Syst. *1*, 417–425. https://doi.org/10.1016/j.cels.2015.12.004.

69. Subramanian, A., Tamayo, P., Mootha, V.K., Mukherjee, S., Ebert, B.L., Gillette, M.A., Paulovich, A., Pomeroy, S.L., Golub, T.R., Lander, E.S., and Mesirov, J.P. (2005). Gene set enrichment analysis: a knowledge-based approach for interpreting genome-wide expression profiles. Proc. Natl. Acad. Sci. USA *102*, 15545–15550. https://doi.org/10.1073/pnas.0506580102.

70. Sanjana, N.E., Shalem, O., and Zhang, F. (2014). Improved vectors and genome-wide libraries for CRISPR screening. Nat. Methods *11*, 783–784. https://doi.org/10.1038/nmeth.3047.

71. Creech, A.L., Taylor, J.E., Maier, V.K., Wu, X., Feeney, C.M., Udeshi, N.D., Peach, S.E., Boehm, J.S., Lee, J.T., Carr, S.A., and Jaffe, J.D. (2015). Building the Connectivity Map of epigenetics: chromatin profiling by quantitative targeted mass spectrometry. Methods *72*, 57–64. https://doi.org/10.1016/j.ymeth.2014.10.033.

72. Taing, L., Bai, G., Cousins, C., Cejas, P., Qiu, X., Herbert, Z.T., Brown, M., Meyer, C.A., Liu, X.S., Long, H.W., and Tang, M. (2021). CHIPS: A Snakemake pipeline for quality control and reproducible processing of chromatin profiling data. F1000Res. *10*, 517. https://doi.org/10.12688/f1000research.52878.1.

73. Li, H., and Durbin, R. (2009). Fast and accurate short read alignment with Burrows-Wheeler transform. Bioinformatics *25*, 1754–1760. https://doi.org/10.1093/bioinformatics/btp324.

74. Zhang, Y., Liu, T., Meyer, C.A., Eeckhoute, J., Johnson, D.S., Bernstein, B.E., Nusbaum, C., Myers, R.M., Brown, M., Li, W., and Liu, X.S. (2008). Model-based analysis of ChIP-Seq (MACS). Genome Biol. *9*, R137. https://doi.org/10.1186/gb-2008-9-9-r137.

75. Neph, S., Kuehn, M.S., Reynolds, A.P., Haugen, E., Thurman, R.E., Johnson, A.K., Rynes, E., Maurano, M.T., Vierstra, J., Thomas, S., et al. (2012). BEDOPS: high-performance genomic feature operations. Bioinformatics *28*, 1919–1920. https://doi.org/10.1093/bioinformatics/bts277.

76. Quon, G., Haider, S., Deshwar, A.G., Cui, A., Boutros, P.C., and Morris, Q. (2013). Computational purification of individual tumor gene expression profiles leads to significant improvements in prognostic prediction. Genome Med. *5*, 29. https://doi.org/10.1186/gm433.

77. Hanzelmann, S., Castelo, R., and Guinney, J. (2013). GSVA: gene set variation analysis for microarray and RNA-seq data. BMC Bioinform. *14*, 1. https://doi.org/10.1186/1471-2105-14-7.

78. Yoshihara, K., Shahmoradgoli, M., Martínez, E., Vegesna, R., Kim, H., Torres-Garcia, W., Treviño, V., Shen, H., Laird, P.W., Levine, D.A., et al. (2013). Inferring tumour purity and stromal and immune cell admixture from expression data. Nat. Commun. *4*, 2612. https://doi.org/10.1038/ncomms3612.

79. Xiao, T., Li, W., Wang, X., Xu, H., Yang, J., Wu, Q., Huang, Y., Geradts, J., Jiang, P., Fei, T., et al. (2018). Estrogen-regulated feedback loop limits the efficacy of estrogen receptor-targeted breast cancer therapy. Proc. Natl. Acad. Sci. USA *115*, 7869–7878. https://doi.org/10.1073/pnas.1722617115.

80. Li, W., Köster, J., Xu, H., Chen, C.H., Xiao, T., Liu, J.S., Brown, M., and Liu, X.S. (2015). Quality control, modeling, and visualization of CRISPR screens with MAGeCK-VISPR. Genome Biol. *16*, 281. https://doi.org/10.1186/s13059-015-0843-6.

81. Chen, C.H., Xiao, T., Xu, H., Jiang, P., Meyer, C.A., Li, W., Brown, M., and Liu, X.S. (2018). Improved design and analysis of CRISPR knockout screens. Bioinformatics *34*, 4095–4101. https://doi.org/10.1093/bioinformatics/bty450.

82. Shu, S., Wu, H.-J., Ge, J.Y., Zeid, R., Harris, I.S., Jovanović, B., Murphy, K., Wang, B., Qiu, X., Endress, J.E., et al. (2020). Synthetic Lethal and Resistance Interactions with BET Bromodomain Inhibitors in Triple-Negative Breast Cancer. Mol. Cell *78*, 1096–1113.e8. https://doi.org/10.1016/j.molcel.2020.04.027.

83. Ritchie, M.E., Phipson, B., Wu, D., Hu, Y., Law, C.W., Shi, W., and Smyth, G.K. (2015). limma powers differential expression analyses for RNA-sequencing and microarray studies. Nucleic Acids Res. *43*, e47. https://doi.org/10.1093/nar/gkv007.

84. Benjamini, Y., and Yosef, H. (1995). Controlling the False Discovery Rate: A Practical and Powerful Approach to Multiple Testing. J. Royal Statis. Soc. Series B (Methodol.) *57*, 289–300.

STAR★METHODS

KEY RESOURCES TABLE

REAGENT or RESOURCE	SOURCE	IDENTIFIER
Antibodies		
Rabbit monoclonal anti IL27-RA	Cell Signaling Technology	Cat# 41220
Rabbit monoclonal anti MMP-9	Cell Signaling Technology	Cat# 13667; RRID:AB_2798289
Rabbit polyclonal anti MIA	Peprotech	Cat# 500-P243; RRID:AB_1268631
Rabbit polyclonal anti p44/42 MAPK	Cell Signaling Technology	Cat# 9102; RRID:AB_330744
Rabbit monoclonal anti NRF1	abcam	Cat# ab175932; RRID:AB_2629496
Rabbit polyclonal anti CTCF	abcam	Cat# ab70303; RRID:AB_1209546
Rabbit Gamma Globulin	Life Technologies	Cat# 31887; RRID:AB_2532980
Mouse IgG Isotype Control	Life Technologies	Cat# 10400C; RRID:AB_2532980
Armenian Hamster IgG Isotype Control (eBio299Arm), eBioscience	Life Technologies	Cat# 14-4888-81; RRID:AB_470128
Goat anti-Rabbit IgG (H+L) Secondary Antibody, HRP	Life Technologies	Cat# 65-6120; RRID:AB_2533967
Goat anti-Mouse IgG (H+L) Secondary Antibody, HRP	Life Technologies	Cat# 62-6520; RRID:AB_2533947
Goat anti-Armenian Hamster IgG (H+L) Secondary Antibody, HRP	Life Technologies	Cat# PA1-32045; RRID:AB_10985178
Mouse monoclonal anti-beta-Actin (AC-74)	Sigma	Cat# A2228; RRID:AB_476697
Monoclonal Anti-α-Tubulin antibody produced in mouse	Sigma	Cat# T5168; RRID:AB_477579
Armenian Hamster monoclonal anti-ZBTB7A (13E9)	Life Technologies	Cat# 14-3309-82; RRID:AB_2043856
Armenian Hamster monoclonal anti-ZBTB7A (13E9)	SantaCruz	Cat# sc-33683; RRID:AB_668999
Rabbit monoclonal anti-ZBTB7A (EPR13178(B))	Abcam	Cat# ab175918
Recombinant monoclonal anti-KDM5A	Active Motif	Cat# 91211; RRID:AB_2793805
Anti-KDM5A / Jarid1A / RBBP2 antibody (ab70892)	abcam	ab70892; RRID:AB_2280628
Rabbit polyclonal anti-KDM5B	Sigma	Cat# HPA027179; RRID:AB_1851987
Rabbit monoclonal anti-KDM5B (E2X6N)	Cell Signaling Technology	Cat# 15327; RRID:AB_2798737
Rabbit polyclonal anti-KDM5B	Novus Biologicals	Cat# 22260002; RRID:AB_10004656
Rabbit polyclonal anti-KDM5C	Abcam	Cat# ab34718; RRID:AB_881090
Rabbit polyclonal anti-H3K4me3	Diagenode	Cat# C15410003-50
Anti-Histone H3 (tri methyl K4) antibody - ChIP Grade (ab8580)	Abcam	Cat# ab8580; RRID:AB_306649
Mouse monoclonal anti-H3	Active Motif	Cat# 39763; RRID:AB_265052
RhoA (67B9) Rabbit mAb #2117	Cell Signaling Technology	Cat# 2117: RRID:AB_10693922
Anti-PKN2 antibody (ab87812)	Abcam	Cat# ab87812; RRID:AB_2042690
Rabbit monoclonal anti-MTA1 (D17G10)	Cell Signaling Technology	Cat# 5647; RRID:AB_10705601
Rabbit polyclonal anti-MTA2	Cell Signaling Technology	Cat# 15793
Rabbit monoclonal anti-MBD2 (EPR18361)	Abcam	Cat# ab188474
Rabbit monoclonal anti-MBD3 (N87)	Cell Signaling Technology	Cat# 14540; RRID:AB_2798504
Rabbit polyclonal anti-CHD3	Cell Signaling Technology	Cat# 4241; RRID:AB_10557102
Rabbit monoclonal anti-CHD4 (D8B12)	Cell Signaling Technology	Cat# 11912; RRID:AB_2751014
Phospho-NF-κB p65 (Ser536) (93H1) Rabbit mAb #3033	Cell Signaling Technology	Cat# 3033; RRID:AB_331284

(*Continued on next page*)

Continued

REAGENT or RESOURCE	SOURCE	IDENTIFIER
Recombinant Anti-NF-kB p65 antibody [E379] (ab32536)	Abcam	Cat# ab32536; RRID:AB_776751
Phospho-NFkB p50 (Ser337) Polyclonal Antibody	Life Technologies	Cat# PA5-37658; RRID:AB_2554266
NFkB p50 Monoclonal Antibody (5D10D11)	Life Technologies	C# MA5-15870; RRID:AB_11153885
Bacterial and virus strains		
Endura ElectroCompetent Cells	Lucigen	Cat# 60242-2
One Shot Stbl3 Chemically Competent E. coli	Life Technologies	Cat# C737303
Chemicals, peptides, and recombinant proteins		
KDM5 inhibitor C70	This paper; Johansson et al.[16]; Tumber et al.[58]; Hinohara et al.[10]	N/A
Nonyl Acridine Orange (Acridine Orange 10-Nonyl Bromide)	Life Technologies	Cat# A1372
Recombinant Human TNF-alpha Protein	R&D Systems	Cat# 210-TA
Critical commercial assays		
Thermo Scientific	Active Rho Pull-Down and Detection Kit	Cat# 16116
Thermo Scientific	Active Rac1 Pull-Down and Detection Kit	Cat# 16118
Seahorse XF Cell Mito Stress Test Kit	Agilent	Cat# 103015-100
Seahorse FluxPaks	Agilent	Cat# 102340-100
Seahorse XF DMEM assay medium pack, pH 7.4	Agilent	Cat# 103680-100
Total Reactive Oxygen Species (ROS) Assay Kit 520 nm	Invitrogen	Cat# 88-5930
Deposited data		
All raw genomic data	GEO	GSE259252
Processed CRISPR screen data	This paper	Table S2
Processed mass spectrometry data (qPLEX-RIME)	This paper	Table S3
Raw histone mass spectrometry data	MassIVE	MSV000094452
Experimental models: Cell lines		
SUM149 cell line	Steve Ethier (University of Michigan)	N/A
SUM149 cell line, ROSA26-g1	This paper	N/A
SUM149 cell line, ROSA26-g2	This paper	N/A
SUM149 cell line, ZBTB7A-g1	This paper	N/A
SUM149 cell line, ZBTB7A-g2	This paper	N/A
SUM149 cell line, KDM5A-g1	This paper	N/A
SUM149 cell line, KDM5A-g2	This paper	N/A
SUM149 cell line, KDM5B-g1	This paper	N/A
SUM149 cell line, KDM5B-g2	This paper	N/A
SUM149 cell line, RHOA-g1	This paper	N/A
SUM149 cell line,RHOA-g2	This paper	N/A
SUM149 cell line,PKN2-g1	This paper	N/A
SUM149 cell line, PKN2-g2	This paper	N/A
MDA-MB-436 cell line	ATCC	HTB-130; RRID:CVCL_0623
MDA-MB-436 cell line, ROSA26-g1	This paper	N/A
MDA-MB-436 cell line, ZBTB7A-g2	This paper	N/A
MCF7 cell line	Marc Lippman (University of Michigan)	N/A

(*Continued on next page*)

Continued

REAGENT or RESOURCE	SOURCE	IDENTIFIER
MCF7 cell line, ROSA26-g1	This paper	N/A
MCF7 cell line, ZBTB7A-g1	This paper	N/A
SUM159 cell line	Steve Ethier (University of Michigan)	
FCIBC02 cell line	Massimo Christofanelli (Fox Chase Cancer Center)	
T-47D cell line	ATCC	HTB-133; RRID:CVCL_0553
BT-474 cell line	ATCC	HTB-20
MDA-MB-361 cell line	ATCC	HTB-27; RRID:CVCL_0620
HCC1419 cell line	ATCC	CRL-2326; RRID:CVCL_1251
SKBR3 cell line	ATCC	HTB-30; RRID:CVCL_0033
Oligonucleotides		
ROSA26-g1: GGTGATCTAGTATTTCTTG	This paper	N/A
ROSA26-g2: TGCGGTCAGGTCACGCCGC	This paper	N/A
NonTargeting-g1: ACCGGAACGATCTCGCGTA	This paper	N/A
ZBTB7A-g1: CCGTCAGCACAGCCAACGT	This paper	N/A
ZBTB7A-g2: TTGAAGTACTGGCTGCAGG	This paper	N/A
KDM5A-g1: TCCAGAATGCTTAGATGTG	This paper	N/A
KDM5A-g2: TGTCCTAAATGTGTCGCCG	This paper	N/A
KDM5B-g1: CACCTTCGCCTAGTCACAC	This paper	N/A
KDM5B-g2: GACTGGCATCTGTAAGGTG	This paper	N/A
RHOA-g1: AAACACATCAGTATAACAT	This paper	N/A
RHOA-g2: CCACTCACCTAAACTATCA	This paper	N/A
PKN2-g1: TAATGGAATATGCTGCCGG	This paper	N/A
PKN2-g2: TAGATATCATACTTTGACG	This paper	N/A
CRISPR PCR round 1 Forward: AATGGACTATCATATGCTTACCGTAA CTTGAAAGTATTTCG	This paper	N/A
CRISPR PCR round 1 Reverse: TCTAC TATTCTTTCCCCTGCACTGTGACTGT GGGCGATGTGCGCTCTG	This paper	N/A
CRISPR PCR round 2 Staggered 1 Forward: AATGATACGGCGACCACCGAGATCTACACT CTTTCCCTACACGACGCTCTTCCGATCTt CAAGGTCAtcttgtggaaaggacgaaacaccg	This paper	N/A
CRISPR PCR round 2 Staggered 1 Reverse: CAAGCAGAAGACGGCATACGAGATCAAGG TCAGTGACTGGAGTTCAGACGTGTGCT CTTCCGATCTacgatcgatTCTACTATTCT TTCCCCTGCACTGT	This paper	N/A
CRISPR PCR round 2 Staggered 2 Forward: AATGATACGGCGACCACCGAGATCTACACT CTTTCCCTACACGACGCTCTTCCGATCTat GCATAACTtcttgtggaaaggacgaaacaccg	This paper	N/A
CRISPR PCR round 2 Staggered 2 Reverse: CAAGCAGAAGACGGCATACGAGATGCATAA CTGTGACTGGAGTTCAGACGTGTGCTCTTCC GATCTcgatcgatTCTACTATTCTTTCC CCTGCACTGT	This paper	N/A

(*Continued on next page*)

Continued

REAGENT or RESOURCE	SOURCE	IDENTIFIER
CRISPR PCR round 2 Staggered 3 Forward: AATGATACGGCGACCACCGAGATCTACAC TCTTTCCCTACACGACGCTCTTCCGATCT gatCTCTGATTtcttgtggaaaggacgaaacaccg	This paper	N/A
CRISPR PCR round 2 Staggered 3 Reverse: CAAGCAGAAGACGGCATACGAGATCTCTG ATTGTGACTGGAGTTCAGACGTGTGCTCTT CCGATCTgatcgatTCTACTATTCTTTC CCCTGCACTGT	This paper	N/A
CRISPR PCR round 3 Forward: AATGATACGGCGACCACCGA	This paper	N/A
CRISPR PCR round 3 Reverse: CAAGCAGAAGACGGCATACGA	This paper	N/A
Recombinant DNA		
Human CRISPR Knockout Library (H3)	Addgene	Cat# 133914
lentiCRISPR v2	Addgene	Cat# #52961
pLV-5xNFkBminiP-d1EGFP	This paper	Vector builder
Software and algorithms		
Visualization Pipeline for RNA-seq analysis (VIPER)	Bitbucket; Cornwell et al. (2018)[59]	https://bitbucket.org/cfce/viper/src/master/
Containerized Bioinformatics workflow for Reproducible ChIP/ATAC-seq Analysis (CoBRA)	Bitbucket; Qiu et al. [60]	https://bitbucket.org/cfce/cobra/src/master/
Model-based Analysis of Genome-wide CRISPR-Cas9 Knockout (MAGeCK) (version: 0.5.9)	SourceForge; Li et al. [61]	https://sourceforge.net/p/mageck/wiki/Home/
MAGeCKFlute (version 1.14.0)	Bioconductor; Wang et al.[62]	https://www.bioconductor.org/packages/release/bioc/html/MAGeCKFlute.html
Cell Ranger (version: 5.0.1)	10X Genomics	https://www.10xgenomics.com/support/software/cell-ranger/latest
Seurat (version 4.3.0)	CRAN	https://cran.r-project.org/web/packages/Seurat/index.html
ERVmap (version 1.1)	Github; Tokuyama et al. (2018)[41]	https://github.com/mtokuyama/ERVmap
ClusterProfiler (version: 4.2.2)	Bioconductor; Wu et al.; Yu et al.[63,64]	https://bioconductor.org/packages/release/bioc/html/clusterProfiler.html
Enrichr	Ma'ayan Lab (Icahn School of Medicine, Mount Sinai)[65–67]	https://maayanlab.cloud/Enrichr/
Molecular Signatures Database (MSigDB) Compute Overlaps Function	Broad Institute, Inc., Massachusetts Institute of Technology, and Regents of the University of California[68,69]	https://www.gsea-msigdb.org/gsea/msigdb/index.jsp
RStudio (version: 4.2.0)	Posit	https://posit.co
Affinity Designer (version: 1.10.4)	Affinity	https://affinity.serif.com/en-us/
GraphPadPrism (version: 9)	GraphPad Software Inc.	https://www.graphpad.com/updates/prism-900-release-notes
FlowJo (version: 10.8.2)	FlowJo, LLC	https://www.flowjo.com/

EXPERIMENTAL MODEL AND STUDY PARTICIPANT DETAILS

Breast cancer cohort data

TCGA data was downloaded from cBioPortal (https://www.cbioportal.org/) for the Breast Invasive Carcinoma (TCGA, PanCancer Atlas) dataset (ID = brca_tcga_pan_can_atlas_2018).

Breast cancer cell lines and derivation of the C70-resistant model

Breast cancer cell lines were obtained from ATCC, or generously provided by Dr. Steve Ethier (U. Michigan) and cultured following the provider's recommendations. The identity of the cell lines was confirmed based on STR and exome-seq analyses. Cells were

regularly tested for mycoplasma. SUM149 and SUM159 were cultured in DMEM/F12 supplemented with 5% FBS, 5 μg/mL insulin, and 1 μg/mL hydrocortisone. MCF7 was cultured in DMEM/F12 supplemented with 10% FBS, and 10 μg/mL insulin. FCIBC02 was cultured in DMEM/F12 supplemented with 10% FBS. MDA-MB-436 was cultured in McCoy's supplemented with 10% FBS, and 10 μg/mL insulin. SKBR3 was cultured in McCoy's supplemented with 10% FBS. MDA-MB-361 was cultured in McCoy's supplemented with 20% FBS. T-47D was cultured in RPMI supplemented with 10% FBS and 10 μg/mL insulin. BT-474 and HCC1419 were cultured in RPMI supplemented with 10% FBS. All cell lines were supplemented with 100 U/mL penicillin and 100 μg/mL streptomycin. All cells were cultured at 37°C with 5% CO_2. C70 resistant SUM149CR cells were derived by growing the cells in the presence of 10 μM C70 and retested IC50 in every 5th passage. It took ~45 days to achieve resistance determined based on a significant shift in IC50. Subsequently the cells were maintained in 10 μM C70-containing culture media.

CRISPR libraries

Human CRISPR knockout library (H3) was generated by Drs. Xiaole Shirley Liu and Myles Brown (Addgene #133914).

METHOD DETAILS

Cellular viability and growth assays

Viability and growth assays were performed in 96-well plates (N = 6 well per condition). Cells were treated with inhibitors and cultured at 37 °C with 5% CO_2. The medium was replaced with fresh medium (with or without inhibitors) every 2-3 days. Plates were fixed in an ice-cold 3:1 mixture of methanol and glacial acetic acid for at least 10 minutes. Fixed cells were washed twice with 1X PBS and stained with 1 μg/mL DAPI at 37 °C for 20 minutes. The cells were washed twice with 1X PBS and the number of DAPI stained cells were acquired using the automated Celigo Image Cytometer from Nexcelom.

CRISPR screen and data analyses

Human CRISPR knockout library (H3) was generated by Drs. Xiaole Shirley Liu and Myles Brown (Addgene #133914). We followed the screen protocol for adherent cells provided by Addgene (Addgene #133914). Briefly, 200 million SUM149 or SUM149CR cells were infected with the pooled lentiviral CRISPR knock-out H3 library at a multiplicity of infection of 0.3 to ensure most cells received only one viral construct. This resulted in ~60 million infected cells and 500X library coverage. After 5 days of puromycin selection, more than 60 million cells were pelleted and stored as the day 0 control. The remaining cells were split and cultured for 10 doublings with 0.01% DMSO or 10 μM C70. To limit changes in gRNA distribution due to sampling, 60 million cells per condition (500X library coverage) were seeded each passage or pelleted at the treatment endpoint. Genomic DNA was isolated from the pelleted samples via phenol/chloroform extraction and PCR was performed to construct each sequencing library (see key resources table for primer information). The libraries were sequenced at 30-40 million reads per sample to ensure at least 300X library coverage. The libraries were sequenced on an Illumina NS500 Single End 75bp with a 10% PhiX spike in.

Generation of single CRISPR/Cas9 knock-out cells

Construction of lenti-CRISPR/Cas9 vectors targeting ZBTB7A, KDM5A, KDM5B, RHOA, and PKN2 was performed following the protocol associated with the backbone vector lentiCRISPR V2 (Addgene #52961)[70] The sgRNA sequences used are listed in key resources table. Knockouts were verified by western blot analysis after puromycin selection.

Generation of NFkB reporter cells

A lentiviral vector containing the NF-kB reporter (pLV-5xNFkBminiP-d1EGFP) was designed based on the backbone of the HypoxCR vector (Addgene #59946) and obtained via fee service from VectorBuilder (https://en.vectorbuilder.com/). The vector contained DNA sequences encoding d1EGFP and mCherry downstream of the 5xNF-kB response element-minimal promoter and CMV promoter, respectively. Cells were transduced with the vector and selected for with Blasticidin.

ChIP-seq

SUM149 expressing *ROSA26-g1* -/+ 10 μM C70 for 7 days, *ZBTB7A-g1 (ZBTB7A-KO)*, *KDM5A-g1 (KDM5A-KO)*, and *KDM5B-g1(KDM5B-KO)* from the lentiCRISPR v2 backbone (see key resources table) were cultured in biological duplicates in 15 cm dishes to about 80% confluence. For ChIP-seq of histone modifications (H3K4me3), each dish was washed once with PBS then crosslinked in fixing buffer (50 mM HEPES-NaOH pH 7.5, 100 mM NaCl, 1 mM EDTA) containing 1% PFA (Electron Microscopy Sciences, 15714) for 10 minutes at room temperature. For ChIP-seq of chromatin binding proteins (KDM5A, KDM5B, ZBTB7A), each dish was washed once with PBS then crosslinked in PBS containing 2 mM DSG (Fisher Scientific 20593) for 30 minutes at room temperature. DSG was then removed, and the samples were further crosslinked with fixing buffer (50 mM HEPES-NaOH pH 7.5, 100 mM NaCl, 1 mM EDTA) containing 1% PFA for 10 minutes at 37 °C. After PFA fixation, all samples were quenched with glycine at a final concentration of 0.125 M for 5 minutes at room temperature. Cells were washed and harvested in ice cold PBS. Nuclei were extracted by first resuspending the cells in lysis buffer (1 mL per 5 million cells) for 10 minutes at 4C (50 mM HEPES-NaOH pH 8, 140 mM NaCl, 1 mM EDTA, 10% Glycerol, 0.5% IGEPAL CA-630, 0.25% Triton X-100). Nuclei were pelleted and washed once in wash buffer (10 mM Tris-HCl pH 8, 200 mM NaCl, 1 mM EDTA), 1 mL of wash buffer per 10 million cells (histone modification ChIP) or 25 million cells (chromatin

modification ChIP). The nuclei were then pelleted and resuspended in 1 mL of shearing buffer (10 mM Tris-HCl pH 8, 1 mM EDTA, 0.1% SDS), containing 10 million (histone modification ChIP) or 25 million cells (chromatin modification ChIP). Samples were transferred to 1 mL AFA Fiber tubes (Covaris 520130), and sonicated in a Covaris E220 sonicator with the following settings: Peak Incident Power 150, Duty Cycles 5%, cycles per Burst 200. Histone modification ChIP samples were sonicated for 900 seconds. Chromatin binding protein ChIP samples were sonicated for 1,200 seconds. After sonication, Triton X-100 and NaCl were added to a final concentration of 1% Triton X-100 and 150 mM NaCl. The samples were then pre-cleared with 50 μL of Dynabeads Protein G (Fisher Scientific, 10004D) for 1 hour at 4 °C. For histone modification ChIP, primary antibodies were added to 1 mL of pre-cleared chromatin from ~10 million cells (H3K4me3 = Diagenode C154100003 at 5 μg/mL) and incubated at 4 °C overnight. For chromatin binding protein ChIP, pre-cleared samples were aliquoted, and volumes adjusted using shearing buffer containing 1% Triton X-100 and 150 mM NaCl before adding the appropriate primary antibodies for overnight incubation at 4°C. Chromatin binding protein ChIP samples contained 500 μL of pre-cleared chromatin from ~5 million cells (ZBTB7A = SantaCruz sc-33683X at 5 μg/mL, KDM5A = Abcam ab70892 at 4 μg/mL, KDM5B = Novus/sdix 22260002 at 5 μg/mL). After overnight immunoprecipitation, crosslinked complexes were precipitated with Dynabeads G (Fisher Scientific, 10004D) for 2 hours at 4°C. The beads were then washed once with low salt wash buffer (20 mM Tris-HCl pH 8, 150 mM NaCl, 0.1% SDS, 1% Triton-X 100, 2 mM EDTA) for 5 minutes at 4°C, once with high salt wash buffer (20 mM Tris-HCl pH 8, 500 mM Nacl, 0.1% SDS, 1% Triton-X 100, 2 mM EDTA) for 5 minutes at 4 °C, once with wash buffer (10 mM Tris-HCl pH 8, 250 mM LiCl, 1% IGEPAL CA-630, 1% Sodium Deoxycholate, 1 mM EDTA) for 5 minutes at 4 °C, and once with TE buffer (10 mM Tris-HCl pH8, 1 mM EDTA) quickly at room temperature. DNA was eluted from the beads in 1% SDS, 100 mM $NaHCO_3$ for 30 minutes at room temperature. Crosslinks were reversed at 65°C overnight. RNA and protein were digested with 0.2 mg/mL RNase A for 30 minutes at 37°C followed by 0.2 mg/mL Proteinase K for 1 hour at 55 °C. DNA was purified with phenol chloroform extraction and ethanol precipitation. Libraries were prepared and sequenced at the Molecular Biology Core Facilities (MBCF) at the Dana-Farber Cancer Institute (DFCI). Libraries were prepared with the automated Swift 2S ligation chemistry and sequenced to 40M 50 bp reads pairs.

RNA-seq

SUM149 and SUM149CR were incubated in biological triplicates for 2 and 7 days in 0.01% DMSO or 10 μM. SUM149 KOs (*ROSA26-g1*, *KDM5A-g1*, *KDM5B-g1*, and *ZBTB7A-g1*), MCF7 KOs (*ROSA26-g1* and *ZBTB7A-g1*), and MDA-MB-436 KOs (*ROSA26-g1* and *ZBTB7A-g2*) were incubated in biological duplicates for 7 days in 0.01% DMSO or 10 μM C70. Cells were cultured to ~80% confluence in 10 cm dishes and RNA was collected using the RNeasy Mini Kit (Qiagen 74104 or 74106) and submitted to the Molecular Biology Core Facilities (MBCF) at the Dana-Farber Cancer Institute for library prep and sequencing. RNA underwent polyA enrichment before library prep and was sequenced on an Illumina NovaSeq to generate 40M 150bp read pairs (80M reads total) per sample.

qPLEX-RIME

SUM149, SUM159, MCF7, and T-47D were cultured to ~80% confluence in 4-5 biological replicates in 15 cm dishes. Samples were washed once with PBS then crosslinked in PBS containing 2 mM DSG (Fisher Scientific 20593) for 30 minutes at room temperature. DSG was then removed, and the samples were further crosslinked with fixing buffer (50 mM HEPES-NaOH pH 7.5, 100 mM NaCl, 1 mM EDTA) containing 1% PFA for 10 minutes at 37°C. After PFA fixation, all samples were quenched with glycine at a final concentration of 0.125 M for 5 minutes at room temperature. Cells were washed and harvested in ice cold PBS, pelleted, and snap frozen.

The nuclear fraction was extracted by first resuspending the pellet in 10ml of LB1 buffer (50 mM Hepes–KOH, pH 7.5; 140 mM NaCl; 1 mM EDTA;10% Glycerol; 0.5% NP-40 or Igepal CA-630; 0.25% Triton X-100) for 10 min at 4oC. Cells were pelleted, resuspended in 10 ml of LB2 buffer (10 mM Tris–HCL, pH8.0; 200 mM NaCl; 1 mM EDTA; 0.5 mM EGTA) and mixed at 4oC for 5 minutes. Cells were pelleted and resuspended in 300 ul of LB3 buffer (10 mM Tris–HCl, pH 8; 100 mM NaCl; 1 mM EDTA; 0.5 mM EGTA; 0.1% Na–Deoxycholate; 0.5% N-lauroylsarcosine) and sonicated in a waterbath sonicator (Diagenode bioruptor). 30μl of 10% Triton-X was added and the lysate centrifuged for 10 minutes at 20,000 rcf to separate debris. Samples were incubated with primary antibody at 4 °C overnight [anti-KDM5B (Novus Biologics 22260002)]. Samples were then precipitated with Dynabeads Protein G for 2 hr. The beads were washed 10 times in 1ml of RIPA buffer and twice in 100mM ammonium hydrogen carbonate (AMBIC) solution. For the second AMBIC wash, the beads were transferred to new tubes.

Samples were digested and purified with the Ultra-Micro C18 Spin Columns (Harvard Apparatus) as previously described[31] After purification, each sample was dried and reconstituted in 100ul 0.1M TEAB (triethylammonium bicarbonate) and labelled with the TMT-10plex reagents (Thermo Fisher). The peptide mixture was fractionated with Reversed-Phase spin columns at high pH (Pierce, #84868) and each fraction was analyzed on a Dionex Ultimate 3000 UHPLC system coupled with the LTQ Orbitrap Velos mass spectrometer (Thermo Scientific). Mobile phase A was composed of 2% acetonitrile, 0.1% formic acid, 5% dimethyl sulfoxide (DMSO) and mobile phase B was composed of 80% acetonitrile, 0.1% formic acid, 5% DMSO. The precursor scans were performed in the Orbitrap in the range of 380-1500 m/z at 60K resolution. The MS2 scans were performed in the ion trap with CID collision energy 30% and in the Orbitrap with HCD collision energy 40% back-to-back for each precursor. The raw data were processed on Proteome Discoverer 2.1 using the SequestHT search engine. The node for SequestHT included the following settings: Precursor Mass Tolerance 20ppm, Fragment Mass Tolerance 0.5Da for the CID spectra and 0.05Da for the HCD spectra, Dynamic Modifications were Oxidation of M (+15.995Da), Deamidation of N/Q (+0.984Da) and Static Modifications were TMT6plex at any N-Terminus/K (+229.163Da).

Antibodies and inhibitors

Full list with catalog numbers available in key resources table. Antibodies used for Immunoblotting were anti-beta-Actin (Sigma, A2228), anti-alpha Tubulin (Sigma, T5168), anti-ZBTB7A (Invitrogen, 14-3309-82), anti-KDM5A (Abcam, ab70892), anti-KDM5B (Sigma, HPA027179), anti-KDM5C (Abcam, ab34718), anti-H3K4me3 (Abcam, ab8580), anti-H3 (Active Motif, 39763), anti-RHOA (Cell Signaling Technology, 2117), anti-PKN2 (Abcam, ab87812), anti-MTA1 (Cell Signaling Technology, 5647), anti-MTA2 (Cell Signaling Technology, 15793), anti-MBD2 (Abcam, ab188474), anti-MBD3 (Cell Signaling Technology, 14540), anti-CHD3 (Cell Signaling Technology, 4241), anti-CHD4 (Cell Signaling Technology, 11912), anti-phospho-p65 (Ser536) (Cell Signaling Technology, 3033), anti-p65 (Abcam, ab32536), anti-phospho-p50 (Ser337) (Invitrogen, PA5-37658), anti-p50 (Invitrogen, MA5-15870), Goat anti-Mouse IgG Secondary HRP (Invitrogen, 62-6520), Goat anti-Rabbit IgG Secondary HRP (Invitrogen, 65-6120), and Goat anti-Armenian Hamster IgG Secondary HRP (Invitrogen, PA1-32045). Antibodies used for Immunoprecipitation during Co-IP were anti-ZBTB7A (SantaCruz, sc-33683X), anti-ZBTB7A C-terminus (Abcam, ab175918), anti-KDM5A (Active Motif, 91211), and anti-KDM5B (Cell Signaling Technology, 15327). Additionally, isotype controls used were Rabbit IgG (Invitrogen, 31887), Mouse IgG (Invitrogen, 10400C), and Armenian Hamster IgG (Invitrogen, 14-4888-81). Antibodies used for Immunoprecipitation during ChIP-seq were anti-ZBTB7A (SantaCruz, sc-33683X), anti-KDM5A (Abcam, ab70892), anti-KDM5B (Novus Biologicals, 22260002), and anti-H3K4me3 (Diagenode, C15410003-50). Antibodies used for qPLEX-RIME were anti-KDM5B (Novus Biologicals, 22260002). The KDM5-C70 inhibitor was provided by the National Center for Advancing Translational Sciences (NCATS) (NCGC ID = NCGC00371443). Previous reports on the synthesis of KDM5-C70 are described in Tumber et al. (2017)[58] and Hinohara et al. (2018)[10].

Immunoblotting and immunoprecipitation experiments

For whole-cell lysates, cells were lysed in RIPA buffer (50 mM Tris-HCl pH 7.4, 150 mM NaCl, 1% NP-40, 0.5% sodium deoxycholate, 0.1% SDS, and 5 mM EDTA). To determine the levels of GTP-bound RhoA and Rac1, we used the Active Rho Pull-Down and Active Rac1 Pull-Down and detection kits from Thermo Scientific (Thermo Scientific, 16116 and 16118). SUM149 cells were treated with 0.01% DMSO or 10 μM C70 for 3 days before processing with the pull-down kits. The samples were collected at two different confluence levels to assess the effect of confluence on active GTPase levels: 50% and 100% confluence. For the Active Rho Pull-Down kit, an anti-RhoA specific antibody from Cell Signaling Technology (Cell Signaling Technology, 2117) was used for immunoblotting instead of the pan-RhO (RhoA, RhoB, RhoC) antibody provided in the kit. For cell fractionation experiments, cells were first incubated in hypotonic buffer (10 mM HEPES pH 7.4, 10 mM KCl, 1.5 mM $MgCl_2$, 0.5% NP-40, and 0.2 mM EDTA) for 10 minutes at 4°C. The samples were then centrifuged at 1,800xg for 5 minutes and the supernatant stored as the cytoplasmic fraction. The pelleted nuclei were resuspended in nuclear extraction buffer (20 mM HEPES pH 7.4, 420 mM NaCl, 1.5 mM $MgCl_2$, 0.5% NP-40, 0.2 mM EDTA), incubated for 10 minutes at 4°C, and sonicated in a cup horn sonicator (Qsonica Q500, 5 minutes net sonication time, 75% amplitude, 20 seconds On/10 seconds Off cycle). The lysate was then centrifuged at 13,000 rpm for 10 minutes and the supernatant stored as the nuclear fraction. For NRF1, cellular fractionation was performed with the Cell Fractionation Kit (CST, #9038) according to the manufacturers protocol. Briefly, different fractions were isolated from cell suspensions via specific isolation buffer and separately collected after centrifugation. For experiments only cytoplasmic fraction and cytoskeletal/nuclear fraction was used. For co-immunoprecipitation experiments, cells were incubated in hypotonic buffer (1 mL per 10 million cells) (10 mM HEPES pH 7.4, 10 mM KCl, 1.5 mM $MgCl_2$, 0.5% NP-40) for 10 minutes at 4°C, then centrifuged at 1,800xg for 5 minutes and supernatant discarded. The nuclear pellet was then resuspended in nuclear extraction buffer (300 μl per 10 million cells) (20 mM HEPES pH 7.4, 300 mM NaCl, 1.5 mM $MgCl_2$, 0.5% NP-40, 0.2 mM EDTA), incubated for 10 minutes at 4 °C and sonicated in a cup horn sonicator (Qsonica Q500, 5 minutes net sonication time, 75% amplitude, 20 seconds On/10 seconds Off cycle). The nuclear lysate was then cleared via centrifugation at 13,000 rpm for 10 minutes. Part of the nuclear lysate was stored as input, and to the rest 1 volume of CoIP dilution buffer was added (20 mM Tris-HCl pH 8.0, 4.5 mM $MgCl_2$, 1.0 mM $CaCl_2$, 0.5% NP-40, 0.2 mM EDTA). Then 1 mg of diluted nuclear lysate was moved to a 1.5 ml tube (Eppendorf LoBind Microcentrifuge Tubes: Protein, Cat# 13-698-794) and volume adjusted to 1 ml. The sample was pre-cleared with 25 μl of Protein A/G Magnetic Beads blocked with 0.5% BSA (Thermo Scientific, 8803) for 1 hour at 4°C. Pre-cleared samples were then incubated with primary antibodies or IgG controls (4 μg/ml) overnight at 4°C. After overnight incubation, protein complexes were precipitated with 25 μl of Protein A/G beads blocked with 0.5% BSA for 2 hours at 4°C. The protein-bead complexes were washed twice with 1 mL of wash buffer (20 mM Tris-HCl pH 8.0, 150 mM NaCl, 1.5 mM $MgCl_2$, 0.5% NP-40, 0.2 mM EDTA) and once with LoTE (10 mM Tris-HCl pH 8.0, 0.1 mM EDTA). Protein complexes were then eluted with 100 μL of sample buffer containing 1X NuPAGE sample reducing agent (Invitrogen NP0009) and 1X NuPAGE LDS Sample Buffer (Invitrogen NP0007) in nuclear extraction buffer for 10 minutes at room temperature. 20 μL of the eluted sample was used for western blotting. For all immunoblots, proteins were denatured with heating at 95°C for 10 minutes in 1X NuPAGE sample reducing agent (Invitrogen NP0009) and 1X NuPAGE LDS Sample Buffer (Invitrogen NP0007). The proteins were then resolved on a 4-12% Bis-Tris polyacrylamide gel (Invitrogen WG1402BOX) in MOPS SDS running buffer and transferred to PVDF membranes using a wet NuPAGE transfer buffer system. The membranes were blocked with 2.5% milk powder in 0.1% Tween20 in TBS (TBS-T) for 1 hour at room temperature followed by incubation with primary antibodies in 2.5% milk TBS-T overnight. The membranes were washed and incubated for 1 hour at room temperature with the appropriate secondary antibodies, then washed and developed with Clarity Western ECL substrate (Bio-Rad 1705061) or Clarity Max Western ECL substrate (Bio-Rad 1705062).

Mass spectrometry analysis of histone modifications

Cells were treated for 48 hours with 0.01% DMSO or 10 μM C70 for 48 hours. They were then collected via scraping in PBS, pelleted, and snap-frozen in liquid nitrogen. Histones were isolated from cell nuclei using acid extraction, biochemically prepared, and analyzed by mass spectrometry against a reference of stable isotope-labeled synthetic peptide standards exactly as described (Creech et al., 2015).[71]

scRNA-seq library prep

SUM149 and SUM149CR were seeded in 10 cm dishes and treated with 0.01% DMSO or 10 μM C70 for 7 days. The cells were then trypsinized and counted. One million cells were pelleted, washed 1 time, and resuspended in 1 mL of ice cold 0.04% BSA in PBS. Library construction was performed using the 10X Genomics 3' v3.1 library kit as described and sequenced on an Illumina NovaSeq.

Flow cytometry experiments

SUM149 cells expressing *ROSA26-g1* or *ZBTB7A-g1* from the lentiCRISPR v2 vector (see key resources table) were grown in 0.01% DMSO or 10 μM C70 for 5 days. Cells were passaged once during treatment and seeded to be 50% confluent by the 5-day endpoint. For detecting reactive oxygen species, 7 hours of 1 mM H_2O_2 treatment was used as a positive control. Cells were trypsinized, counted, and resuspended in 100 μL per million cells with 1X ROS assay reagent in assay buffer from the Total Reactive Oxygen Species (ROS) Assay Kit 520 nm (Thermo Fisher, 88-5930). The samples were then incubated for 1 hour at 37 °C, centrifuged at 200xg for 5 minutes, and resuspended in 500 μL of ice cold FACS buffer (1% BSA and 2 mM EDTA in PBS). For detecting mitochondrial cardiolipins, 2 hours of 1 mM H_2O_2 treatment was used as a positive control. Cells were trypsinized, counted, and resuspended in 1 mL per million cells with 0.4 μM Nonyl Acridine Orange (NAO) (Fisher Scientific, A1372) in PBS. The samples were then incubated for 20 minutes at 37 °C, centrifuged at 200xg for 5 minutes, and resuspended in 500 μL of ice cold FACS buffer. All samples were kept on ice, and fluorescence intensities were acquired on an LSRFortessa cytometer (BD Biosciences) through the FITC channel and analyzed via FlowJo.

Mito-Stress Test

To measure the effect of ZBTB7A-KO and C70 treatment on mitochondrial respiration, we used Agilent's Seahorse XF Cell Mito Stress Test Kit (Agilent, 103015-100). SUM149 cells expressing *ROSA26-g1* or *ZBTB7A-g1* from the lentiCRISPR v2 vector (see key resources table) were pre-treated with 0.01% DMSO or 10 μM C70 for a total of 6 days. The cells were first seeded in 10 cm dishes and treated with -/+ 10 μM C70 for 4 days. Afterwards, cells were trypsinized and re-seeded in Agilent Seahorse XF24 cell culture microplates (100777-004) for an additional 2 days of pre-treatment: 40,000 cells per well in 100 μL of media -/+ 10 μM C70. Cells were seeded such that they form a 100% confluent monolayer by the time of the assay. We then followed the protocol as described for the Seahorse XF Cell Mito Stress Test Kit (Agilent, 103015-100). The following final compound concentrations were used during the assay: 1.5 μM Oligomycin, 0.75 μM FCCP, and 0.5 μM Rotenone/Antimycin A.

QUANTIFICATION AND STATISTICAL ANALYSIS

Software used in this study

See key resources table. Visualization Pipeline for RNA-seq analysis (VIPER), Containerized Bioinformatics workflow for Reproducible ChIP/ATAC-seq Analysis (CoBRA), Model-based Analysis of Genome-wide CRISPR-Cas9 Knockout (MAGeCK) (v 0.5.9), Cell Ranger (v5.0.1), Seurat (v4.3.0), ERVmap (v1.1), deepTools2.0, RStudio (v 4.2.0), MAGeCKFlute (v1.14.0), ClusterProfiler (v4.2.2), ChIPseeker (v1.30.3), GenomicRanges (v1.46.1), Affinity Designer (v 1.10.4), GraphPadPrism (v 9), FlowJo (v 10.8.2).

ChIP-seq data analysis

Peak calling and data analysis

All samples were processed through the computational pipeline developed at the Dana-Farber Cancer Institute Center for Functional Cancer Epigenetics (CFCE) using primarily open-source programs.[60,72] Samples were analyzed in duplicates, and each sample was normalized to a 1% input. Sequence tags were aligned with Burrows-Wheeler Aligner (BWA)[73] to build hg19 and uniquely mapped, non-redundant reads were retained. These reads were used to generate binding sites with Model-Based Analysis of ChIP-Seq 2 (MACS v2.1.1.20160309), with a q-value (FDR) threshold of 0.01.[74] We evaluated multiple quality control criteria based on alignment information and peak quality: (i) sequence quality score; (ii) uniquely mappable reads (reads that can only map to one location in the genome); (iii) uniquely mappable locations (locations that can only be mapped by at least one read); (iv) peak overlap with Velcro regions, a comprehensive set of locations – also called consensus signal artifact regions – in the genome that have anomalous, unstructured high signal or read counts in next-generation sequencing experiments independent of cell line and of type of experiment; (v) number of total peaks (the minimum required was 10,000); (vi) high-confidence peaks (the number of peaks that are tenfold enriched over background); (vii) percentage overlap with known DHS sites derived from the ENCODE Project (the minimum required to meet the threshold was 80%); and (viii) peak conservation (a measure of sequence similarity across species based on the hypothesis that conserved sequences are more likely to be functional).

Peak cluster definitions

In Figures 3B and S3G, peak clusters were defined based on whether there was overlap in peak calls for ZBTB7A, KDM5A, and/or KDM5B in the untreated *ROSA26-g1* samples. Peaks were considered present for a given factor if they were called in both replicates and absent if there was no peak call in either replicate. Heatmaps were created with deepTools2.0 using the computeMatrix and plotHeatmap functions on the Glaxy server (https://usegalaxy.org/) using bigwig files from CoBRA[60] and self-defined peak regions as input. Feature annotations and nearest genes for each peak were obtained with the annotatePeak function from ChIPseeker (v1.30.3) in R (v4.1.3).

Differential binding analyses

Peaks from all samples were merged to create a union set of sites for each transcription factor and histone mark using bedops.[75] Sample-sample correlation and differential peaks analysis were performed by the CoBRA pipeline.[60] Read densities were calculated for each peak for each sample and used for the comparison of cistromes across samples. Sample similarity was determined by hierarchical clustering using the spearman correlation between samples. Differential peaks were identified by DEseq2 with adjusted $P \leq 0.05$. A total number of reads in each sample was applied to the size factor in Deseq2, which can normalize the sequencing depth between samples. KDM5A unchanged peaks (Figure 3) were defined as regions with KDM5A peak calls across all untreated *ROSA26-g1* replicates and padj > 0.05 for deseq between *ZBTB7A-KO* and *ROSA26-g1*.

Target gene identification, GSEA, and motif analysis: To identify target genes using only peak information, we used Cistrome-GO (http://go.cistrome.org/), which calculates regulatory potential scores for each gene based on both the number and proximity of peaks.[32] In Figures 3H–3J and S3J, we used the top 500 predicted target genes based on regulatory potential score to look for enrichment of certain pathways.

Overlap with Hallmark pathways was calculated using the compute overlap function from MSigDB (https://www.gsea-msigdb.org/gsea/msigdb/). Overlap with consensus transcription factor target genes from ENCODE/ChEA and overlap with transcription factor motifs from TRANSFAC/JASPAR were calculated using enrichr (https://maayanlab.cloud/Enrichr/). To assess similarity of our peak sets with published ChIP-seq tracks, we used the Cistrome DB toolkit (http://dbtoolkit.cistrome.org/) "What factors have significant overlap with your peak set?" with peak number to use set to "All peaks in each sample". The Giggle scores from this analysis (-log1 (padj)*odds ratio from Fisher's Exact Test, see Layer et al. 2018 for more information) are plotted in Figures 3K and S3I.[33,34] In Figure S3I, only the maximum Giggle scores identified for each factor are plotted. To determine the regulatory potential of each peak set, we performed binding and expression target analysis (BETA), in which we integrated the peak information with RNA-seq comparing the ZBTB7A KO and wild-type SUM149 cells.[32] For promoter-enriched peak sets (e.g., KDM5A down and ZBTB7A+KDM5A/B), we used a window of 3 kb from each gene's TSS to select peaks, and for non-promoter enriched peak sets (i.e., ZBTB7A unique), we used the default parameter of 100 kb. To annotate the genes in the volcano plots with their nearest peaks, we used the output from the annotatePeak function in the ChIPseeker (v1.30.3) package. The p values in these graphs are from the previously described BETA analyses. Finally, for enrichment analyses, we selected high probability target genes for each peak set based on a rank product score of less than 0.001 from the BETA output. Enrichment of transcription factor motifs from published ChIP-seq across Cistrome was calculated using the epigenetic Landscape In Silico deletion Analysis (Lisa) tool (http://lisa.cistrome.org/). Overlap with Hallmark pathways was calculated using the compute overlap function from MSigDB (https://www.gsea-msigdb.org/gsea/msigdb/). Motif enrichment scores were calculated using simple enrichment analysis from MEME-suite (https://meme-suite.org/meme/doc/sea.html) for ZBTB7A consensus sequence GACCC. Default shuffled input sequences were used as control.

RNA-seq data analysis

RNA-seq data was analyzed using the Visualization Pipeline for RNA-seq analysis (VIPER) and aligned to version hg19 of the human genome[59] The following config.yaml parameters were adjusted: RPKM_threshold = 1.0 and min_num_samples_expressing_at_threshold = 2. Samples were analyzed in duplicates. GSEA was performed by ranking genes based on log2(FC) and using the GSEA function from the ClusterProfiler (v4.2.2) package in R. Public gene sets tested in the manuscript include MSigDB's Hallmark (H1) and positional gene sets (C1), KEGG, and Reactome. TNBC subtypes used for GSEA in Figure S4K were from our prior publication.[39] The heatmaps in Figures S2D and 4A are the default output of VIPER, which used the top 1,000 variable genes for plotting. PCA plots were computed using log2 transformed count data of all genes within each sample with the prcomp function form the stats (v4.1.3) package in R. The heatmap in Figure 5D was created using all C70-responsive DEGs, which were defined as padj < 0.05 when comparing -/+ C70 in either SUM149 ROSA26-g1 or SUM149 ZBTB7A-g1. The heatmap was generated using row normalized Z-scores of FPKM values with the ComplexHeatmap (v2.10.0) function in R. Rows were clustered via k-means with k = 5. Enrichment of gene sets within the heatmap clusters was determined using the enricher function from the clusterProfiler (v4.2.2) package in R. Transcription factor target gene sets were taken from "TFT: transcription factor targets" in MSigDB.

TCGA and METABRIC data analyses: Because these cohorts are bulk RNA-seq, we used the ISOpure algorithm to estimate gene expression levels specifically coming from the tumor fraction and used these deconvoluted matrices[76] for the analyses. First, we assessed if KDM5 activity correlated with select Hallmark pathways we found to be influenced by KDM5 inhibition in our study. We used average expression of *KDM5A* and *KDM5B* as a surrogate for KDM5 activity and tested for correlation with pathway enrichment scores (gene set variation analysis, GSVA) across basal TCGA samples.[77] Immune scores were calculated from bulk RNA-seq via "Estimation of STromal and Immune cells in MAlignant Tumours using Expression data" (ESTIMATE).[78]

Endogenous retroelement expression analysis

Differential expression of endogenous retroelements was assessed from bulk RNA-seq data using the ERVmap pipeline (v1.1).[41]

CRISPR screen data analysis

CRISPR data were analyzed by MAGeCK (v0.5.9) essentially as described[79–81] Briefly, read counts for each sgRNA were obtained from fastq files with mageck count.[61] To obtain significantly enriched and depleted sgRNAs in the C70 treated versus untreated samples, we used the MAGeCK TEST algorithm, in which read counts were normalized to a set of 3,842 control guides targeting the AAVS1 (3,540), CCR5 (99), and ROSA26 (203) loci. Genes with p value less than 0.001 were defined as candidate hits and colored in the rank plots in Figure 2. The MageckFlute package (v1.14.0)[61] was used to visualize the data.

scRNA-seq data analysis

Raw bcl2 files from the NovaSeq run were converted to fastq using cellranger mkfastq (Cell Ranger v5.0.1). Count information was obtained using cellranger count and aligned to the GRCh38 reference transcriptome provided by 10X: refdata-gex-GRCh38-2020-A.tar.gz. The filtered h5 files output from cellranger count were then loaded and analyzed with Seurat (v4.3.0). To remove poor quality cells, cells with less than 1,000 total RNA counts or percent mitochondrial counts greater than 3 absolute deviations from the median were filtered out. To remove doublets, cells with total RNA greater than 3 absolute deviations from the median were also filtered out. The filtered data was then normalized with Seurat's NormalizeData function, which normalized the gene expression for each cell by total expression, and then multiplied by a scaling factor of 10,000 and log-transformed the results. We identified the top 2,000 most variable features using FindVariableFeatures with selection.method = "vst". The data was then scaled using ScaleData, which makes the mean expression across cells 0 and variance 1. The scaled data was then used for clustering and visualization via UMAP using the first 30 PC dimensions. Hexagonal plots were created as we previously described.[10,82] Code to generate the plots was generated by Dr. Hua-Jun Wu and can be found on Bitbucket (https://bitbucket.org/mthjwu/hexplot/src/master/). To create the hexagonal plots, we first defined cell identity signatures for SUM149, C70 (i.e., SUM149 + 10 μM C70 for 7 days), and SUM149CR. For each cell type, we compared its bulk RNA-seq (3 replicates) with the other two cell types combined (3 replicates each) and obtained DEGs via deseq. We chose the top 66 up- and down-regulated genes based on padj values as the up- and down-signatures of each cell type. The top 66 genes were chosen since this was the smallest number of DEGs (padj<0.05) identified for a given cell type, and we sought to use the same number of genes to define each gene signature. Using these gene signatures, we then calculated cell identity scores for each cell within our filtered and scaled scRNA-seq data set. The cell identity score was the average scaled expression of the up-gene signature minus the average scaled expression of the down- gene signature. We randomly selected 1,000 sets of up and down signatures, each matching the size of the original true signatures, which allowed us to generate a bootstrap distribution for the cell identity score. From this distribution, we calculated the bootstrap p-value. Single cells were then classified based on this p-value, using a cutoff of 5%. Cells that didn't meet the threshold for any signature were labeled as unclassified. Hexagonal plots were utilized to visually represent the bootstrap classification of single cells within SUM149 and SUM149CR -/+ C70. Cells that clearly exhibited identity (i.e., passed the 5% threshold for only 1 of the 3 identities) were positioned along the edge of the plot. Cell-to-cell distance were calculated in each group using "Embeddings" function of the Seurat package with PCA dimension reduction. Gini indexes of all the genes within each group were calculated using "ineq" package.

qPLEX RIME data analysis

Peptide intensities were normalized using median scaling and protein level quantification was obtained by the summation of the normalized peptide intensities. A statistical analysis of differentially-regulated proteins was carried out using qPLEXanalyzer a Bioconductor R-package.[31], which internally uses limma R-package from Bioconductor.[83] Multiple testing correction of p-values was applied using the Benjamini-Hochberg method.[84] to control the false discovery rate.

Cell Reports, Volume *43*

Supplemental information

ZBTB7A is a modulator of KDM5-driven transcriptional networks in basal breast cancer

Benedetto DiCiaccio, Marco Seehawer, Zheqi Li, Andriana Patmanidis, Triet Bui, Pierre Foidart, Jun Nishida, Clive S. D'Santos, Evangelia K. Papachristou, Malvina Papanastasiou, Andrew H. Reiter, Xintao Qiu, Rong Li, Yijia Jiang, Xiao-Yun Huang, Anton Simeonov, Stephen C. Kales, Ganesha Rai, Madhu Lal-Nag, Ajit Jadhav, Myles Brown, Jason S. Carroll, Henry W. Long, and Kornelia Polyak

SUPPLEMENTARY FIGURES

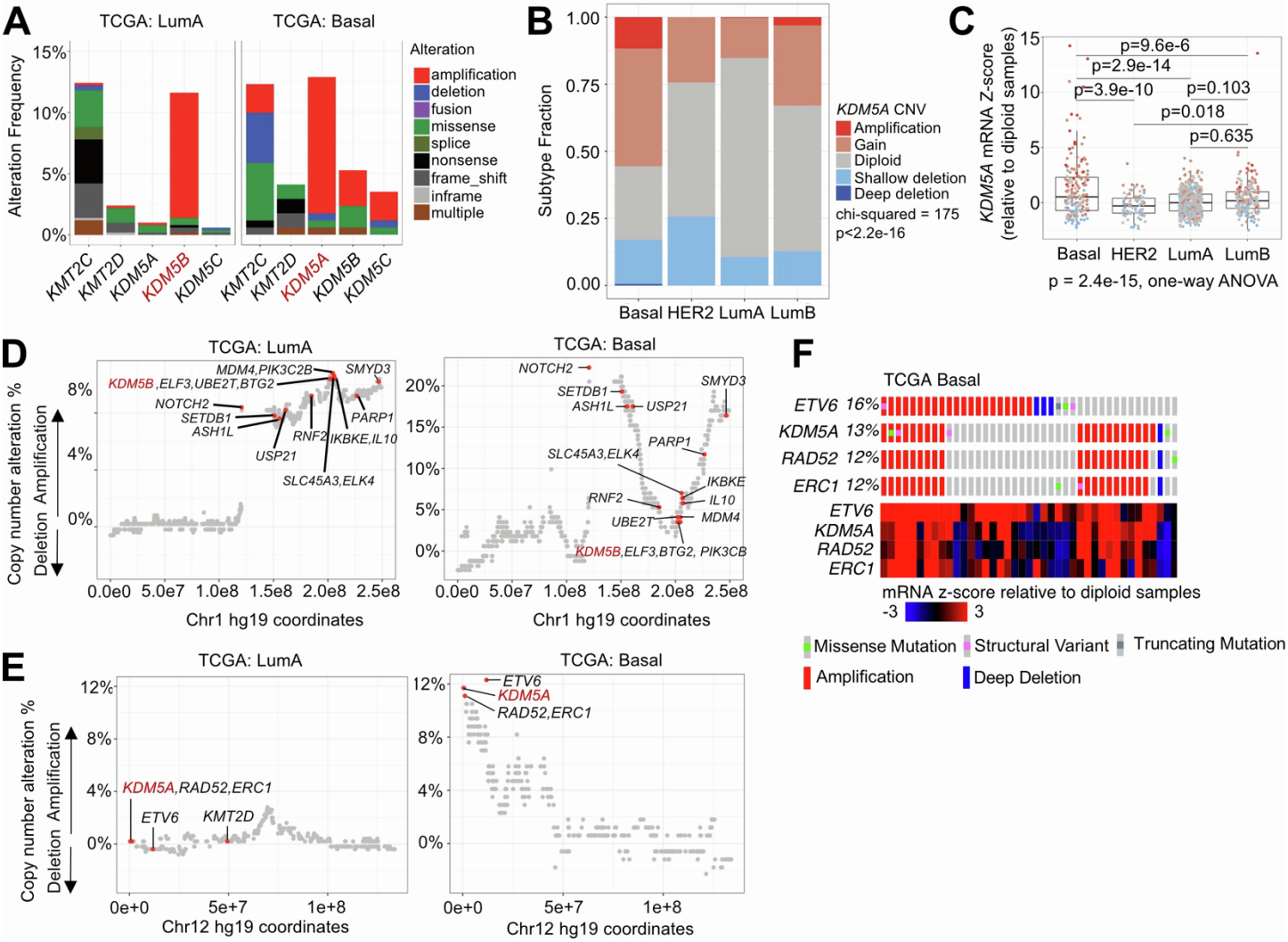

Figure S1. *KDM5A* is commonly amplified in basal breast cancer.
(A) Stacked bar chart depicting the frequencies of genetic alterations in genes encoding H3K4 methyltransferases (KMT2 family) and H3K4 demethylases (KDM5 family) in the LumA and basal PAM50 breast cancer subtypes in the TCGA cohort.
(B) Stacked bar chart showing fraction of tumors with *KDM5A* copy number variation (CNV) within each PAM50 breast cancer subtype. Chi- squared = 175, p<2.2e-16.
(C) Box plot showing distribution of *KDM5A* mRNA Z-scores across the PAM50 breast cancer subtypes. One-way ANOVA p=2.38e-15. Pairwise t-tests with Bonferroni corrections are shown.
(D-E) Amplification/deletion frequencies of individual genes mapped to their positions across chromosomes 1 or 12 in LumA and Basal breast cancer. Frequently amplified cancer-associated genes, based on OncoKB, are labelled.
(F) Oncoprint of *ETV6*, *KDM5A*, *RAD52*, and *ERC1* across basal breast cancer samples.

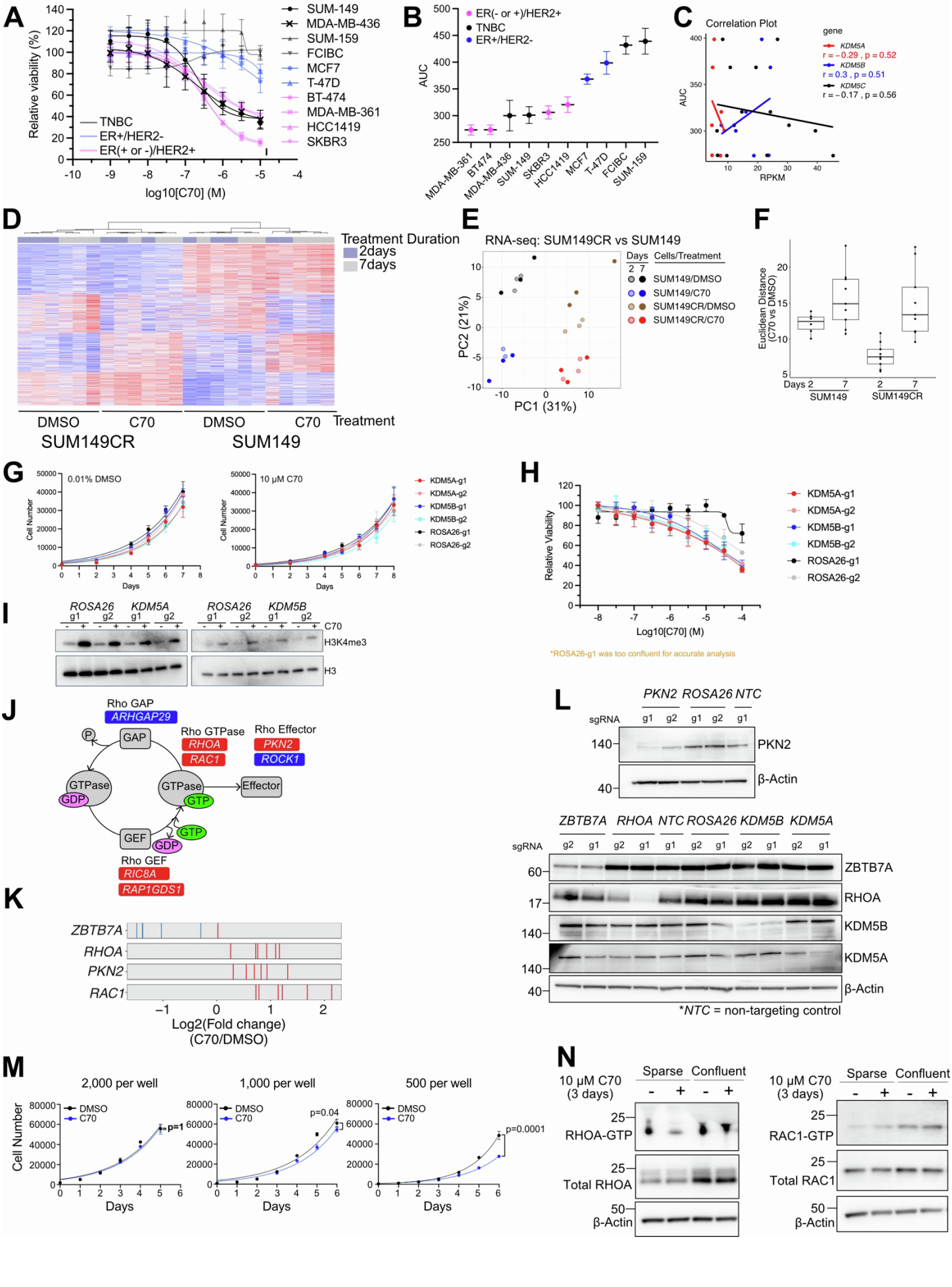
A
Relative viability (%)
log10[C70] (M)
SUM-149
MDA-MB-436
SUM-159
FCIBC
MCF7
T-47D
BT-474
MDA-MB-361
HCC1419
SKBR3
TNBC
ER+/HER2-
ER(+ or -)/HER2+
B
AUC
ER(- or +)/HER2+
TNBC
ER+/HER2-
C
Correlation Plot
gene
KDM5A
r = −0.29 , p = 0.52
KDM5B
r = 0.3 , p = 0.51
KDM5C
r = −0.17 , p = 0.56
RPKM
D
Treatment Duration
2days
7days
DMSO
C70
DMSO
C70
Treatment
SUM149CR
SUM149
E
RNA-seq: SUM149CR vs SUM149
Days
Cells/Treatment
SUM149/DMSO
SUM149/C70
SUM149CR/DMSO
SUM149CR/C70
PC2 (21%)
PC1 (31%)
F
Euclidean Distance (C70 vs DMSO)
Days
SUM149
SUM149CR
G
0.01% DMSO
10 μM C70
Cell Number
Days
KDM5A-g1
KDM5A-g2
KDM5B-g1
KDM5B-g2
ROSA26-g1
ROSA26-g2
H
Relative Viability
Log10[C70] (M)
*ROSA26-g1 was too confluent for accurate analysis
I
ROSA26
KDM5A
KDM5B
C70
H3K4me3
H3
J
Rho GAP
ARHGAP29
Rho GTPase
RHOA
RAC1
Rho Effector
PKN2
ROCK1
GAP
GTPase
GDP
GTP
Effector
GEF
Rho GEF
RIC8A
RAP1GDS1
K
ZBTB7A
RHOA
PKN2
RAC1
Log2(Fold change)
(C70/DMSO)
L
PKN2
ROSA26
NTC
sgRNA
PKN2
β-Actin
ZBTB7A
RHOA
NTC
ROSA26
KDM5B
KDM5A
*NTC = non-targeting control
M
2,000 per well
1,000 per well
500 per well
Cell Number
DMSO
C70
p=1
p=0.04
p=0.0001
Days
N
10 μM C70
(3 days)
Sparse
Confluent
RHOA-GTP
Total RHOA
β-Actin
RAC1-GTP
Total RAC1
β-Actin

Figure S2. CRISPR viability screen to identify modulators of KDM5 inhibitor sensitivity. Related to Figure 2.

(A) Dose-response curves to the KDM5 inhibitor C70 across a panel of breast cancer cell lines of the indicated subtype. Mean -/+ standard deviation is shown (n = 6).

(B) Area under the curve calculated from panel A renormalized to the lowest C70 concentration. Error bars are 95% confidence intervals. Error was propagated from error bars in panel A when calculating the AUC of Fig. S3A)

(C) Plot depicting Pearson correlation between C70-sensitivity and expression level of KDM5A/B/C across cell lines. AUC = area under the curve for % viability DMSO vs C70. RPKM values were obtained from the cancer cell line encyclopedia.

(D) Heatmap of RNA-seq in SUM149 and SUM149CR cells -/+ 10 μM C70 for 2 or 7 days. Rows and columns are ordered based on hierarchical clustering. Values are row normalized Z-scores.

(E) PCA plot of RNA-seq data in SUM149 and SUM149CR -/+ 10 μM C70 for 2 or 7 days.

(F) Euclidean distance between PC1/PC2 coordinates of treated and untreated samples in panel D.

(G,H) Growth curves (G) and IC50 plots (H) illustrating the viable cell numbers of SUM149 ROSA26, *KDM5A* or *KDM5B* knockout cell lines growing in DMSO or 10 μM C70.

(I) Immunoblot analysis for H3K4me3 in SUM149 ROSA26, *KDM5A* or *KDM5B* knockout cell lines after growth for three days in DMSO or 10 μM C70.

(J) Diagram of the Rho-GTPase cycle with significant hits from the SUM149 CRISPR screen labelled. Red = enriched in C70, blue = enriched in DMSO.

(K) Log2(fold change) of individual sgRNAs from the CRISPR screen in SUM149 -/+ 10 μM C70. Positive log2(fold change) indicates enrichment in C70.

(L) Immunoblot validating deletion of the indicated genes with individual gRNAs targeting top hits from the CRISPR screen in SUM149.

(M) Growth curves of SUM149 cells seeded at varying densities and treated with -/+ 10 μM C70. Cells were seeded at 2,000, 1,000, or 500 cells per well in a 96-well plate. Data are mean -/+ standard deviation (n=6). Statistical analysis for growth curves was performed using two-way repeated measures ANOVA followed by Bonferroni's multiple comparisons test; the significance at the last time point compared to is shown.

(N) Levels of Active RHOA-GTP and RAC1-GTP levels -/+ 10 μM C70 (3 days) in SUM149 cells. Active RHOA and RAC1 pulldowns were performed with GST-Rhotekin-RBD and GST-Pak1-PBD beads, respectively.

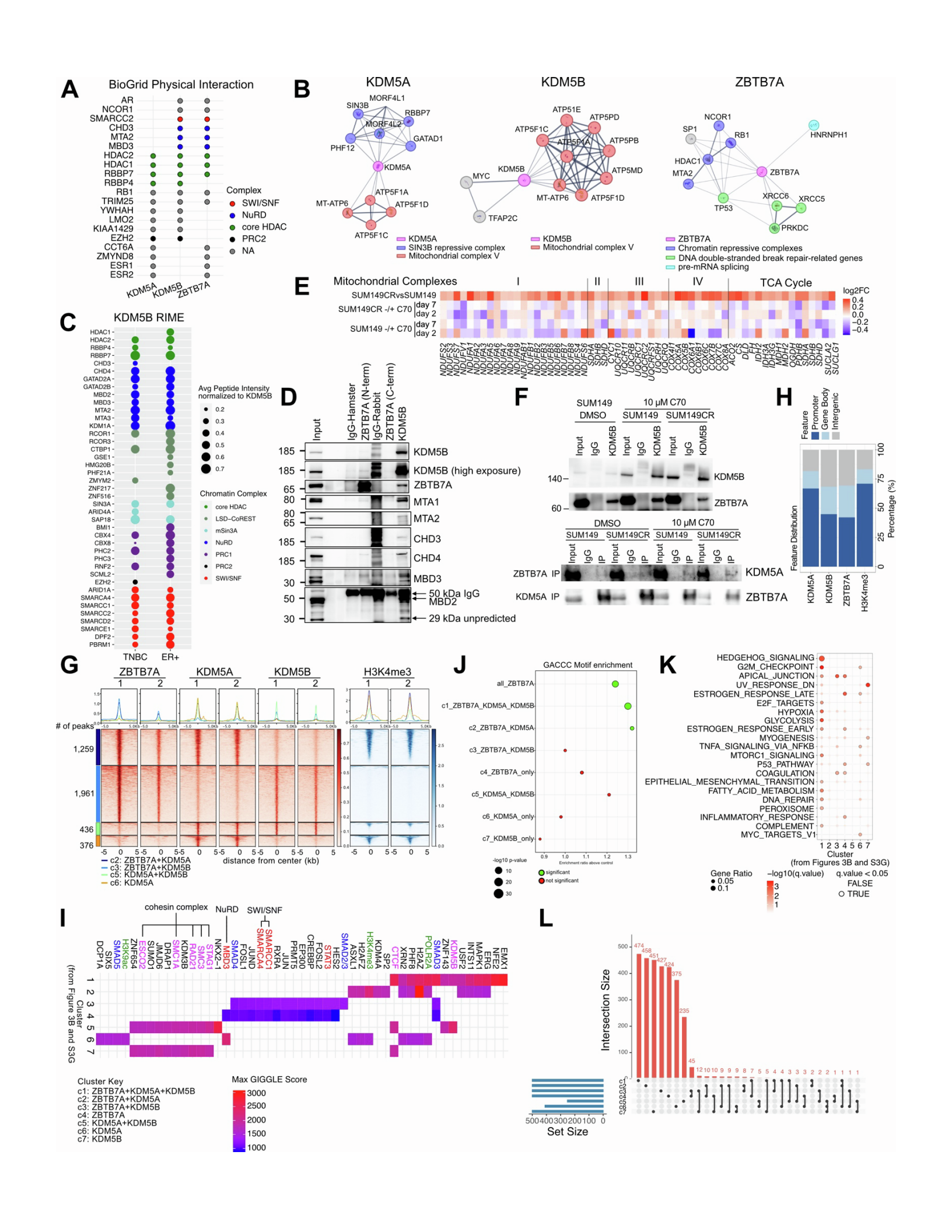
A
BioGrid Physical Interaction
AR
NCOR1
SMARCC2
CHD3
MTA2
MBD3
HDAC2
HDAC1
RBBP7
RBBP4
RB1
TRIM25
YWHAH
LMO2
KIAA1429
EZH2
CCT6A
ZMYND8
ESR1
ESR2
KDM5A
KDM5B
ZBTB7A
Complex
SWI/SNF
NuRD
core HDAC
PRC2
NA
B
KDM5A
MORF4L1
SIN3B
RBBP7
MORF4L2
GATAD1
PHF12
KDM5A
ATP5F1A
MT-ATP6
ATP5F1D
ATP5F1C
KDM5A
SIN3B repressive complex
Mitochondrial complex V
KDM5B
ATP51E
ATP5PD
ATP5F1C
ATP5PB
ATP5F1A
ATP5MD
KDM5B
MYC
MT-ATP6
ATP5F1D
TFAP2C
KDM5B
Mitochondrial complex V
ZBTB7A
NCOR1
SP1
RB1
HNRNPH1
HDAC1
MTA2
ZBTB7A
XRCC6
XRCC5
TP53
PRKDC
ZBTB7A
Chromatin repressive complexes
DNA double-stranded break repair-related genes
pre-mRNA splicing
C
KDM5B RIME
HDAC1
HDAC2
RBBP4
RBBP7
CHD3
CHD4
GATAD2A
GATAD2B
MBD2
MBD3
MTA2
MTA3
KDM1A
RCOR1
RCOR3
CTBP1
GSE1
HMG20B
PHF21A
ZMYM2
ZNF217
ZNF516
SIN3A
ARID4A
SAP18
BMI1
CBX4
CBX8
PHC2
PHC3
RNF2
SCML2
EZH2
ARID1A
SMARCA4
SMARCC1
SMARCC2
SMARCD2
SMARCE1
DPF2
PBRM1
TNBC
ER+
Avg Peptide Intensity normalized to KDM5B
0.2
0.3
0.4
0.5
0.6
0.7
Chromatin Complex
core HDAC
LSD–CoREST
mSin3A
NuRD
PRC1
PRC2
SWI/SNF
D
Input
IgG-Hamster
ZBTB7A (N-term)
IgG-Rabbit
ZBTB7A (C-term)
KDM5B
185
KDM5B
185
KDM5B (high exposure)
65
ZBTB7A
80
MTA1
80
65
MTA2
185
CHD3
185
CHD4
30
MBD3
50
50 kDa IgG
MBD2
30
29 kDa unpredicted
E
Mitochondrial Complexes
I
II
III
IV
TCA Cycle
SUM149CRvsSUM149
SUM149CR -/+ C70
day 7
day 2
SUM149 -/+ C70
day 7
day 2
log2FC
0.4
0.2
0.0
−0.2
−0.4
NDUFS2
NDUFS3
NDUFV1
NDUFA1
NDUFA2
NDUFA3
NDUFA5
NDUFA6
NDUFA7
NDUFA8
NDUFA9
NDUFAB1
NDUFB2
NDUFB3
NDUFB5
NDUFB6
NDUFB7
NDUFB8
NDUFB9
NDUFS4
NDUFS6
SDHA
SDHB
SDHC
UQCR10
UQCR11
UQCRB
UQCRC1
UQCRC2
UQCRFS1
UQCRH
UQCRQ
COX4I1
COX5A
COX6A1
COX6B1
COX6C
COX7B
COX8A
ACO2
CS
DLD
IDH1
IDH3A
IDH3G
MDH1
MDH2
OGDH
SDHA
SDHB
SDHD
SUCLA2
SUCLG1
F
SUM149
10 μM C70
DMSO
SUM149
SUM149CR
Input
IgG
KDM5B
140
KDM5B
60
ZBTB7A
DMSO
10 μM C70
SUM149
SUM149CR
ZBTB7A IP
KDM5A
KDM5A IP
ZBTB7A
H
Feature
Promoter
Gene Body
Intergenic
Feature Distribution
Percentage (%)
KDM5A
KDM5B
ZBTB7A
H3K4me3
G
ZBTB7A
KDM5A
KDM5B
H3K4me3
# of peaks
1,259
1,961
436
376
distance from center (kb)
c2: ZBTB7A+KDM5A
c3: ZBTB7A+KDM5B
c5: KDM5A+KDM5B
c6: KDM5A
J
GACCC Motif enrichment
all_ZBTB7A
c1_ZBTB7A_KDM5A_KDM5B
c2_ZBTB7A_KDM5A
c3_ZBTB7A_KDM5B
c4_ZBTB7A_only
c5_KDM5A_KDM5B
c6_KDM5A_only
c7_KDM5B_only
Enrichment ratio above control
-log10 p-value
significant
not significant
K
HEDGEHOG_SIGNALING
G2M_CHECKPOINT
APICAL_JUNCTION
UV_RESPONSE_DN
ESTROGEN_RESPONSE_LATE
E2F_TARGETS
HYPOXIA
GLYCOLYSIS
ESTROGEN_RESPONSE_EARLY
MYOGENESIS
TNFA_SIGNALING_VIA_NFKB
MTORC1_SIGNALING
P53_PATHWAY
COAGULATION
EPITHELIAL_MESENCHYMAL_TRANSITION
FATTY_ACID_METABOLISM
DNA_REPAIR
PEROXISOME
INFLAMMATORY_RESPONSE
COMPLEMENT
MYC_TARGETS_V1
Cluster
(from Figures 3B and S3G)
Gene Ratio
0.05
0.1
−log10(q.value)
q.value < 0.05
FALSE
TRUE
I
cohesin complex
NuRD
SWI/SNF
DCP1A
SIX5
SMAD5
H3K9ac
ZNF654
ESCO2
SUMO1
JMJD6
DRAP1
SMC1A
KDM3B
RAD21
SMC3
STAG1
NKX2−1
MBD3
SMAD4
FOSL1
JUND
SMARCA4
SMARCC1
RXRA
RUNX1
PRMT5
EP300
CREBBP
FOSL2
STAT3
HES2
SMAD2/3
ASXL1
H2AFZ
H3K4me3
KDM4A
SP2
CTCF
XRN2
PHF8
H2AZ
POLR2A
SMAD3
ZNF143
KDM5B
USF2
INTS11
MAPK1
ERG
NFE2
EMX1
Cluster
(from Figure 3B and S3G)
Cluster Key
c1: ZBTB7A+KDM5A+KDM5B
c2: ZBTB7A+KDM5A
c3: ZBTB7A+KDM5B
c4: ZBTB7A
c5: KDM5A+KDM5B
c6: KDM5A
c7: KDM5B
Max GIGGLE Score
3000
2500
2000
1500
1000
L
Intersection Size
474
458
451
427
424
375
235
45
12
10
10
9
9
9
8
7
5
5
4
4
3
3
3
2
2
2
1
1
1
1
Set Size
500
400
300
200
100
0

Figure S3. ZBTB7A and KDM5A/B interactomes and chromatin patterns. Related to Figure 3.
(A) List of physical interactions reported in BioGrid that have experimental evidence for KDM5A, KDM5B, and ZBTB7A. Common interactors between ZBTB7A and KDM5A/KDM5B are shown.
(B) The edges indicate that the proteins are part of a physical complex, and the data is based on known interactions based on experiments or curated databased. The edge thickness indicates edge confidence. The interactions are non-exhaustive, in which the parameters were set to display a maximum of 10 interactions, and all interaction scores had to be above 0.4.
(C) KDM5B-associated proteins identified by qPLEX-RIME. The average peptide intensity normalized to KDM5B within TNBC (SUM149 and SUM159) and luminal ER+ (MCF7 and T47D) cell lines tested are shown.
(D) Immunoblot for NuRD subunits in ZBTB7A and KDM5B immunoprecipitants. Both N-terminal and C-terminal targeting antibodies were tested against ZBTB7A (labelled). Only the N-term targeting antibody successfully immunoprecipitated ZBTB7A.
(E) Heatmap depicting log2(FC) from RNA-seq in SUM149 and SUM149CR cells for the specified OXPHOS-related genes. The represented genes drive the leading edge of the GSEA analysis in Figure 1B.
(F) Immunoblot analysis of ZBTB7A and KDM5B or KDM5A in total cell lysates (input), control IgG and KDM5B, KDM5A or ZBTB7A immunoprecipitants in SUM149 and SUM149CR cells treated with DMSO or 10 μM C70 for 3 days.
(G) Heatmap of ChIP-seq for ZBTB7A, KDM5A, KDM5B, and H3K4me3. Peaks are clustered based on the intersection of peak calls among the three proteins.
(H) Feature distribution plot of KDM5A, KDM5B, ZBTB7A, and H3K4me3 ChIP-seq peaks in SUM149 cells.
(I) Factors with significant binding overlap with the identified ChIP-seq peaks in **Figures 3B, S3G**. Overlap is assessed via the Giggle score computed from CISTROME DB's toolkit. The maximum Giggle score is reported per comparison.
(J) Bubble plot showing enrichment ratios above controls of GACCC motif separated by cluster from Figure 3B and S3G.
(K) Overlap of the top 500 predicted target genes within each ChIP-seq cluster from **Figures 3B, S3G** with Hallmark pathways. Top genes were identified based on regulatory potential scores from BETA-minus.
(L) Overlap between the top 500 predicted target genes across cluster from **Figures 3B, S3G**.

Fig. S4

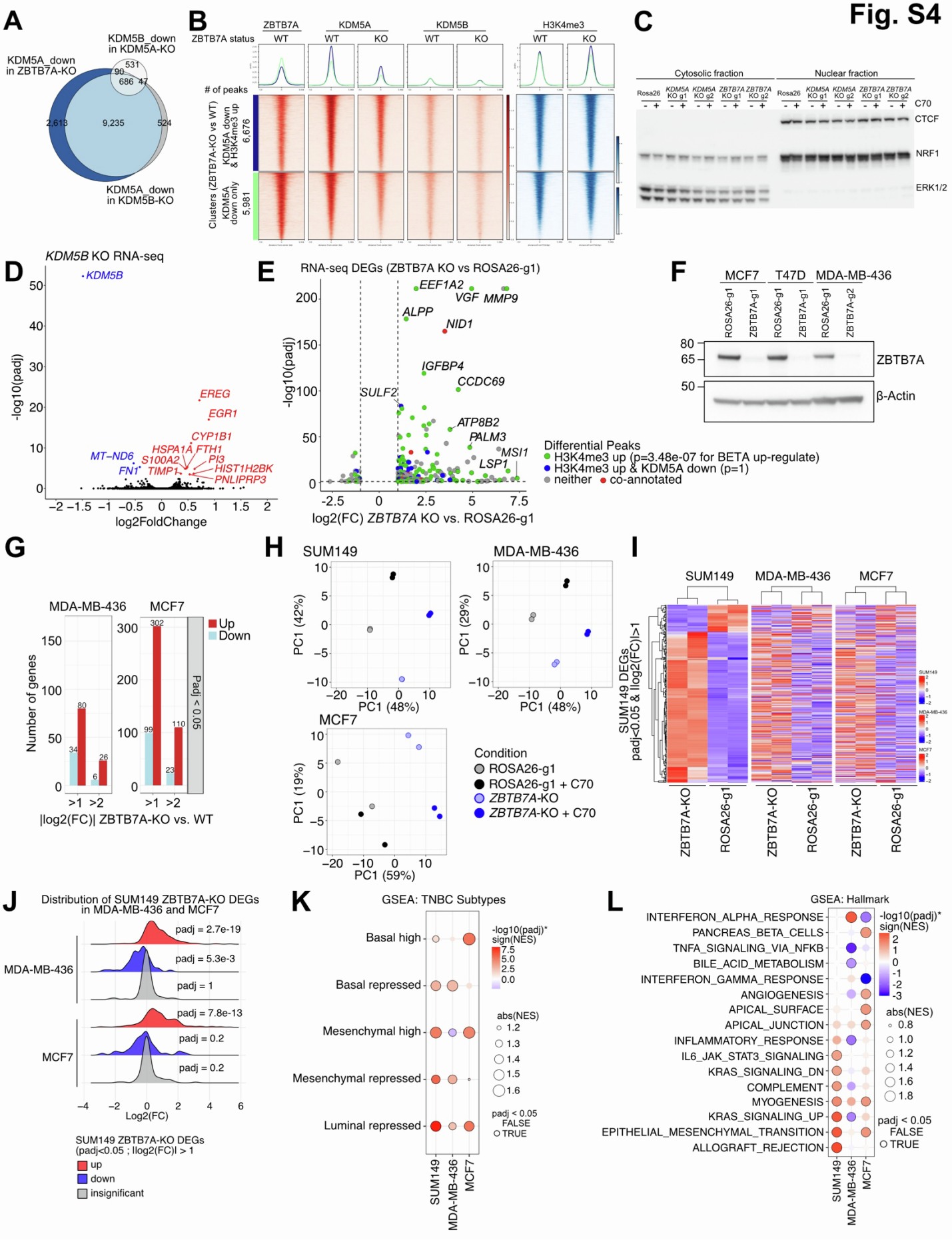
A
KDM5B_down in KDM5A-KO
KDM5A_down in ZBTB7A-KO
KDM5A_down in KDM5B-KO
531
90
686
47
2,618
9,235
524
B
ZBTB7A
KDM5A
KDM5B
H3K4me3
ZBTB7A status
WT
KO
# of peaks
Clusters (ZBTB7A-KO vs WT)
KDM5A down & H3K4me3 up
6,676
KDM5A down only
5,981
C
Cytosolic fraction
Nuclear fraction
Rosa26
KDM5A KO g1
KDM5A KO g2
ZBTB7A KO g1
ZBTB7A KO g2
C70
CTCF
NRF1
ERK1/2
D
KDM5B KO RNA-seq
KDM5B
EREG
EGR1
CYP1B1
HSPA1A
FTH1
MT-ND6
S100A2
PI3
FN1
TIMP1
HIST1H2BK
PNLIPRP3
-log10(padj)
log2FoldChange
E
RNA-seq DEGs (ZBTB7A KO vs ROSA26-g1)
EEF1A2
VGF
MMP9
ALPP
NID1
IGFBP4
CCDC69
SULF2
ATP8B2
PALM3
MSI1
LSP1
-log10(padj)
log2(FC) ZBTB7A KO vs. ROSA26-g1
Differential Peaks
H3K4me3 up (p=3.48e-07 for BETA up-regulate)
H3K4me3 up & KDM5A down (p=1)
neither
co-annotated
F
MCF7
T47D
MDA-MB-436
ROSA26-g1
ZBTB7A-g1
ZBTB7A-g2
ZBTB7A
β-Actin
G
MDA-MB-436
MCF7
Up
Down
Number of genes
Padj < 0.05
|log2(FC)| ZBTB7A-KO vs. WT
H
SUM149
MDA-MB-436
MCF7
PC1 (42%)
PC1 (29%)
PC1 (19%)
PC1 (48%)
PC1 (59%)
Condition
ROSA26-g1
ROSA26-g1 + C70
ZBTB7A-KO
ZBTB7A-KO + C70
I
SUM149
MDA-MB-436
MCF7
SUM149 DEGs padj<0.05 & |log2(FC)|>1
ZBTB7A-KO
ROSA26-g1
J
Distribution of SUM149 ZBTB7A-KO DEGs in MDA-MB-436 and MCF7
MDA-MB-436
MCF7
padj = 2.7e-19
padj = 5.3e-3
padj = 1
padj = 7.8e-13
padj = 0.2
padj = 0.2
Log2(FC)
SUM149 ZBTB7A-KO DEGs (padj<0.05 ; |log2(FC)| > 1
up
down
insignificant
K
GSEA: TNBC Subtypes
Basal high
Basal repressed
Mesenchymal high
Mesenchymal repressed
Luminal repressed
-log10(padj)* sign(NES)
abs(NES)
padj < 0.05
FALSE
TRUE
SUM149
MDA-MB-436
MCF7
L
GSEA: Hallmark
INTERFERON_ALPHA_RESPONSE
PANCREAS_BETA_CELLS
TNFA_SIGNALING_VIA_NFKB
BILE_ACID_METABOLISM
INTERFERON_GAMMA_RESPONSE
ANGIOGENESIS
APICAL_SURFACE
APICAL_JUNCTION
INFLAMMATORY_RESPONSE
IL6_JAK_STAT3_SIGNALING
KRAS_SIGNALING_DN
COMPLEMENT
MYOGENESIS
KRAS_SIGNALING_UP
EPITHELIAL_MESENCHYMAL_TRANSITION
ALLOGRAFT_REJECTION
-log10(padj)* sign(NES)
abs(NES)
padj < 0.05
FALSE
TRUE
SUM149
MDA-MB-436
MCF7

Figure S4. Gene expression changes induced by *ZBTB7A* KO and its impact on ZBTB7A and KDM5A/B peak sets. Related to Figure 4.

(A) Venn diagram comparing KDM5A peaks that decrease in the *ZBTB7A* KO or *KDM5B* KO along with KDM5B peaks that decrease in the *KDM5A* KO SUM149 cells.

(B) ChIP-seq signal intensity across all regions with a significant reduction in KDM5A signal (padj < 0.05) upon *ZBTB7A* deletion. Peaks are separated into those associated with a significant increase in H3K4me3 (padj < 0.05) upon *ZBTB7A* KO or not.

(C) Immunoblot analysis of NRF1 in nuclear and cytoplasmic fraction in the indicated cell lines and treatment. CTCF and ERK1/2 were used as controls for loading and subcellular localization.

(D) Volcano plot of differentially expressed genes (padj < 0.05; |log2(FC)| > 1) in SUM149 *ZBTB7A* KO vs ROSA26-g1. The nearest genes to differential peaks are annotated. P-values are based on binding and expression target analysis (BETA), indicating if the differential peak set is significantly associated with up- or down-regulated genes. Dashed gray lines indicate adjusted p value and fold change cut offs used for defining DGEs in RNA-seq.

(E) Volcano plot depicting genes differentially expressed between ZBTB7A KO vs. ROSA26-g1 SUM149 cells and are associated with H3K4me3 and/or KDM5A peaks showing the indicated changes.

(F) Immunoblot for ZBTB7A in parental and *ZBTB7A* KO MCF7 and MDA-MB-436 cell lines.

(G) Number of up and down-regulated DEGs upon *ZBTB7A* KO in MDA-MB-436 and MCF7 cells.

(H) PCA plots from RNA-seq of indicated cell lines with *ZBTB7A* KO or ROSA26-g1 -/+ 10 μM c70 for 7 days.

(I) Heatmap of SUM149 DEGs (padj < 0.05 and |log2(FC)| > 1) upon *ZBTB7A* KO. The DEGs are compared across SUM149, MDA-MB-436, and MCF7 cell lines. Rows are ordered based on hierarchical clustering of the SUM149 data. Values are row normalized Z-scores within each cell line.

(J) Log2(FC) distribution of SUM149 *ZBTB7A* KO DEGs (differentially expressed genes) in the MDA-MB-436 and MCF7 cell lines. P-values are based on GSEA using the SUM149 DEGs as the reference gene sets. A random selection of 102 insignificant genes from SUM149 were used as a control.

(K,L) Gene-set enrichment of differentially expressed genes comparing *ZBTB7A* -g1 and ROSA26-g1 within the SUM149, MDA-MB-436, and MCF7 cell lines. Enrichment of TNBC subtypes (K) and Hallmark gene sets (L).

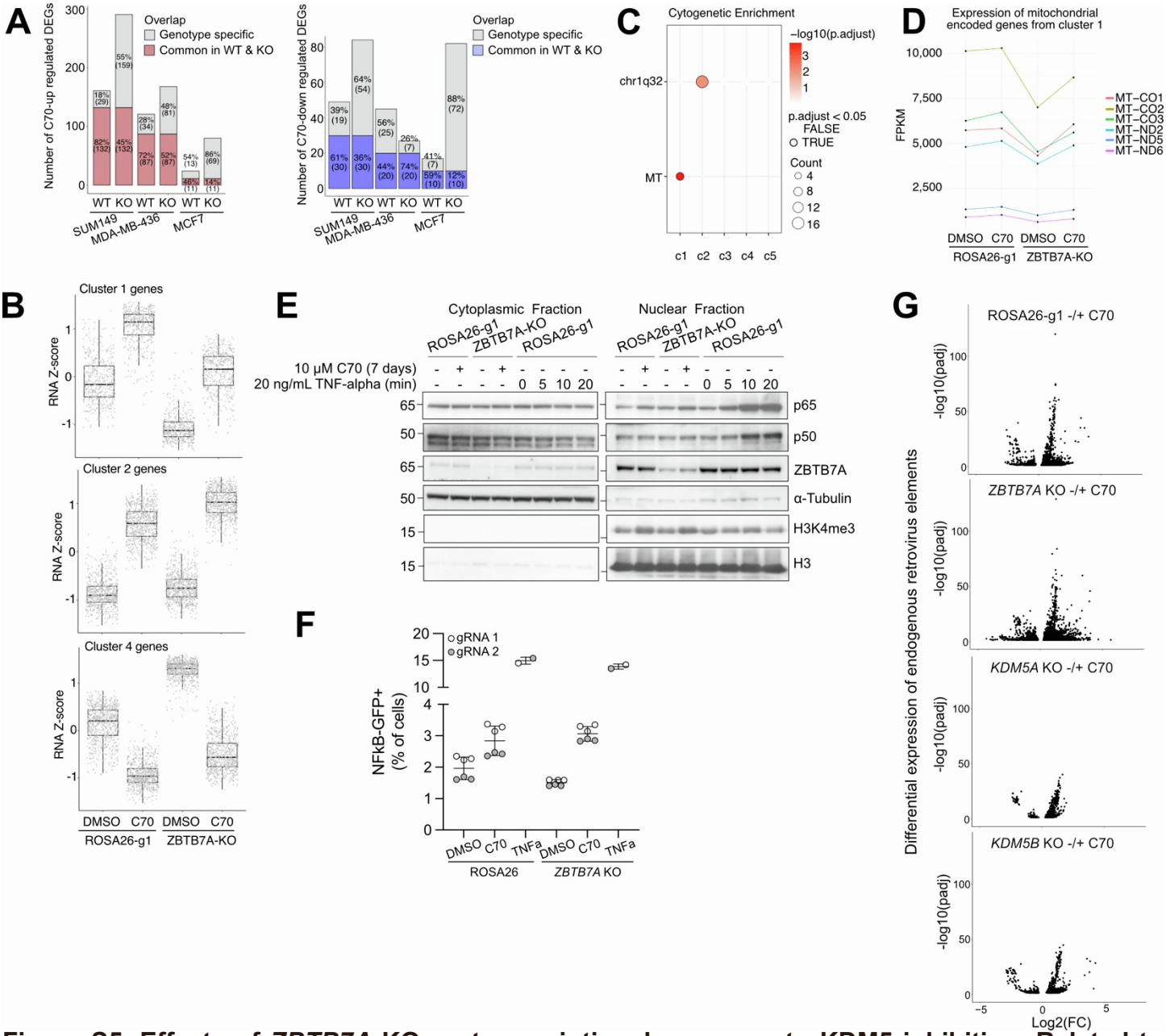

Figure S5. Effects of *ZBTB7A* KO on transcriptional response to KDM5 inhibition. Related to Figure 5.

(A) Number of up and down-regulated DEGs (padj < 0.05 and |log2(FC)| > 1) after 10 μM C70 treatment for 7 days within the indicated wild-type parental and *ZBTB7A* KO cell lines. DEGs common between both the WT and *ZBTB7A* KO are shaded in red (up-regulated) or blue (down-regulated).

(B) Box plot of RNA Z-scores within each cluster from **Figure 5D**.

(C) Enrichment of MSigDB's positional gene sets corresponding to human chromosome cytogenetic bands on each RNA-seq cluster from **Figure 5D**.

(D) FPKM values of mitochondrial encoded genes enriched in **Figure S4D**.

(E) Nuclear localization of NF-kB (p65 and p50). Immunoblot on cytoplasmic/nuclear fractions of SUM149 ROSA26-g1 and *ZBTB7A* KO cells -/+ 10 μM C70 for 7 days. 20 ng/mL TNF-alpha for the indicated time points was used as a positive control.

(F) NF-kB promoter activity assessed via a GFP-reporter construct driven by an NF-kB minimal promoter. Percent of GFP positive cells assessed via flow cytometry. Median + SD is shown.

(G) Differential endogenous retrovirus (ERV) expression after 7 days of 10 μM C70 treatment in the indicated SUM149 wild-type (ROSA26-g1) and knockout (*ZBTB7A* KO, *KDM5A* KO, *KDM5B* KO) cell lines. Results were calculated from RNA-seq data with the ERVmap pipeline. ERVs with -log10(padj) > 40 and |log2(FC)| > 1.5 are labelled.